Numerical Study of Flow and Heat Transfer in Wavy Passages

K. M. Stone and S. P. Vanka

ACRC TR-118 May 1997

For additional information:

Air Conditioning and Refrigeration Center
University of Illinois
Mechanical & Industrial Engineering Dept.
1206 West Green Street
Urbana, IL 61801

(217) 333-3115

Prepared as part of ACRC Project 65
Investigation of Wavy Fins for Heat Transfer Augmentation in Refrigeration/Air Conditioning Systems
S. P. Vanka, T. A. Newell and A. M. Jacobi, Principal Investigators

The Air Conditioning and Refrigeration Center was founded in 1988 with a grant from the estate of Richard W. Kritzer, the founder of Peerless of America Inc. A State of Illinois Technology Challenge Grant helped build the laboratory facilities. The ACRC receives continuing support from the Richard W. Kritzer Endowment and the National Science Foundation. The following organizations have also become sponsors of the Center.

Amana Refrigeration, Inc.
Brazeway, Inc.
Carrier Corporation
Caterpillar, Inc.
Copeland Corporation
Dayton Thermal Products
Delphi Harrison Thermal Systems
Eaton Corporation
Ford Motor Company
Frigidaire Company
General Electric Company
Hydro Aluminum Adrian, Inc.
Indiana Tube Corporation
Lennox International, Inc.
Modine Manufacturing Co.
Peerless of America, Inc.
Redwood Microsystems, Inc.
The Trane Company
Whirlpool Corporation
York International, Inc.

For additional information:

Air Conditioning & Refrigeration Center
Mechanical & Industrial Engineering Dept.
University of Illinois
1206 West Green Street
Urbana IL 61801

217 333 3115

ABSTRACT

Flow and heat transfer in a wavy passage are analyzed using an accurate numerical scheme that solves the two-dimensional unsteady flow and energy equations, for both developing and periodically fully-developed flow conditions. Developing flow calculations are presented for two different wavy channels, each consisting of 14 waves. It is observed that the flow is steady in part of the channel and unsteady in the remainder. As the Reynolds number is progressively increased, the unsteadiness is onset at a much earlier location, leading to increased heat transfer rates. Calculations for fully-developed flow were performed using periodic boundary conditions. The ensuing results reveal the effects of individually varying the height, amplitude, and wavelength of a selected wavy passage.

TABLE OF CONTENTS

NOMENCLATURE

a	Amplitude
a_{11}	Metric coefficient resulting from coordinate transformation
a_{22}	Metric coefficient resulting from coordinate transformation
C	Convection term in momentum equation
D	Diffusion term in momentum equation
D_h	Hydraulic diameter
f	Friction factor
h	Heat transfer coefficient
H	Separation distance between walls. Also sum of convection and diffusion terms
J	Jacobian of the coordinate transformation
k	Thermal conductivity
n	General integer variable
Nu	Nusselt number
p	Pressure
Pr	Prandtl number
Q	Volumetric flow rate
Re	Reynolds number
s	General length variable
t	Time
T	Temperature

u	Cartesian velocity vector
u	Cartesian velocity component in the x direction
U	Contravariant velocity vector
U	Contravariant velocity component in the ξ direction
v	Cartesian velocity component in the y directoin
V	Contravariant velocity component in the η direction
x	Cartesian coordinate
y	Cartesian coordinate

Greek Symbols

α	Thermal diffusivity
ϕ	Phase shift between upper and lower walls
η	General curvilinear coordinate
λ	Wavelength
ν	Kinematic viscosity
θ	Dimensionless temperature
ρ	Density
ξ	General curvilinear coordinate

Subscripts

avg	Spatially-averaged quantity
i	Index corresponding to the ξ direction
in	Quantity evaluated at the inlet
j	Index corresponding to the η direction
m	Bulk mean quantity
max	Quantity evaluated at maximum cross-section. Also maximum value of specified quantity
out	Quantity evaluated at the outlet
w	Quantity evaluated at the wall
λ	Value of quantity evaluated over a single wavelength

Superscripts

^ (carrot)	Intermediate quantity in fractional step scheme
$\bar{}$ (overbar)	Time-averaged quantity
+	Denotes face of control volume located in the positive direction of the specified coordinate
-	Denotes face of control volume located in the negative direction of the specified coordinate
n	Index corresponding to time

CHAPTER 1: INTRODUCTION

1.1 Overview of Present Research

For air-side heat transfer applications, special surfaces are often employed to obtain high rates of heat transfer within the imposed size constraints. One geometry that can be used to enhance heat exchanger performance is a sinusoidally curved wavy passage. Wavy channels are easy to fabricate, and can provide significant heat transfer enhancement if implemented in an appropriate (transitional) Reynolds number regime. Several studies have been conducted to evaluate the degree of heat transfer enhancement attained by utilizing wavy passages. These studies have shown that wavy passages can be very effective enhancement devices when the flow is unsteady, but they do not provide significant enhancement in the steady flow regime.

In a previous study of unsteady heat transfer in a periodic wavy passage, Wang and Vanka (1995) found that the flow becomes unstable for Reynolds numbers as low as 160. This means that for an infinitely long periodic passage, the flow will eventually transition to an unsteady state with self-sustaining oscillations downstream of a certain point in the passage. This onset location varies strongly with Reynolds number. However, numerical studies conducted so far have primarily considered the flow to be periodic in the streamwise direction. One of the purposes of the current study is to use numerical simulations to thoroughly examine developing flow and heat transfer in a wavy passage, and determine how long such a channel must be for instabilities to evolve and cause the flow to become unsteady. This is important, because heat transfer

enhancement in a wavy passage is not achieved until the flow transitions to an oscillatory state. Thus, if the onset location for the instabilities is far downstream of the entrance at a given Reynolds number, the practical benefits of the wavy geometry in this regime would be minimal, even though the flow can actually become unstable in a longer channel. This study determines the onset location where the flow becomes unsteady as a function of the Reynolds number for three specific geometrical configurations. In addition, the characteristics of the developing flow patterns are investigated, and comprehensive heat transfer and pressure drop data are presented.

Simulations of developing flow provide valuable insight regarding the degree of heat transfer enhancement that can be expected in an actual finite wavy passage. Unfortunately, developing flow calculations are quite cumbersome, because the entire length of the passage must be modeled. Thus, one cannot extensively analyze many different channel configurations. The effects of varying the geometry can be more effectively studied using fully-developed flow simulations. For fully-developed flow, periodic boundary conditions are employed, and the computational domain need only consist of a single wave (Wang and Vanka, 1995). The numerical results presented herein for developing flow are complemented by concurrent experimental data (Rush, 1997).

1.2 Motivation for Heat Transfer Enhancement

For well over a century, efforts have been made to produce more efficient heat exchangers by employing various methods of heat transfer augmentation. The study of enhanced heat transfer has gained serious momentum during recent years due to increased demands by industry for heat exchange equipment that is less expensive to build and operate. Savings in materials and energy use also provide strong motivation for the development of improved methods of enhancement. When designing heat exchangers for air conditioning and refrigeration applications, it is imperative that they are made as compact and lightweight as possible. This is especially true for cooling systems in automobiles and spacecraft, where volume and weight constraints are particularly stringent.

Numerous methods have been developed to increase the rates of heat transfer in compact exchange devices operated in the laminar regime (Webb, 1994). The objective behind these methods is to efficiently interrupt the boundary layer that forms on the exchange surface and replace it with fluid from the core, thereby creating a fresh boundary layer that has increased near-wall temperature gradients. This leads not only to higher rates of heat transfer, but to greater frictional losses as well. Therefore, the primary goal for any enhancement scheme is to increase heat transfer as much as possible while minimizing pressure drop.

Enhancement techniques can be separated into two categories: passive and active. Passive methods require no direct application of external power. Instead, passive techniques employ special surface geometries or fluid additives which induce a higher rate of heat transfer.

On the other hand, active schemes do require external power for operation (Bergles, *et al.* 1979). Some examples are: electromagnetic fields, direct surface vibration, and acoustic excitation of the flow. In general, active techniques have attracted little enthusiasm because of the costs involved, and the problems that are associated with vibration or acoustic noise (Webb, 1987). As a result, passive enhancement through the use of various special surface geometries tends to be preferred. Examples of such devices are: offset strip fins, louvers, and vortex generators.

The wavy passage is another special surface that can be used to promote heat transfer. This is accomplished due to complex recirculatory flows and boundary layer separation. Several studies have been conducted to evaluate the degree of enhancement provided by this geometry. However, the developing section of the passage has not been numerically analyzed for unsteady laminar flow in the low Reynolds number regime ($Re < 1000$) that is relevant to compact heat exchanger operation.

1.3 Compact Heat Exchangers

In forced-convection heat transfer between a gas and a liquid, the heat transfer coefficient of the gas may be 10 to 50 times smaller than that of the liquid. The use of specially-configured surfaces can be used to reduce the gas-side thermal resistance. For heat transfer between two gases, the difficulty in inducing the desired heat exchange is even more pronounced. In this case especially, the use of enhanced surfaces can substantially reduce heat exchanger size. This is the motivation behind the design of a category of heat exchangers with reduced size and greatly enhanced gas-side heat transfer, which are referred to as "compact".

A compact heat exchanger is generally defined as one which incorporates a heat transfer surface having a high "area density". In other words, it possesses a high ratio of heat transfer surface area to volume. This does not necessarily mean that compact heat exchangers are of small mass or volume. However, if they did not incorporate a surface of such high area density, the resulting units would be much more bulky and massive than their compact counterparts.

Various techniques can be used to make heat exchangers more compact. Three general types of extended surface geometries which can be used to increase gas-side heat transfer coefficients include: (a) finned-tube heat exchangers with flat fins, (b) finned-tube heat exchangers with individually finned tubes, and (c) plate-fin heat exchangers. One type of plate-fin exchanger that can be employed for augmenting heat transfer rates is a periodically converging-diverging (C-D) channel, such as those addressed in the present work. Due to their small hydraulic diameter and the low density of gases, special surface geometries must be effective in the low Reynolds number regime.

1.4 Outline of Thesis

In the present work, flow through wavy passages is analyzed numerically for both developing and fully-developed flow conditions. The computational simulations were performed using a privately-developed FORTRAN program that numerically integrates the time-dependent flow and energy equations. This study expands on previous work by Wang and Vanka (1995), in which they analyzed fully-developed flow for a single wavy channel.

A comprehensive review of pertinent literature is presented in Chapter 2. Although this summary is by no means all-inclusive, it covers a wide range of different studies that have been conducted on this topic, with an emphasis on those which are most closely related to the current inquiry. The papers are categorized based on the method of investigation (numerical or experimental), and on the geometrical configurations of the passages that were analyzed.

In Chapter 3, the governing equations for 2-D laminar incompressible flow are presented. The equations are discretized and solved on an orthogonal curvilinear mesh, using a fractional step method with Adams-Bashforth differencing of the momentum equations. The pressure equation is solved using the conjugate gradient technique without preconditioning. Different boundary conditions must be employed, depending on whether one wishes to model fully-developed flow, or flow in the entrance region of the passage.

In Chapter 4, the results of calculations for flow in the entrance length of a wavy passage are discussed. Developing flow simulations were performed for two different wave geometries. The first corresponds to the passage analyzed by Wang and Vanka (1995). The second passage has the same wall geometry, but the minimum distance between the two walls is doubled. For each case, a channel with 14 periodic waves is examined.

In Chapter 5, the results of calculations for fully-developed flow are presented. Because these simulations feature periodic boundary conditions, only one wave is needed for the computational domain. Thus, calculations can be performed more rapidly, and the parameter

space can be further expanded. For fully-developed flow, the effects of separately varying the height, amplitude, and wavelength of furrowed passages are considered.

CHAPTER 2: REVIEW OF RELEVANT LITERATURE

2.1 Examples of Other Non-Wavy Enhancement Geometries

A high-performance enhancement surface will increase the heat transfer that takes place within a heat exchanger, without incurring penalties on friction and pressure drop that are severe enough to negate the benefits of the augmented heat transfer. A wide variety of plate-fin configurations have been suggested to perform this function in compact heat exchangers. Included among these are wavy and corrugated channels that are at least conceptually similar to the geometries investigated in the present work. Previous studies which have focused on such geometries are discussed further in Section 2.2.

For any proposed enhancement mechanism to be considered as a viable alternative for practical heat exchanger applications, they must exhibit performance that is at least comparable to other existing plate-fin configurations. Figure 2.1.1 includes general examples of five such geometries: (A) rectangular plain fins, (B) triangular plain fins, (C) offset strip fins, (D) louvered fins, and (E) vortex generators. The remainder of Section 2.1 features a brief description of each of these designs.

Plain Fins

Plain fins are the most basic special surface geometry. Plain fin surfaces are characterized by long uninterrupted flow passages with performance comparable to that obtained inside long circular tubes (Kays and London, 1964). The plain fins that are most commonly used have flow channels with either a rectangular or triangular cross-section, corresponding to surfaces A and B in Figure 2.1.1. The enhancement in heat transfer achieved with plain fins results mainly from increased area density, rather than any substantial rise in heat transfer coefficient (Brockmeier, *et al.* 1993). Plain fins require a smaller flow frontal area than interrupted surfaces (i. e. offset strip fins and louvered fins) for given values of heat duty, pressure drop, and flow rate, but the flow length with plain fins will be greater, resulting in a higher overall heat exchanger volume (Shah and Webb, 1983).

Offset Strip Fins

The offset strip fin geometry (Figure 2.1.1(C)) is one of the most widely-used enhancement surfaces in compact heat exchangers. As fluid flows over one of the strips, a laminar boundary layer develops on the short strip length, and is then dissipated in the wake region between strips. This process is then repeated throughout the entire array. The recurrent cycles of boundary layer growth and destruction resulting from the interrupted nature of the surface lead to higher rates of heat transfer than those which can be attained using plain fins. Offset strip fins are usually operated in the laminar flow regime. Typical strip lengths range from 3 to 6 mm (Webb, 1987). It should be noted that the enhancement provided by offset strip fins

results from expanding the effective surface area within the exchanger, as well as increasing the heat transfer coefficient (Brockmeier, *et al.* 1993).

Louvered Fins

Louvered fin surfaces (Figure 2.1.1(D)) are commonly used in automobile radiators. The louvered fin geometry consists of an interrupted surface similar to that of the offset-strip fin. However, the slit strips of louvered fins are not completely offset. Instead, the slit fin is rotated between 20° and 60° relative to the direction of the airflow. Most radiators use a louver strip width of 1.0 to 1.25 mm (Webb, 1987). For equal strip width, the louvered fin configuration provides enhancement comparable to that of offset strip fins. Moreover, louvered fins are less expensive than offset strip fins for large-quantity production, by virtue of their ease of manufacture using high-speed mass production technology (Shah and Webb, 1983).

Vortex Generators

Vortex generators are a relatively new class of enhancement devices. One such structure is the wing-type vortex generator plate shown in Figure 2.1.1(E). Vortex generators do not significantly change the effective heat transfer surface area of the plate. Instead, they increase the heat transfer coefficient by creating longitudinally spiraling vortices which promote mixing between the core and near-wall regions of the flow (Brockmeier, *et al.* 1993). Lately, vortex generators have spawned a great deal of interest. However, because thorough examination of these surfaces has only recently begun, quality data for vortex generators is still fairly scarce. This

is due in part to the fact that there are numerous possibilities for different vortex generator surfaces. One can vary the size, angle of attack, aspect ratio, and/or arrangement for any given shape of vortex generator. As a result, an optimal configuration has not yet been found.

2.2 Experimental Studies of Flow in Wavy Channels

Rush (1997) has performed a series of flow visualization and wind tunnel experiments which correspond to the calculations presented herein, and to those of Voelker and Vanka (1997). The results of Rush's experiments can be compared directly with the numerical results for developing flow presented in Chapter 4. Therefore, no further mention of Rush's work is made in this chapter. But there are a number of other previously published findings concerning similar flow problems.

Viscous flow in wavy channels was first treated analytically by Burns and Parks (1967). They obtained a solution by expressing the stream function in a Fourier series under the assumption of Stokes flow. Since then, several investigations have been conducted to analyze flow through various types of wavy and triangular corrugated passages. Experimental studies that are pertinent to the present work are discussed in the remainder of Section 2.2. Earlier relevant numerical work is reviewed in Section 2.3.

2.2.1 Serpentine Channels

Triangular corrugated channels

Goldstein and Sparrow (1977) were probably the first to study the local heat and mass transfer characteristics of a triangular corrugated channel with a uniform cross-sectional area for the laminar, transitional, and low Reynolds number turbulent flow regimes. Their experiments showed only minimal enhancement in the laminar regime. However, for low Reynolds number turbulent flow (Re ~ 6000-8000), the heat transfer rates exceeded those of a conventional straight channel by a factor of 3. Because the passage had only two corrugation cycles, entrance effects influenced the results. O'Brien and Sparrow (1982) conducted one of the first comprehensive studies for the fully-developed region of a corrugated channel for flow in the range of $1500 < Re < 25{,}000$. They observed heat transfer rates that were approximately 2.5 times greater than for the straight channel. But the pressure drop for the corrugated duct was significantly larger as well.

Sparrow and Comb (1983) performed a similar study for a corrugated channel with an interwall spacing that was approximately 45% greater than the channel used by O'Brien and Sparrow (1982), and then analyzed the effects of this variation. The increase in spacing led to a 30% rise in the fully-developed Nusselt number, but the friction factor more than doubled. To further assess these findings, performance evaluations were carried out for three different constraints. For all three cases, the performance differences between the two ducts were not sufficiently great to indicate a clear superiority of one over the other.

Ali and Ramadhyani (1992) conducted experiments to analyze the developing flow region of triangular corrugated channels. They examined laminar and transitional flow for two different interwall spacings. For both channels, they observed a transition to unsteady flow at $\mathrm{Re} \approx 500$, accompanied by a sharp increase in Nusselt number. As a result, optimal heat transfer enhancement was found to occur in the transitional flow regime. No substantial enhancement was detected when the flow was steady.

Sinusoidally curved wavy passages

Beginning with Goldstein and Sparrow (1977), several experimental studies were performed which demonstrated that a triangular corrugated channel with two in-phase walls could be used to achieve increased rates of heat transfer, at least within the transitional flow regime. But the gains in heat transfer were accompanied by substantial rises in pressure drop. One way to decrease the frictional losses while maintaining the same flow structure is to use walls with smoother wavy or curved corrugations, rather than abrupt triangular corrugations.

The most voluminous body of work concerning flow through wavy passages is encompassed by a series of flow visualization and mass transfer experiments performed by Japanese research groups headed by T. Nishimura. Nishimura, *et al.* (1986) investigated the relationship between flow structure and mass transfer for fully-developed flow in a sinusoidally curved wavy channel for laminar, transitional, and turbulent flows. Nishimura, *et al.* (1990a) examined the occurrence and structure of longitudinal vortices in wavy channels, at relatively low

Reynolds numbers (Re = 50 - 500). They observed that the developing flow becomes less stable as it proceeds downstream, and that flow can become three-dimensional for Reynolds numbers as low as 100. Nishimura's groups also performed many experiments for wavy channels with a symmetric converging-diverging cross-section. These are discussed in Section 2.2.2.

Oyakawa, *et al.* (1989) examined how heat transfer and fluid flow are affected by varying the height of a wavy sinusoidal passage. From these experiments, they obtained an optimum spacing for fully-developed flow using the chosen wall geometry. A study with similar goals was conducted by Gschwind, *et al.* (1995), using flow visualization and mass transfer experiments with air. In addition to demonstrating the qualitative effects of varying the Reynolds number and the channel spacing, they also provide a stability diagram that describes the existing range of longitudinal vortices.

Other serpentine channels without triangular or sinusoidally curved walls

Snyder, *et al.* (1993) measured heat transfer rates and pressure drops in the thermally fully-developed region of a serpentine channel for Reynolds numbers ranging from 250 to 10,000. The channel used for these experiments looks very similar to the sinusoidally curved wavy passages discussed above. But this channel consists of two walls, each comprised of 30 recursive arc circles, resulting in a passage with 15 waves. This design was chosen with the purpose of minimizing the extent of flow separation. On an equal Reynolds number basis, Snyder, *et al.* found that, for air, the heat transfer in the serpentine channel was as much as 9 times greater than in a straight parallel-plate channel.

Recently, Choi, *et al.* (1996) studied mass transfer (and by extension, heat transfer) for turbulent flow in a serpentine channel with right-angled turns. Using local and regional measurements for heat/mass transfer, they determined that the flow may be considered periodic downstream of the fifth period in their channel. They also found that the heat transfer enhancement attained was offset by large pressure drops.

2.2.2 Furrowed Channels

Mendes and Sparrow (1984) performed a comprehensive experimental study to analyze turbulent fluid flow for the entrance region and for fully-developed flow in periodically converging-diverging tubes. The Reynolds number for these experiments ranged from 6000 to 70,000. The geometry of the tubes was also varied. Mendes and Sparrow compared the performance of the C-D tubes to a conventional straight tube for two sets of constraints. In both cases, the C-D channel provided significant enhancements over the straight channel.

The Japanese research group led by T. Nishimura has produced a number of experimental studies regarding sinusoidally curved wavy channels with a periodic C-D, or "furrowed," cross-section. Nishimura, *et al.* (1984) examined the characteristics for steady flow in a symmetric wavy channel, over a Reynolds number regime ranging from fully laminar to fully turbulent flow. They also conducted a numerical investigation for laminar steady flow, using a two-dimensional finite-element approach to calculate vorticity and stream function. The dimensions of their channel have been adopted as the base configuration for the present study.

Nishimura, *et al.* (1985) investigated the mass transfer characteristics resulting from the flow dynamics observed by Nishimura, *et al.* (1984). They determined, analytically and experimentally, the mass transfer coefficients for the same wavy channel at high Peclet numbers for laminar and turbulent flow. They found that although there is minimal mass transfer enhancement over a straight channel for steady laminar flow, there is a large degree of enhancement for turbulent flow.

Nishimura, *et al.* (1987) analyzed the flow and mass transfer characteristics for oscillatory inflow with the same wall geometry. In this study, however, they also varied the phase shift between the upper and lower walls. Three different geometries were employed (ϕ = 0°, 90°, and 180°). Nishimura, *et al.* (1990b) compared the flow and mass transfer properties of the symmetric wavy-walled channel to those of a similar arc-shaped channel. Experiments were performed for Re = 20-300.

Stephanoff, *et al.* (1980) provide photographs of the flow patterns observed through a furrowed channel with sinusoidally curved wavy walls. Flow visualizations were performed for steady and oscillatory inflow at relatively low Reynolds numbers. This experimental study serves as a companion to the numerical work performed by Sobey (1980) (see Section 2.3.2). Stephanoff (1986) provides an extension of these two companion reports. Fourier analysis is utilized to determine the amplified frequencies of the observed self-excited shear-layer oscillations present in the developing flow profile.

2.2.3 Channels with a Single Wavy/Corrugated Wall

During the past decade, Greiner, *et al.* have published a series of papers dealing with heat transfer augmentation in a grooved channel. The channel features a flat upper wall, and a lower wall with a series of periodic triangular grooves. The geometry of the passage is designed to excite normally damped Tollmien-Schlichting modes in order to enhance mixing.

Greiner, *et al.* (1990) performed flow visualizations and convective heat transfer measurements for developing flow in this channel over the Reynolds number range, Re = 300-15,000. The flow visualizations revealed that the flow is steady near the entrance, but becomes oscillatory downstream of a certain onset location. This location is found to move upstream with increasing Reynolds number. The onset location for oscillatory flow also corresponds to the place where heat transfer enhancement is first realized. The degree of heat transfer enhancement increases with the distance downstream from the onset location. Heat transfer measurements along the smooth channel boundary indicate an augmentation of approximately 65% over an equivalent straight channel in the transitional flow regime. Also, the flow is found to be intermittently unsteady over a very narrow range of Reynolds numbers, which will vary as a function of streamwise location.

Greiner, *et al.* (1991) performed experiments with a similar grooved channel. This channel had a minimum spacing equal to half the spacing used by Greiner, *et al.* (1990). This experiment included measurements for pressure drop along the flat surface, as well as for heat

transfer. Measurements were made using air for the Reynolds number range, Re = 300-5000. For a given Reynolds number, the development length is observed to be shorter for the narrower channel. Greiner, *et al.* (1995) extended this study even further, by examining heat transfer augmentation in the recovery section immediately downstream of the grooved passage. Interestingly, they find that the mechanics for heat and momentum transport are uncoupled in the recovery region. They conclude, therefore, that short flat regions placed intermittently in a grooved passage may be useful in reducing the overall pumping power required to obtain a desired amount of heat transfer.

Saniei and Dini (1993) performed an experimental study of convective heat transfer in the turbulent regime for flow over a single wavy wall in a duct. Data were obtained for developing flow over seven waves. Local Nusselt number distribution is plotted over the entire wavy wall. Average Nusselt numbers for each wave are plotted as a function of the number of waves downstream of the inlet. Similar plots for average Nu vs. wave number are given in the present work for laminar/transitional flow in furrowed wavy passages.

2.3 Numerical Studies of Flow in Wavy Channels

2.3.1 Serpentine Channels

Voelker and Vanka (1997) have performed numerical simulations for developing and fully-developed flow in a serpentine channel. These calculations were conducted concurrently with those presented herein for the furrowed passage. The wall geometry for the serpentine channel is the same one used as the base case for the furrowed channel study. That is, a sinusoidally curved wavy wall with the dimensions used by Nishimura, *et al.* (1984). Voelker and Vanka analyzed a serpentine channel with a 0° phase shift between the top and bottom walls.

Several other numerical analyses have focused on the flow and heat transfer characteristics of corrugated and wavy channels with a serpentine geometry. Amano, *et al.* (1987) used a full Reynolds-stress model to examine turbulent flow and heat transfer in a channel composed of two triangular corrugated walls aligned in phase with each other. Asako and Faghri (1987) obtained solutions for fully-developed flow and heat transfer in a corrugated duct using finite-volume based simulations. Only flow in the laminar regime was considered. The performance of the corrugated duct is compared to that of a straight duct under three different constraints - fixed pumping power, fixed pressure drop, and fixed mass flow rate. Small differences in the enhancement ratios were observed under these constraints. Asako, *et al.* (1988) assessed the heat transfer and pressure drop characteristics of a similar corrugated duct with rounded corners. The duct boundaries were approximated by a cosine function. Computations

were carried out in the Reynolds number range, Re = 100-1000, for several geometrical configurations. It was determined that the change in heat transfer rates caused by rounding the corners depends on the specific flow conditions, geometry, and performance constraints.

Garg and Maji (1988a) applied a finite-difference numerical scheme to laminar flow through a serpentine channel with sinusoidally curved wavy walls. Results were tabulated for both developing and fully-developed flow, for Reynolds numbers ranging from 100 to 500. The channel dimensions were varied as well. For one chosen configuration, a number of figures are featured which detail the behavior of velocity, pressure, and enthalpy for developing laminar flow.

2.3.2 Furrowed Channels

Wang and Vanka (1995) analyzed convective heat transfer for fully-developed flow in a periodic wavy passage for several Reynolds numbers. This study is a direct predecessor to the current investigation. For the base geometry presented in this paper, developing flow is examined in what can be viewed as the entry section for the periodic wavy passage analyzed by Wang and Vanka. In addition, their periodic channel geometry serves as the basis of comparison for the other periodic channel simulations presented in Chapter 5.

Sparrow and Prata (1983) examined a family of periodic ducts, using both numerical and experimental methods. The periodic duct is a tube consisting of a succession of alternately converging and diverging conical sections. Numerical simulations were carried out for fully-developed laminar flow in the Reynolds number range, Re = 100-1000, for various duct

configurations. The resulting data indicated that the periodic C-D tube is not conducive to heat transfer enhancement for steady laminar flow.

Vajravelu (1980) solved the governing equations for fluid flow and heat transfer in a wavy passage by separating the solution into two parts: a mean part and a perturbed part. The mean part of the solution was found to correspond closely with that of plane Poiseuille flow, while the perturbed part of the solution represents the contribution from the waviness of the walls. Four different values of ϕ were considered: 0°, 90°, 180°, 270°. The mean, perturbed, and total solutions were evaluated numerically for each configuration.

As mentioned previously in Section 2.2.2, Sobey (1980) conducted a numerical study of flow through furrowed channels in conjunction with a related experimental investigation (Stephanoff, *et al.*, 1980). Sobey calculated the flow patterns obtained using both steady and pulsatile inflow. The effects of varying the dimensional parameters and the Reynolds number were examined. Furthermore, the flow structures that occur in a channel with arc-shaped walls are compared with the patterns induced by sinusoidally curved wavy walls. Oscillatory flow in various types of wavy passages is examined further in subsequent studies performed by Sobey (1982, 1983).

Garg and Maji (1988b) used a finite-difference methodology to solve the governing equations for steady laminar flow and heat transfer in a furrowed wavy channel. Calculations were performed using various wall amplitudes for Re = 100-500. Both the developing and the fully-developed flow regions were analyzed. The local Nusselt number was observed to fluctuate

sinusoidally in the fully-developed region. Moreover, the Nusselt number increased with the Reynolds number, unlike what transpires for laminar flow through a straight channel.

Recently, Guzman and Amon have published research documenting the transition to chaos for fully-developed flow in furrowed wavy channels. Specifically, the Ruelle-Takens-Newhouse scenario for the onset of chaos is verified using direct numerical simulations (DNS) (Guzman and Amon, 1994). The results are illustrated for various Reynolds numbers using velocity time signals, Fourier power spectra, and phase space trajectories. The dimensions for the 2-D sinusoidally curved wavy channel are the same as those used for the base case in this paper.

Guzman and Amon (1996) extended their previous study by using DNS to calculate dynamical system parameters. Dynamical system techniques, such as time-delay reconstructions of pseudophase spaces, Poincare maps, autocorrelation functions, fractal dimensions, and Eulerian Lyapunov exponents are employed to characterize laminar, transitional, and chaotic flow regimes. Also, 3-D simulations are performed to determine the effect of the spanwise direction on the route of transition to chaos.

2.3.3 Channels with a Single Wavy Wall

Patel, *et al.* published a pair of papers dealing with flow through a channel with a single wavy wall. One of the papers dealt with steady laminar flow over a wall with six waves (Patel, *et al.*, 1991a), and the other addressed turbulent flow over the same wall (Patel, *et al.*, 1991b). For the laminar case, the pressure and friction coefficients are plotted over the course of the wavy

wall. It should be noted, however, that these calculations are performed for a channel Reynolds number of 10,760, a value that is considerably higher than the expected transition Reynolds number. Therefore, the results are not indicative of what would actually occur in an analogous physical situation.

CHAPTER 3: MATHEMATICAL FORMULATION AND NUMERICAL PROCEDURE

3.1 Governing Equations

In the present study, laminar flow of a Newtonian fluid through wavy passages is investigated. This type of flow is governed by the familiar time-dependent Navier-Stokes equations. The flow is also considered to be two-dimensional with no variation in the spanwise direction. Assuming incompressible flow and constant fluid properties, the governing equations for mass continuity, momentum, and energy take the following general forms:

mass continuity:

$$\nabla \cdot \mathbf{u} = 0 \tag{3.1}$$

momentum:

$$\frac{\partial \mathbf{u}}{\partial t} + \nabla \cdot (\mathbf{uu}) = -\nabla p + \nu \nabla^2 \mathbf{u} \tag{3.2}$$

energy:

$$\frac{\partial \theta}{\partial t} + \nabla \cdot (\mathbf{u}\theta) = \alpha \nabla^2 \theta \tag{3.3}$$

where ν and α are the kinematic viscosity and the thermal diffusivity, respectively. Also, note that density is assumed to be unity throughout this paper. The dimensionless temperature θ is defined as:

$$\theta = \frac{T - T_w}{T_{m,in} - T_w} \tag{3.4}$$

where T_w is the temperature prescribed uniformly along the wall, and $T_{m,in}$ is the bulk mean temperature evaluated at the inlet section of the computational domain. The temperature distribution at the inlet is prescribed uniformly for the developing flow calculations (see Section 3.5 for more details on boundary conditions), but in general, the bulk mean temperature is calculated by taking the mass-averaged value of the temperature along the selected cross-section,

$$T_m = \frac{\int T(s)\, u(s)\, ds}{\int u(s)\, ds} \tag{3.5}$$

3.2 Grid Generation

The discretized versions of the conservation equations presented in Section 3.1 are solved on a two-dimensional curvilinear orthogonal grid. Rather than describing the flow geometry in

Cartesian coordinates (x,y), it is described with a general coordinate system (ξ,η). A combination of algebraic and differential equation techniques is used to generate the final mesh.

First, an initial non-orthogonal mesh is derived algebraically from the prescribed boundaries for a single wave in the domain. The technique used here is Lagrange linear interpolation, where one family of grid lines (in this case, the constant-η lines) are straight, connecting corresponding boundary points. A linear distribution for the x-coordinates is assigned throughout:

$$x_{i,j} = \frac{i-1}{i_{max,\lambda} - 1}\lambda \tag{3.6}$$

where i and j represent the node numbers in the ξ and η directions, respectively. The nodes are numbered with consecutive integers, beginning at 1 for the first node in each direction. For the meshes generated here, the wave is divided into 64 x 64 internal cells. Therefore,

$$i_{max,\lambda} = j_{max,\lambda} = 65 \tag{3.7}$$

For a specified wavelength, amplitude, and average spacing, the y-coordinates along the wall boundaries are determined from the following cosine functions:

$$y_{i,1} = -\frac{H_{avg}}{2} + a * \cos\left(\frac{2\pi x_{i,1}}{\lambda}\right) \tag{3.8}$$

$$y_{i,j_{max,\lambda}} = \frac{H_{avg}}{2} - a * \cos\left(\frac{2\pi x_{i,j_{max,\lambda}}}{\lambda}\right) \tag{3.9}$$

The y-coordinates for the interior nodes are then found by interpolating between the two boundaries defined above:

$$y_{i,j} = \frac{(j_{max,\lambda} - j)y_{i,1} + (j-1)y_{i,j_{max,\lambda}}}{j_{max,\lambda} - 1} \tag{3.10}$$

Now, a mesh such as the one shown in Figure 3.2.1 has been defined for the entire wave. This grid serves as the initial condition for the transformation to general curvilinear coordinates.

The orthogonal mesh is now generated by solving a system of two discretized Poisson equations (Temperton, 1979). The extremum characteristics that are exhibited by some elliptic systems can guarantee a one-to-one sequential mapping between the physical and transformed regions. The principle behind this is that extrema cannot occur within the solution field. The most simple system of elliptic partial differential equations, and one that features the desired extremum properties, is the Laplace system:

$$\nabla^2 x = x_{\xi\xi} + x_{\eta\eta} = 0 \tag{3.11}$$

$$\nabla^2 y = y_{\xi\xi} + y_{\eta\eta} = 0 \tag{3.12}$$

These two equations are solved iteratively using a fourth-order ADI routine by lagging the coefficients and treating the cross-derivatives explicitly. A boundary value for x or y is computed from the orthogonality constraint, and the other coordinate value is then determined by the relation describing the shape of the boundary (Thompson, *et al.*, 1985).

The final solution to Equations 3.11 and 3.12 provides an orthogonal grid such as the one in Figure 3.2.2 for a single wave with the specified boundaries. For periodic, fully-developed simulations, the governing equations are solved over a single wavelength, so the computed mesh will serve as the actual computational domain. In this case,

$$i_{max} = i_{max.\lambda} = 65 \tag{3.13}$$

$$j_{max} = j_{max.\lambda} = 65 \tag{3.14}$$

and the domain will have a total of 4096 internal cells.

For simulations of developing flow in the entrance region, the single wave mesh can be periodically extrapolated over the desired total channel length. For the calculations presented here, 14 waves are used. In addition, straight sections of height H_{min} and length λ are appended to both ends of the channel, forming a 16λ passage, like the one shown in Figure 3.2.3. Now,

$$i_{max} = 16\left(i_{max.\lambda} - 1\right) + 1 = 1025 \tag{3.15}$$

$$j_{max} = j_{max.\lambda} = 65 \tag{3.16}$$

so the domain has a total of 65,536 internal cells. Consequently, developing flow computations take considerably longer than those for periodic fully-developed flow.

3.3 Spatial Discretization and Coordinate Transformation

The variables are spatially discretized using a collocated arrangement with the two Cartesian velocities and the scalar quantities positioned at the centers of discrete finite volumes in the computational domain. The continuity equation is satisfied by the mass fluxes passing through the cell faces. These contravariant mass fluxes (U, V) are related to the Cartesian velocities (u, v) by

$$U = \left(y_\eta u - x_\eta v\right) \tag{3.17}$$

$$V = \left(x_\xi v - y_\xi u\right) \tag{3.18}$$

where x_ξ, x_η, y_ξ, and y_η determine the metrics of the coordinate transformation. These metrics, along with the Jacobian (J),

$$J = \frac{\partial(x,y)}{\partial(\xi,\eta)} = x_\xi y_\eta - y_\xi x_\eta \tag{3.19}$$

are used to obtain the governing equations for the curvilinear coordinate system. Partial derivatives with respect to Cartesian space are related to partial derivatives with respect to curvilinear coordinates through chain rule differentiation:

$$\frac{\partial}{\partial x} = \frac{\partial}{\partial \xi}\xi_x + \frac{\partial}{\partial \eta}\eta_x \tag{3.20}$$

$$\frac{\partial}{\partial y} = \frac{\partial}{\partial \xi}\xi_y + \frac{\partial}{\partial \eta}\eta_y \tag{3.21}$$

The metrics can be expressed as:

$$\xi_x = \frac{y_\eta}{J} \tag{3.22}$$

$$\xi_y = -\frac{y_\xi}{J} \tag{3.23}$$

$$\eta_x = -\frac{x_\eta}{J} \tag{3.24}$$

$$\eta_y = \frac{x_\xi}{J} \tag{3.25}$$

In discretizing the transformed equations, it is conventional to stipulate the distance between nodes in curvilinear space to be unity for the sake of simplicity:

$$\Delta\xi = \Delta\eta = 1 \tag{3.26}$$

Note that with the collocated storage scheme, the cell-centered Cartesian velocities do not precisely satisfy continuity, even after the corrections are added. However, the resulting error is of the same order as the error in the spatial discretization.

3.4 Fractional Step Method

The numerical integration of the governing equations is based on a two-step fractional step procedure with backward Euler differencing of the time derivative and Adams-Bashforth explicit differencing for the convection-diffusion terms. Fourth-order differencing is used to approximate all of the spatial derivatives.

Calculation of intermediate velocities

In the fractional step procedure, the first stage of the numerical integration consists of solving the momentum equations for an intermediate velocity field $\hat{\mathbf{u}}$. Applying the Adams-Bashforth differencing technique to the momentum equation produces

$$\frac{\hat{\mathbf{u}} - \mathbf{u}^n}{\Delta t} J = \frac{3}{2} H^n - \frac{1}{2} H^{n-1} \tag{3.27}$$

where H represents the sum of the convection and diffusion terms,

$$H = -C_{\mathbf{u}} + D_{\mathbf{u}} = -\nabla \cdot (\mathbf{uu}) + \nu \nabla^2 \mathbf{u} \tag{3.28}$$

For a two-dimensional curvilinear mesh, the sum of the convection terms at the cell faces can be expressed as:

$$C_{\mathbf{u}} = (U\mathbf{u})_{\xi^+} - (U\mathbf{u})_{\xi^-} + (V\mathbf{u})_{\eta^+} - (V\mathbf{u})_{\eta^-} \tag{3.29}$$

Using an orthogonal grid allows one to neglect the cross-derivative quantities in the diffusion terms, leaving,

$$\begin{aligned} D_{\mathbf{u}} = \nu \left[(a_{11})_{\xi^+} \left(\frac{\partial \mathbf{u}}{\partial \xi} \right)_{\xi^+} - (a_{11})_{\xi^-} \left(\frac{\partial \mathbf{u}}{\partial \xi} \right)_{\xi^-} \right] + \\ \nu \left[(a_{22})_{\eta^+} \left(\frac{\partial \mathbf{u}}{\partial \eta} \right)_{\eta^+} - (a_{22})_{\eta^-} \left(\frac{\partial \mathbf{u}}{\partial \eta} \right)_{\eta^-} \right] \end{aligned} \tag{3.30}$$

where the metric coefficients a_{11} and a_{22} are:

$$a_{11} = \frac{x_\eta^2 + y_\eta^2}{J} \tag{3.31}$$

$$a_{22} = \frac{x_\xi^2 + y_\xi^2}{J} \tag{3.32}$$

Pressure equation

Once $\hat{\mathbf{u}}$ is determined, the following Poisson equation is solved for the pressure field:

$$\nabla^2 p^{n+1} = \frac{1}{\Delta t} \nabla \cdot \hat{\mathbf{U}} \tag{3.33}$$

Expanding Equation 3.33 using curvilinear coordinates yields:

$$\begin{aligned} &\left[(a_{11})_{\xi^+} \left(\frac{\partial p}{\partial \xi} \right)_{\xi^+} - (a_{11})_{\xi^-} \left(\frac{\partial p}{\partial \xi} \right)_{\xi^-} \right] + \\ &\left[(a_{22})_{\eta^+} \left(\frac{\partial p}{\partial \eta} \right)_{\eta^+} - (a_{22})_{\eta^-} \left(\frac{\partial p}{\partial \eta} \right)_{\eta^-} \right] = \frac{1}{\Delta t} \left(\frac{\partial \hat{U}}{\partial \xi} + \frac{\partial \hat{V}}{\partial \eta} \right) \end{aligned} \tag{3.34}$$

Again, the cross-derivative terms resulting from the coordinate transformation are neglected, since the mesh is orthogonal. The intermediate values for the contravariant mass fluxes $(\hat{U}, \hat{V})$ are calculated by substituting the intermediate values for the Cartesian velocities $(\hat{u}, \hat{v})$ into Equations 3.17 and 3.18. Equation 3.34 is solved using the conjugate gradient technique without preconditioning.

Update velocities

Using the new pressure field, the intermediate cell-centered velocities are corrected and updated as follows:

$$\mathbf{u}^{n+1} = \hat{\mathbf{u}} - \Delta t \nabla p^{n+1} \tag{3.35}$$

Using i and j to represent the nodal coordinates for a general interior node, the discretized versions of Equation 3.35 for u and v are written as:

$$u_{i,j}^{n+1} = \hat{u}_{i,j} - \frac{\Delta t}{2J}\left[y_\eta\left(p_{i+1,j}^{n+1} - p_{i-1,j}^{n+1}\right) - y_\xi\left(p_{i,j+1}^{n+1} - p_{i,j-1}^{n+1}\right)\right] \tag{3.36}$$

$$v_{i,j}^{n+1} = \hat{v}_{i,j} - \frac{\Delta t}{2J}\left[-x_\eta\left(p_{i+1,j}^{n+1} - p_{i-1,j}^{n+1}\right) + x_\xi\left(p_{i,j+1}^{n+1} - p_{i,j-1}^{n+1}\right)\right] \tag{3.37}$$

The contravariant velocities at the cell faces are updated as well:

$$\mathbf{U}^{n+1} = \hat{\mathbf{U}} - \Delta t \nabla p^{n+1} \tag{3.38}$$

For an orthogonal mesh, the discretized versions of Equation 3.38 for U and V simplify to:

$$U_{i+1/2,j}^{n+1} = \hat{U}_{i+1/2,j} - \Delta t\, a_{11}\left(p_{i+1,j}^{n+1} - p_{i,j}^{n+1}\right) \tag{3.39}$$

$$V_{i,j+1/2}^{n+1} = \hat{V}_{i,j+1/2} - \Delta t\, a_{22}\left(p_{i,j+1}^{n+1} - p_{i,j}^{n+1}\right) \tag{3.40}$$

Energy equation

The equation for the temperature field takes on the same form as Equation 3.27 which was used to solve for the intermediate velocities:

$$\frac{\theta^{n+1} - \theta^{n}}{\Delta t} J = \frac{3}{2} H^{n} - \frac{1}{2} H^{n-1} \tag{3.41}$$

But now,

$$H = -C_{\theta} + \frac{1}{Pr} D_{\theta} = -\nabla \cdot (\mathbf{u}\theta) + \alpha \nabla^{2} \theta \tag{3.42}$$

where Pr is taken to be 0.7, the known Prandtl number for air. C_{θ} and D_{θ} can be readily obtained by substituting θ for **u** in Equations 3.29 and 3.30, respectively.

3.5 Boundary Conditions

Along the walls of the channel, no-slip boundary conditions are prescribed for the Cartesian velocities, along with a constant isothermal temperature distribution. Therefore,

$$u_w = 0 \tag{3.43}$$

$$v_w = 0 \tag{3.44}$$

$$\theta_w = 0 \tag{3.45}$$

For the pressure equation, no boundary conditions are necessary at the walls since the cell face fluxes are known (to be zero) directly. However, wall pressures are still necessary in updating the cell-centered Cartesian velocities. In the algorithm used here, these are obtained by a zero normal derivative condition:

$$\left.\frac{\partial p}{\partial \eta}\right|_w = 0 \tag{3.46}$$

The boundary conditions at the inlet and outlet are prescribed differently depending on whether the simulations are for developing or fully-developed flow.

Developing Flow

At the inlet to the passage, uniform velocity and temperature distributions are applied, where,

$$u_{1,j} = 1 \tag{3.47}$$

$$v_{1,j} = 0 \tag{3.48}$$

$$\theta_{1,j} = 1 \tag{3.49}$$

This condition also specifies the mass flow through the channel, which is used to determine the Reynolds number.

A fully-developed flow condition is specified for the velocities along the outflow boundary:

$$\left.\frac{\partial \mathbf{u}}{\partial x}\right|_{i_{max},j} = \mathbf{0} \tag{3.50}$$

Because the passage for this problem is so long, a uniform temperature distribution,

$$\theta_{i_{max},j} = 0 \tag{3.51}$$

is prescribed at the outlet.

The boundary pressures at the inlet and outlet are calculated using a second-order approximation:

$$p_{1,j} = 2p_{2,j} - p_{3,j} \tag{3.52}$$

$$p_{i_{max},j} = 2p_{i_{max}-1,j} - p_{i_{max}-2,j} \tag{3.53}$$

Fully-developed flow

Since the flow is assumed to be fully-developed in the streamwise direction, the following periodic boundary conditions are used for a domain of length λ:

$$\mathbf{u}(0,y) = \mathbf{u}(\lambda,y) \tag{3.54}$$

$$\frac{\theta(0,y)}{\theta_{m,in}} = \frac{\theta(\lambda,y)}{\theta_{m,out}} \tag{3.55}$$

$\theta_{m,in}$ and $\theta_{m,out}$ denote the bulk mean dimensionless temperatures at the inlet and outlet sections, respectively. The mass-averaged value of the dimensionless temperature for a given cross-section is calculated as in Equation 3.5, substituting θ for T.

The boundary conditions in Equations 3.54 and 3.55 are enforced by simply swapping values between the inflow and outflow boundaries. For the velocities,

$$\mathbf{u}_{1,j} = \mathbf{u}_{i_{max}-1,j} \tag{3.56}$$

$$\mathbf{u}_{i_{max},j} = \mathbf{u}_{2,j} \tag{3.57}$$

and for the temperatures,

$$\theta_{1,j} = \frac{\theta_{i_{max}-1,j}}{\theta_{m,out}} \tag{3.58}$$

$$\theta_{i_{max},j} = \theta_{2,j}\theta_{m,out} \tag{3.59}$$

The boundary pressures are handled by prescribing a constant pressure drop across the length of the domain. For this problem, the relation

$$p(\lambda, y) - p(0, y) = 20\nu \tag{3.60}$$

has been found to be effective. This pressure drop indirectly determines the mass flow through the channel.

3.6 Expressions for Dimensionless Parameters

Because of the complex flow mechanics in wavy passages, it can be difficult to make valid performance comparisons between channels with different geometrical configurations and/or flow

parameters, relying solely on the properties of the flow and temperature fields. Three significant dimensionless parameters help to quantify and evaluate the flow and heat transfer characteristics of the wavy channels. These are: Reynolds number, Nusselt number, and friction factor.

Reynolds number

The Reynolds number is defined as the volumetric flow rate divided by the kinematic viscosity:

$$Re = Q / \nu \tag{3.61}$$

The flow rate for this 2-D passage is defined as:

$$Q = \int_{-H/2}^{H/2} u(x,y)dy = u_{avg}(x)H(x) \tag{3.62}$$

where u_{avg} is the average u-velocity over the entire cross-section at streamwise location x. For the developing flow simulations, a uniform velocity profile is prescribed at the inlet, so the Reynolds number is known in advance to be

$$Re = \frac{u_{avg,in}\, H_{min}}{\nu} \tag{3.63}$$

The value of $u_{avg,in}$ is unity (Equation 3.47) for all the developing flow calculations, so the Reynolds number becomes inversely proportional to the kinematic viscosity for each geometrical configuration.

For fully-developed flow, the velocity profile at the inlet to the computational domain may be continuously changing, so the Reynolds number must be repeatedly recalculated as the flow field evolves. As a result, the Reynolds number for a given set of flow parameters is not known beforehand. As with the developing flow situation, the Reynolds number is dependent only on the kinematic viscosity for a fixed geometry. But now the exact relationship between ν and Re is not known. Appropriate values of ν for a desired Reynolds number regime must be arrived at iteratively. Because ν is the independent variable, the actual Reynolds numbers will not be round values. Also, the flow rate varies over time for unsteady flow, so a time-averaged Reynolds number is used as the defining parameter for a given set of flow conditions.

Nusselt number

The Nusselt number is a parameter that reflects the non-dimensional heat transfer rate at a point on the wall. The local Nusselt number is defined as:

$$Nu(\xi) = \frac{hD_h}{k} = \frac{D_h\left(\partial\theta/\partial\eta\right)_w}{\theta_m(\xi)} \tag{3.64}$$

where H_{avg} was chosen as the hydraulic diameter. The average Nusselt number over a single wavelength is calculated by integrating the local values:

$$Nu_{avg} = \frac{\int_{(n-1)\lambda}^{n\lambda} Nu(\xi)d\xi}{\int_{(n-1)\lambda}^{n\lambda} d\xi} \tag{3.65}$$

where n represents the number of waves downstream from the inlet, beginning with 1. For the developing flow simulations, the time-averaged value of Nu_{avg} for each wave is plotted as a function of n to show how $\overline{Nu_{avg}}$ varies as a function of streamwise location.

Friction factor

To evaluate the pressure drop losses that are incurred from flow through a wavy passage, a dimensionless friction factor is calculated, based on the total pressure drop across a single wavelength:

$$f_{avg} = \frac{\Delta p}{\frac{1}{2}\rho u_{avg,in}^2} = \frac{p((n-1)\lambda) - p(n\lambda)}{\frac{1}{2}\rho u_{avg,in}^2} \tag{3.66}$$

For the developing flow simulations, the time-averaged value of f_{avg} across each wave is plotted as a function of n to show how $\overline{f_{avg}}$ varies as a function of streamwise location.

CHAPTER 4: DEVELOPING FLOW CALCULATIONS

4.1 Computational Details

In the present study, the flow is considered to be two-dimensional with no variation in the spanwise direction. A curvilinear orthogonal grid, generated by solving a pair of elliptic partial differential equations, is used to represent the flow domain (see Section 3.2). The numerical integration of the two-dimensional conservation equations is based on a two-step fractional step procedure with backward Euler differencing of the time derivative and Adams-Bashforth explicit differencing of the convection-diffusion terms (see Section 3.3).

The spatial discretization uses a collocated arrangement with the two Cartesian velocities and the pressure positioned at the centers of discrete finite volumes in the computational domain. The continuity equation is satisfied by the mass fluxes located at the cell faces. The pressure Poisson equation is solved using the conjugate gradient technique without preconditioning. A dimensionless time step of 0.005 was used for all of the developing flow calculations.

Figure 4.1.1 shows a section of the flow domain for which computations were performed. Each passage includes fourteen periodic waves, bounded by two straight sections at the inlet and outlet. The dimensions of the wavy portion of the base passage (Channel #1) were chosen to correspond exactly with those used in the experiments of Nishimura, *et al.* (1984), as well as several subsequent experimental and numerical studies. The wavy channel consists of two

sinusoidally curved wavy walls that are arranged with a mean spacing (H_{avg}) of 1.3 dimensionless units. Each wave has a minimum height (H_{min}) of 0.6 and a maximum height (H_{max}) of 2.0, due to the fact that the amplitude (a) of the sinusoidal walls is 0.35. Each periodic wavelength (λ) spans 2.8 units in the streamwise direction. Two straight sections with height H_{min} and length λ are attached at the entrance and exit of the computational domain. They are added to minimize the effects of the inherent assumptions required to determine the boundary variables.

The two walls in Channel #2 are identical to those of Channel #1. However, the spacing between the walls has been increased by 0.6 units, yielding a mean spacing of 1.9. By comparing the flow and heat transfer and characteristics of the two channels, one can determine the effects of varying the spacing between the two walls while maintaining constant wall dimensions.

For both passages, the Reynolds number was systematically varied by changing the value of the kinematic viscosity while maintaining a constant volumetric flow rate. It should be noted that the flow/temperature fields which were calculated at lower Reynolds numbers were designated as the flow conditions at $t = 0$ for simulations conducted at higher Reynolds numbers. This was done to increase the rate of convergence for the calculations. All of the simulations were carried out for a sufficiently long time so that the initial conditions were completely convected out of the passage, and had no effect on the final results.

During each simulation, the instantaneous u-velocities were monitored to determine the streamwise position in the channel where the onset of instabilities causes the flow to become unsteady. Anywhere upstream of the onset location, the flow will be completely steady. Hence,

for the simulations presented in this chapter, a non-oscillatory time signal in the 14^{th} wave implies that the flow is steady throughout the entire computational domain. This simply means that the onset location for the flow instabilities lies more than 14 waves downstream of the inlet, assuming that the fully-developed flow is unsteady at that Reynolds number. Near the onset location itself, the fluctuations in the flow will be relatively small. However, as the flow proceeds further downstream, the amplitude of the oscillations will grow, until they reach the limit where the flow can be defined as fully-developed.

The velocity "probes" were arbitrarily placed at a height of $0.75H_{max}$ in the tallest part of each wave. Obviously, the values of the velocities that are calculated vary greatly over each wave. However, for this study, the actual values of the monitored velocities are less important than the qualitative nature of the time signals. By focusing on a single point within each wave, it is easy to compare the signals produced at various streamwise locations within the channel, and at various Reynolds numbers. This is important, because previous work has shown that heat transfer enhancement in wavy passages is realized only when the flow is unsteady. It should be noted that the flow will generally be much more oscillatory in the vicinity of the cavities of the channel than near the center. The area where the core and cavity fluid meet is where most of the improved mixing that promotes heat transfer takes place. Thus, the chosen spot for the velocity probes is in a key position. But while the flow may be clearly oscillatory with large-amplitude fluctuations at the probed location, the fluctuations are generally much smaller along the centerline of the channel.

Time signals were also generated for the average friction factors and Nusselt numbers across each wavelength of the passage. If the flow is unsteady, then the time signals for the wave-averaged f and Nu values will be oscillatory, just as the velocity time signals are. However, these can be integrated to produce time-averaged values (see Section 3.6) which are indicative of the average dimensionless heat transfer and pressure drop across each wave of the passage.

All of the developing flow calculations were performed using an orthogonal curvilinear grid containing 64 x 64 internal cells over each wavelength. This translates to an overall computational domain containing 1024 x 64 cells for the fourteen-wave channel (plus the straight inlet and outlet sections). Grid refinement studies have shown that the 64 x 64 grid provides accurate results with a reasonable degree of computational efficiency.

Before performing the final set of calculations that are the subject of this paper, some calculations were performed using coarser grids, in order to determine how much the results of the calculations depend on: i) mesh density, and ii) the overall length of the wavy passage that is modeled. The wave geometry of Channel #1 was used for all of the coarse grid computations. First, simulations were conducted using a 32 x 32 grid for each wave for flow through a passage containing only eight waves, rather than fourteen. Simulations for this case were conducted for Reynolds numbers of 300, 400, 500, and 700. Next similar computations were executed using a 64 x 32 grid for flow through a passage with fourteen waves. By comparing these results with those obtained using a 32 x 32 grid over eight waves, the effects of varying the mesh density and the effects of varying the overall length of the passage can be evaluated simultaneously.

Qualitatively, the results for these two sets of coarse grid calculations showed good agreement. For Re = 300 and Re = 400, the flow was completely steady throughout the entire channel in both cases, producing relatively trivial results. For Re = 500 and Re = 700, u-velocity time signals revealed a transition to unsteadiness at a certain point within the bounds of the channels being investigated. For both Reynolds numbers, this transition occurred at the same position relative to the inlet regardless of the total length of the channel. Furthermore, the patterns of the time signals did not vary with the refinement of the grid. However, in order to ensure the highest possible degree of accuracy within the constraints of available computational resources, 64 x 64 cells per wave are employed for all of the results that follow, both for the developing flow results presented within this chapter, and for the fully-developed flows addressed in Chapter 5.

Computations were performed on a Silicon Graphics PowerChallenge Array, and also on Pentium-based PC's. In either case, approximately two weeks real time was required to complete a single developing flow simulation. The PowerChallenge Array required fewer total CPU hours per simulation. But because the simulations were so lengthy (approximately 12 CPU hours for 5000 time steps), each simulation had to be divided into manageable segments. The turnaround time between runs, combined with the dilution of computational resources among several users, severely lengthened the runs. Consequently, no real time was lost by executing the program on a dedicated Pentium PC.

4.2 Channel #1 (H_{avg} = 1.3)

Calculations were performed using a 64 x 64 mesh for each wavelength, for flow through a 14-wave passage, at Re = 300, 500, 600, 700. This provides a representative sampling of developing flow in a wavy passage in the regime where transition to an oscillatory state takes place. These simulations use the wave dimensions described in Section 4.1, where the average separation distance between the top and bottom walls is equal to 1.3 units.

Figure 4.2.1 shows the u-velocity time signal in wave 14 for Re = 300. At Re = 300, it is evident from the time signals that the flow becomes steady throughout the entire passage immediately after the initial conditions are convected out of the channel. The streamline plot in Figure 4.2.2 shows single trapped vortices in the cavities and almost perfectly straight core flow. These are expected patterns for steady flow in a wavy passage (Wang and Vanka, 1995). From the isotherm plot in Figure 4.2.3, one can see that the warm core fluid passes straight through the center of the passage, without significantly mixing with the cooler fluid near the walls. This shows that when the flow is steady, only minimal increases in heat transfer rates can be expected, due to the fact that the cooler fluid becomes isolated in the large recirculating vortices that fill the two furrows of each wave. The quantitative heat transfer performance of the wavy passage is addressed later in this section.

The coarse grid calculations discussed in Section 4.1 revealed that the flow is also steady at Re = 400, and consequently, exhibits the same behavior observed at Re = 300. In the interest of saving computer time, those calculations were not repeated using the finer mesh.

At Re = 500, however, the flow behavior becomes more interesting. Looking at the time signals for waves 8, 10, 12, and 14 in Figure 4.2.4, one can see a unique pattern developing. For a certain period of time, the time signal does not fluctuate significantly, and the flow appears to be steady, leading to flow and temperature profiles similar to what is seen in Figures 4.2.2 and 4.2.3 for the Re = 300 case. Then, suddenly, large oscillations appear in the time signals. The resulting flow pattern contains multiple vortices and divergent core flow, especially in the last two waves of the passage, as shown in Figure 4.2.5. Thus, the temperature profile in Figure 4.2.6 reveals better mixing of the core and near-wall fluid. This unsteady flow lasts for a certain amount of time, until the oscillations quickly die out, and the flow becomes steady again. After awhile, the cycle repeats itself. Thus, beginning eight waves downstream and continuing at least through the fourteenth wave, the flow is "intermittently" unsteady. It is unsteady for a certain period of time, and steady for the rest of the time. However, the time signals indicate that the fluctuating sections become longer as the flow moves downstream. The period of time that the flow is unsteady also increases. By the fourteenth wave, there are small oscillations in the portion of the signal where the flow is completely steady in the upstream waves.

Figure 4.2.7 shows the percentage of time that the flow is unsteady at Re = 500, plotted as a function of streamwise location. The flow is completely steady through the sixth wave downstream, but by the twelfth wave, the flow is unsteady almost 80% of the time. This is crucial information, because heat transfer enhancement is not realized while the flow remains steady. Intermittently unsteady flow was also observed in the experiments of Greiner *et al.* (1990) at

comparable Re for flow in a channel with a triangular grooved wall. However, the intermittency only existed over a small range of Reynolds numbers.

At Re = 600, the flow is oscillatory beginning at the fifth wave, and is completely unsteady downstream of this point. The time signals in Figure 4.2.8 do not display the intermittent behavior seen in the Re = 500 case. Again, though, the amplitude of the oscillations does increase as the flow progresses downstream. Through the tenth wave, the oscillations are fundamentally periodic with a single dominant frequency, but further downstream, multiple frequencies are present in the signals. The instantaneous streamline plot in Figure 4.2.9 and the instantaneous isotherm plot in Figure 4.2.10 reflect the unsteady behavior triggered by instabilities in the flow.

Finally, at Re = 700, the flow is unsteady beginning at the third wave. And once again, the oscillations are completely self-sustaining downstream of this point, with their amplitude increasing as the flow proceeds downstream. The time signals in Figure 4.2.11 exhibit patterns similar to those of the Re = 600 case. The flow is basically periodic with a single frequency through the eighth wave, but multiple frequencies are introduced downstream of this point. The instantaneous streamline plot in Figure 4.2.12 exhibits the multiple vortices and divergent core flow that result from the oscillatory nature of the flow. In the instantaneous isotherm plot in Figure 4.2.13, there is obviously far more mixing between the core and near-wall fluid than there would be if the flow was steady.

The time-averaged values for the friction factors and Nusselt numbers averaged across each wavelength are plotted in Figures 4.2.14 and 4.2.15, respectively, as a function of wave

location relative to the inlet for all four Reynolds numbers investigated using this geometrical configuration. Note that two sets of data are presented for Re = 500. One set of quantities was tabulated during the time the flow was steady, and the other set was obtained while it was unsteady.

In Figure 4.2.14, $\overline{f_{avg}}$ is very low in the first wave of the channel. Because the boundary layers have developed through the straight section, the velocity profile entering the first wave is more parabolic than for flow entering the narrow portions of subsequent waves. By the second wave, the friction factor has reached a value that remains constant as long as the flow is steady. Thus, for Re = 300, $\overline{f_{avg}}$ is basically the same for each wave from wave 2 through the final wave of the passage. As expected, $\overline{f_{avg}}$ decreases as Re increases for steady laminar flow. For higher Re, however, there is a noticeable increase in the friction factor once the flow becomes unsteady.

Figure 4.2.15 clearly reveals how unsteady flow in a wavy channel can enhance heat transfer, while steady flow in the same geometry produces only minimal benefits. For Re = 300, and the steady flow at Re = 500, the Nusselt number remains virtually constant throughout the passage, beginning at the second wave from the inlet. The slight increases in the last few waves for the Re = 500 case is due to the fact that in these locations, the flow is still slightly oscillatory even during the time when the flow is considered "steady". However, these oscillations are tiny compared with those which occur when the flow is fully unsteady. For steady flow at Re = 300 and 500, the values of $\overline{Nu_{avg}}$ are not substantially greater than the Nu = 7.54 yielded by a straight channel. When the flow is unsteady at Re = 500, though, the Nusselt number rises

significantly beginning in the eighth wave, at the onset location for unsteady flow. At Re = 600, in the portion of the passage where the flow is steady, the Nusselt number remains constant from wave to wave, and is only slightly higher than for steady flow at Re = 500. However, once the flow becomes unsteady, beginning around the fifth wave, the value of $\overline{Nu_{avg}}$ begins to increase dramatically as the flow travels downstream. This rate of increase becomes even larger once the oscillations begin to exhibit markedly increased amplitudes, accompanied by multiple frequencies, around the twelfth wave. By the end of the wavy passage, the time-averaged Nusselt number is almost twice as large as the value in the waves near the inlet where the flow is completely steady. At Re = 700, the Nu plot is similar to that for Re = 600, but now the onset location is the third wave, corresponding to the area where Nu begins to increase. The values of $\overline{Nu_{avg}}$ are higher throughout the passage, exceeding 23 by the fourteenth wave.

Comparing the Nusselt number plot in Figure 4.2.15 with Table 4.1, which gives the onset location for each Re examined here, one can see that the initial increases in $\overline{Nu_{avg}}$ coincide exactly with the point where the flow becomes unsteady. The friction factor also increases when the flow becomes unsteady, but the correspondence between this increase and the onset location is not quite as direct as for Nu. At Re = 500, the growth in f does begin at the onset location in wave 8, when the flow is unsteady. But at Re = 600 and 700, $\overline{f_{avg}}$ remains constant for a few waves after the initial onset location, before finally rising. Looking at the time signals, though, it appears that this increase begins instead at the point where multiple frequencies are introduced to the flow, complementing the continually rising amplitudes of oscillation. So, there is a decoupling of the heat transfer and pressure drop mechanisms, but only over a few wavelengths.

Reynolds number	First wave of unsteadiness
300	> 14
400	> 14
500	8
600	5
700	3

Table 4.1 Onset location for unsteady flow as a function of Reynolds number for Channel #1

4.3 Channel #2 ($H_{avg} = 1.9$)

The simulations presented in this section use the wave dimensions described in Section 4.1, but with the average separation distance between the top and bottom walls equal to 1.9 units. This geometry was considered to investigate the effect of the channel height on the flow dynamics. The dimensions for Channel #2 were chosen, because it has $H_{min} = 1.2$, which is equal to twice the inlet height of Channel #1. Thus, it is possible to observe the effects of doubling the inlet height while maintaining a constant wall geometry.

For $Re = Q / \nu$, the inlet height is the dimension that determines Re, if the inlet velocity is held constant, as it is here. But it is possible that the dimension which has the greatest impact on the flow mechanisms may be the amplitude of the wave. Choosing another dimension would change the actual value of Re for a given set of flow conditions. Regardless, $Re = Q / \nu$ is used here, because this definition has a physical meaning that is easily understood. And, this Re

directly reflects the change in the separation distance between the two plates. Expanding the distance between the two walls increased the Reynolds number at which the flow became unsteady, at least for the Re as it is defined in this paper. Consequently, simulations for this geometry were conducted for Re = 300, 500, 700, 1000, and 1400.

When the flow is completely steady, the flow and temperature mechanisms are very similar to those of the narrower channel. Figure 4.3.1 shows the u-velocity time signal in wave 14 for Re = 300. From Figure 4.3.1, it is evident that at Re = 300 the flow becomes steady throughout the entire passage immediately after the initial conditions are convected out of the channel. The streamline plot in Figure 4.3.2 shows the familiar pattern of single trapped vortices in the cavities accompanied by straight core flow. But now, the ratio of the amount of fluid in the cavities to that flowing through the core is much smaller. From the isotherm plot in Figure 4.3.3, one can see that the warm core fluid passes straight through the wide center of the passage, essentially unperturbed by the furrows along the walls. As discussed previously, wavy passages are not effective enhancement devices when the flow is steady. And, with the increased channel height, the steady heat transfer rates are even lower than before. The quantitative heat transfer performance of the wavy passage is addressed further later on.

As with the previous geometry, the Reynolds number was then increased from 300 to 500. But this time, the flow became steady at this Reynolds number as well. At Re = 700, instabilities in the initial flow field triggered oscillations shown in the time signal in Figure 4.3.4, but these oscillations were not self-sustaining, and disappeared after the initial conditions were convected out of the channel. The steady state flow patterns for Re = 500 and 700 look exactly like the plot

in Figure 4.3.2 for Re = 300. The corresponding isotherm plots are also very similar, with the exception of increased temperature gradients within the channel. But the general patterns are the same, and there is still only minimal mixing between the core and near-wall fluid.

It is clear that increasing the wall spacing causes the flow to remain stable at higher Reynolds numbers. Once the Re was increased to 1000, however, the flow did become unsteady. The flow is unsteady beginning at the sixth wave, and the oscillations feature a single dominant frequency throughout, as shown in Figure 4.3.5. The instantaneous streamline plot in Figure 4.3.6 features multiple vortices, as seen with unsteady flow in the narrower channel. But here, a larger amount of fluid passes straight through the center of the channel, virtually unaffected by the instabilities triggered by the wavy walls. The instantaneous isotherm plot in Figure 4.3.7 confirms that there is some increased exchange between the core and near-wall fluids, but the warmest fluid still proceeds straight down the center of the channel.

Finally, at Re = 1400, the flow is unsteady beginning in the fourth wave. The flow is always unsteady, but the amplitude of the oscillations varies intermittently over some of the channel, as shown in Figure 4.3.8. But by the 14^{th} wave of the passage, the fluctuations remain large for the entire time, once the transients die out. The instantaneous streamline and isotherm plots in Figures 4.3.9 and 4.3.10, respectively, are very similar to the corresponding plots for Re = 1000 in Figures 4.3.6 and 4.3.7. Although there are multiple vortices and improved mixing, a significant portion of the fluid still flows straight through the center of the channel, with minimal fluctuations in velocity.

The time-averaged values for the friction factors and Nusselt numbers averaged across each wavelength are plotted in Figures 4.3.11 and 4.3.12, respectively, as a function of wave location relative to the inlet for all five Reynolds numbers investigated using Channel #2. In Figure 4.3.11, $\overline{f_{avg}}$ is very low in the first wave of the channel, due to the near-parabolic profile of the flow entering from the straight section. Then, after peaking in the second wave, it decreases slowly over the next few wavelengths. The exact length of this decrease depends on Re. Because the distance between the two walls has been extended, the shear layers take even longer to develop than before. Once the boundary layers have formed, the friction factor remains essentially constant for a given Re, as long as the flow is steady. Thus, for Re = 300, 500, and 700, $\overline{f_{avg}}$ is basically the same for each wave from wave 5 through the wave 13, with a slight upturn in the final wave of the passage, due to the permanent contraction of the channel to H_{min}. As expected, $\overline{f_{avg}}$ decreases as Re increases for steady laminar flow. It is seen that, even at higher Re, this trend continues, at least over the length of the channel modeled here. When the flow becomes unsteady, there are slight fluctuations in $\overline{f_{avg}}$, but nothing remotely approaching the sharp increase that occurs with unsteady flow in the narrower channel.

Figure 4.3.12 shows that the rates of heat transfer for the wavy passage are again directly determined by whether or not the flow is unsteady. Increasing Re only produces small gains in Nu as long as the flow is steady. For Re = 300, 500, and 700, the Nusselt number remains virtually constant through most of the passage, once the shear layers have developed fully. The

length needed for this development increases with Re, but in all three cases, $\overline{Nu_{avg}}$ settles to a value only slightly greater than the Nu = 7.54 yielded by a straight channel.

At Re = 1000 and 1400, $\overline{Nu_{avg}}$ once again begins decreasing over the first few waves of the channel. But once the transition to unsteadiness takes place, $\overline{Nu_{avg}}$ undergoes a rapid rise before peaking a few waves later, at which point it slowly decreases. For Re = 1000, this decrease continues through the final wave, but at Re = 1400, $\overline{Nu_{avg}}$ levels out and even begins to slowly increase again. Also, over the last 6 waves of the passage, $\overline{Nu_{avg}}$ is noticeably larger for the Re = 1000 case than for Re = 1400. There could be several reasons for this. Firstly, there is the intermittent nature of the time signals for Re = 1400. If $\overline{Nu_{avg}}$ is calculated only where the oscillations are largest, then it will be much higher than the value obtained when integrating over both the small and large fluctuation cycles. In a related issue, it is possible that the amount of time over which the flow properties were sampled was not large enough in this instance to provide the most accurate time-averaged values. More likely, though, the channel must be more than 14 waves long before the temperature profiles reach a pseudo-steady state. Farther down the hypothetical periodic passage, $\overline{Nu_{avg}}$ may be higher at Re = 1400 than at Re = 1000.

Comparing the Nusselt number plot in Figure 4.3.12 with Table 4.2 which provides the onset location for each Re investigated here, one can see that the initial increases in $\overline{Nu_{avg}}$ coincide exactly with the points where the flow becomes unsteady. But the behavior of the friction factor undergoes only minimal changes due to the unsteady flow. For this geometry, there

is a strong decoupling of the heat transfer and pressure drop mechanisms within the computational domain modeled here. This decoupling would have a very favorable effect on heat exchange performance, because $\overline{f_{avg}}$ decreases with increasing Re for laminar flow while $\overline{Nu_{avg}}$ increases due to the enhanced mixing provided by oscillatory flow. However, one may recall that for the narrower channel, there was also a temporary decoupling over the course of a few wavelengths, before $\overline{f_{avg}}$ also began to increase further downstream. Thus, it is likely that $\overline{f_{avg}}$ will begin to increase further down a passage with the geometry of Channel #2 as well. But more than 14 wavelengths would be required before this will occur.

Reynolds number	First wave of unsteadiness
300	> 14
500	> 14
700	> 14
1000	6
1400	4

Table 4.2 Onset location for unsteady flow as a function of Reynolds number for Channel #2

CHAPTER 5: FULLY-DEVELOPED FLOW CALCULATIONS USING PERIODIC B.C.'s

5.1 Computational Details

As with the developing flow simulations, the flow and energy equations are solved on a two-dimensional curvilinear orthogonal mesh, using a collocated fractional step scheme. A few subtle adjustments were made to accommodate the fully-developed flow. For these simulations, the computational domain consisted solely of one wave. Wang and Vanka (1995) demonstrated that only a single wavelength was needed to model fully-developed flow in wavy passages when using periodic boundary conditions at the inlet and outlet of the domain, as presented in Equations 3.56-3.59.

Instead of directly specifying the mass flow through the channel, a constant pressure gradient is prescribed across each wavelength, using the relationship in Equation 3.60. Because ν is the independent variable, appropriate values of ν for a desired Reynolds number regime must be arrived at iteratively. Consequently, the actual Reynolds numbers may not be round values. The dimensionless time step was varied with the purpose of employing the largest feasible time step that would yield a stable and accurate solution. Lower Reynolds numbers required smaller time steps, due to the diffusive stability restrictions. Actual time steps ranged from 0.001 to 0.01, depending on the Reynolds number and the geometrical configuration being investigated.

Six u-velocity probes were arbitrarily placed throughout the wave in order to monitor the fluctuations in the flow at various points throughout the domain. These time signals indicated whether the fully-developed flow was steady or unsteady, once a stationary solution had been obtained. Probes were placed along the y-centerline and at 0.75H near the inlet and outlet of the domain, and along the x-centerline. The fluctuations along the y-centerline were always smaller than those which occurred at 0.75H. For ease of comparison, the time signals presented throughout the remainder of Chapter 5 indicate the behavior of the u-velocity at 0.75H along the x-centerline. This is the same point that was used to generate the time signals for the developing flow simulations in Chapter 4. Time signals were also generated for the average friction factors and Nusselt numbers across the domain. These values were integrated to produce time-averaged quantities (see Section 3.6) which are indicative of the average dimensionless heat transfer and pressure drop across each wave of the passage.

All of the fully-developed flow calculations were performed using an orthogonal curvilinear grid containing 64 x 64 internal cells. Grid refinement studies have shown that the 64 x 64 grid provides accurate results with a reasonable degree of computational efficiency (Wang and Vanka, 1995). This mesh is 1/16 as large as the mesh required for the developing flow calculations discussed in Chapter 4. Also, the solution for the pressure field, which limits the speed of the computation, converges monotonically, and in fewer iterations than for the fully-developed case. Thus, far less computational time was required. All simulations discussed in this chapter were performed using Pentium-based PC's. A single simulation could take up to 20 hours, but many required fewer than 5 hours. Because the fully-developed flow calculations are

less cumbersome, they allow for more comparisons between wavy passages with different dimensions.

In the remainder of Chapter 5, the effects of varying three different dimensions of the wavy passage are analyzed. In Section 5.2, results are presented for fully-developed flow in the base channel. In Section 5.3, the height, or separation distance between the two walls, is varied. In Section 5.4, the amplitude of the wavy walls is varied, while maintaining a constant average separation distance. And in Section 5.5, the wavelength of the walls is varied. In all three cases, the geometry which serves as the basis for comparison has the same wave dimensions as Channel #1 in Chapter 4:

$$H_{avg} = 1.3, \quad a = 0.35, \quad \text{and} \quad \lambda = 2.8 \tag{5.1}$$

For each dimension that is examined, two additional configurations are compared to the base geometry: one where the parameter in question is less than the value in Equation 5.1, and one where it is greater. The other two dimensions are held constant.

5.2 Base Channel

For fully-developed flow through the base channel, the flow was observed to become unsteady around Re = 190. In the finite-length Channel #1 addressed in Chapter 4, self-sustaining oscillations were not observed in the 14-wave domain below Re = 500. For lower Reynolds numbers, the instabilities develop slowly over a long entrance length.

Representative time signals for the base channel are presented in Figures 5.2.1 and 5.2.2. In both cases, a single dominant frequency is evident, but additional frequencies are present as well. Between Re = 268 and Re = 425, the amplitude of the oscillations remains essentially the same. Figure 5.2.3 shows the streamlines for steady flow. As with the developing flow cases, steady flow yields single recirculating vortices in each of the cavities, accompanied by straight core flow. This pattern was observed for steady flow in all of the passages considered here, regardless of the specific dimensions. A single trapped vortex fills each of the cavities, regardless of the actual cavity size. Altering the wave dimensions changes the flow patterns only in the unsteady regime.

An instantaneous streamline plot for unsteady flow in the base channel is given in Figure 5.2.4. The specific pattern will vary with time, but the unsteady flow always produces increased mixing and heat transfer rates for all of the wavy passages. This can be seen for the base channel in Figure 5.2.5. For steady flow, the Nusselt number remains constant at a value around 9, regardless of Reynolds number. Once the flow becomes unsteady, though, $\overline{Nu}_{avg}$ steadily increases with Reynolds number. After a slight increase in friction factor when the flow first becomes unsteady, $\overline{f}_{avg}$ continues to decrease with Re. However, the *rate* of this decrease slows down as Re is increased. Hence, there comes a point where increasing Re renders diminishing benefits in heat transfer performance. The optimal value of Re depends on the specific criteria for evaluating performance, and on the dimensions of the passage. But it is known that wavy passages generally offer the best enhancement in the transitional regime. For flow in this regime,

the base channel is now compared to passages where the height, amplitude, and wavelength are individually varied.

5.3 Height Variation

For the base channel, H_{avg} = 1.3. With a = 0.35, this yields a minimum separation distance, H_{min} = 0.6. The other two values of H_{avg} that are investigated are 1.0 and 1.9. These two values were chosen because they represent a halving and doubling, respectively, of H_{min} relative to the base case. The approximate transition Reynolds numbers for the three different heights are given in Table 5.1.

H_{avg}	Transition Re
1.0	130
1.3	190
1.9	240

Table 5.1 Transition Reynolds number as a function of H_{avg}

Decreasing the channel height causes the flow to become significantly less stable. Figure 5.3.1 shows the time signal at Re = 182 for the narrower channel. The signal is periodic with a single frequency. This changes when the Reynolds number is increased. The time signal for Re = 400 is given in Figure 5.3.2. Now, several frequencies are present, including a dominant low frequency. Also, the amplitude of the fluctuations is much greater. This more chaotic behavior is reflected in the streamline plot in Figure 5.3.3. The patterns of the friction factor and Nusselt

number plots in Figure 5.3.4 are more chaotic as well. The actual values of the friction factor are much greater than for the base case, because the expansion ratio (H_{max} / H_{min}) has increased by 70%, leading to increased pressure drop. However, the Nusselt numbers are also somewhat larger.

Expanding the channel height causes the flow to become more stable. Figures 5.3.5 and 5.3.6 show two representative time signals for the wider channel. The signal is periodic with a single frequency in both cases. As the Reynolds number is incremented, the frequency of the oscillations becomes smaller, while their amplitude becomes greater. Although the streamline plot in Figure 5.3.7 exhibits divergent core flow and irregular vortices, the flow pattern is not nearly as chaotic as for the narrower channel, even at Re = 1001. The friction factor and Nusselt number plots in Figure 5.3.8 follow smooth patterns. The Nusselt number increases linearly with Re once the flow becomes unsteady, while the rate of decrease in the friction factor slowly levels off. The values of the friction factor are equal to about 1/3 of those for corresponding Reynolds numbers with the base case, but the Nusselt numbers are lower as well.

5.4 Amplitude Variation

For the base channel, the amplitude of the sinusoidal wavy walls, a = 0.35. The other two values of a that are investigated are 0.25 and 0.50. H_{min} and H_{max} will change as the amplitude is varied, but H_{avg} is held constant at 1.3. The approximate transition Reynolds numbers for the three different amplitudes are given in Table 5.2.

a	Transition Re
0.25	245
0.35	190
0.50	135

Table 5.2 Transition Reynolds number as a function of the amplitude of the wavy walls

The results produced by increasing the amplitude of the walls are similar to those obtained for the narrowest passage described in Section 5.3. The flow became significantly less stable as the amplitude was increased. Figure 5.4.1 shows the time signal at Re = 174 for the channel with a = 0.50. The signal is periodic with a single frequency. But when the Reynolds number is increased, multiple frequencies emerge, including a dominant low frequency, as in Figure 5.4.2 for Re = 363. Figure 5.4.3 shows a corresponding streamline plot for this Reynolds number. This geometry has an expansion ratio equal to 2.3 times that of the base geometry, so the friction factors in Figure 5.4.4 are even higher than for those for H_{avg} = 1.0. However, the friction factor and Nusselt number obey more conventional functions of Reynolds number. They follow the trends observed for the base case, and for all the other geometries with less severe expansion ratios discussed in this chapter.

Decreasing the amplitude from the base case caused the flow to become more stable. Figures 5.4.5 and 5.4.6 show time signals for the passage with a = 0.25 at Re = 260 and Re = 668, respectively. At Re =260, the signal is periodic with only a single frequency. At Re = 668, the signal is basically periodic, but there is an underlying low frequency that manifests itself over

long periods of time. A corresponding streamline plot for this Reynolds number is given in Figure 5.4.7. Friction factor and Nusselt number are plotted vs. Reynolds number for this geometry in Figure 5.4.8. $\overline{f_{avg}}$ actually increases between Re = 572 and Re = 668. $\overline{f_{avg}}$ would eventually begin increasing with Reynolds number for the other configurations as well, but this increase occurs at higher Reynolds numbers than those that are considered here.

5.5 Wavelength Variation

For the base channel, $\lambda = 2.80$. The other two values of λ that are investigated are 2.24 and 3.36. These two values were chosen because they represent a 20% decrease and increase, respectively, of λ relative to the base case. This variation was examined experimentally by Rush (1997) for developing flow. The approximate transition Reynolds numbers for the three different wavelengths are given in Table 5.3.

λ	Transition Re
2.24	175
2.80	190
3.36	195

Table 5.3 Transition Reynolds number as a function of wavelength

Varying the wavelength produced only minimal differences in the flow behavior, even between the passages with the smallest and largest wavelengths. The transition Reynolds number

is similar for all three cases. Figure 5.5.1 shows the time signal at Re = 189 for the channel with the shortest wavelength. The signal is periodic with a single frequency. Figure 5.5.2 shows the time signal after the Reynolds number is increased to 492. The signal still follows a predictable periodic pattern. A corresponding streamline plot for this Reynolds number is given in Figure 5.5.3. Friction factor and Nusselt number are plotted versus Reynolds number in Figure 5.5.4. For varying wavelength, the friction factors have been calculated based on a projected pressure drop over the base wavelength of 2.80. The resulting values of $\overline{f_{avg}}$ are become larger as the wavelength is compressed. But the effect of reducing the wavelength is not nearly as pronounced as that of decreasing the channel height or increasing the amplitude of the walls.

Figure 5.5.5 shows the time signal at Re = 213 for the passage $\lambda = 3.36$. As expected for a Reynolds number just above the transtion number, the signal is periodic. Figure 5.5.6 shows the time signal at Re = 443. Although the signal follows a distinct pattern, multiple frequencies are evident, and the amplitude of the oscillations is not constant. A corresponding streamline plot for this Reynolds number is given in Figure 5.5.7. Friction factor and Nusselt number are plotted versus Reynolds number for this geometry in Figure 5.5.8. The value of $\overline{Nu_{avg}}$ at a given Reynolds number remains essentially the same for all three of the wavelengths addressed in this section.

CHAPTER 6: SUMMARY AND CONCLUSIONS

In the current study, the time-dependent governing equations for flow and heat transfer in wavy passages are solved on a 2-D curvilinear mesh using an accurate numerical scheme. Computations have been performed for developing flow in the entrance length of the passage, and for periodic fully-developed flow conditions. The data for developing flow in the entrance length of the passage supply new information about how long a wavy channel must be for the flow to become unsteady. Periodic fully-developed flow calculations were used to make comparisons between wavy passages with different dimensions.

Flow patterns have been examined in the developing portion of two wavy passages. The first channel studied corresponds to the geometry of Nishimura, *et al.* (1984). For Re = 300 and 400, more than fourteen waves are needed for the flow instabilities to develop. At Re = 500, the flow becomes unsteady beginning at the eighth wave downstream from the inlet. Furthermore, the unsteadiness is observed to be intermittent. For Re = 600, completely self-sustaining oscillations are evident as far upstream as the fifth wave, and at Re = 700, the unsteady behavior is present in the third wave. When the inlet height of the channel is doubled, the flow remains stable at higher Reynolds numbers. Thus, it appears that the transition Reynolds number may be one that is defined based on wave height, not channel height. For this configuration, the flow is steady through the entire fourteen-wave passage at least up to Re = 700. The flow was observed to become unsteady in the sixth wave for Re = 1000, and in the fourth wave for Re = 1400.

For both channels, there was minimal heat transfer enhancement under steady flow conditions, regardless of Reynolds number. When the Reynolds number was high enough to trigger flow instabilities within the computational domain, the wave-averaged Nusselt number showed a marked increase beginning at the onset location for unsteady flow. A corresponding rise in the friction factor occurred shortly after, indicating a moderate decoupling of the heat transfer and pressure drop mechanisms.

Information about the developing section of the channel is crucial, because effective heat transfer enhancement cannot be realized unless the flow is unsteady. However, calculations for developing flow are quite lengthy, because the flow patterns must be accurately resolved over a computational domain equal to the entire length of the finite passage being modeled. This makes it difficult to investigate developing flow for diverse geometrical configurations. Computations for fully-developed flow are less troublesome, because periodic boundary conditions allow the computational domain to be reduced to a single wavelength. Here, fully-developed flow calculations are used to expand the parameter space under consideration. Three different dimensions of the wavy passage were separately varied, and their effects on flow and heat transfer behavior were observed.

The channel which serves as the basis for comparison has the same geometry as Channel #1 for the developing flow calculations (Nishimura, *et al.*, 1984). For each dimension that is examined, two additional configurations are compared to the base geometry: one where the parameter in question is less than the corresponding value for the base case, and one where it is greater. The other two dimensions are held constant.

First, the height, or separation distance between the two walls, was varied. Decreasing the height caused the flow to become less stable, meaning that the flow became unsteady at a lower Reynolds number. The friction factor increased, due in part to an increase in the expansion ratio (H_{max} / H_{min}), but the Nusselt number rose as well. Similar trends were observed when the amplitude of the wavy walls was modified, while maintaining a constant average separation distance. Increasing the amplitude promoted flow instabilities, and resulted in the highest friction factors of any of the configurations for which fully-developed calculations were conducted. Lastly, the wavelength was varied by 20% in either direction to complement a concurrent experimental study (Rush, 1997). This had a minimal effect on the flow behavior and stability. The friction factor increased slightly as the wavelength was decreased. The Nusselt number for any given Reynolds number remained essentially constant regardless of wavelength.

The results presented in this thesis strengthen our understanding about how heat exchangers can be made more compact and efficient using wavy channels. This report can be added to the growing body of work pertaining to this topic.

FIGURES

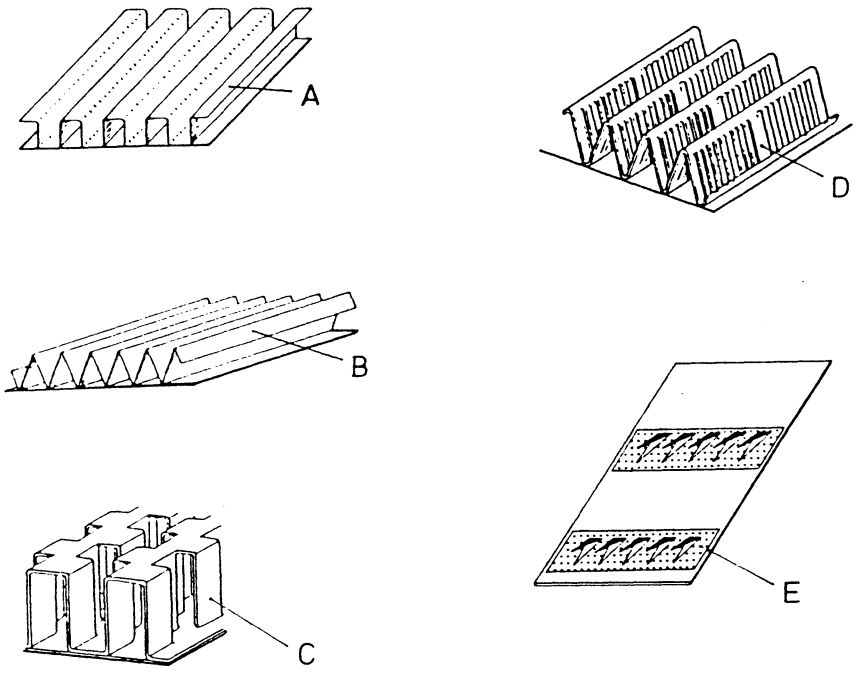

Figure 2.1.1 (A) Rectangular plain fins, (B) triangular plain fins, (C) offset strip fins, (D) louvered fins, (E) vortex generators (Brockmeier, *et al.*, 1993)

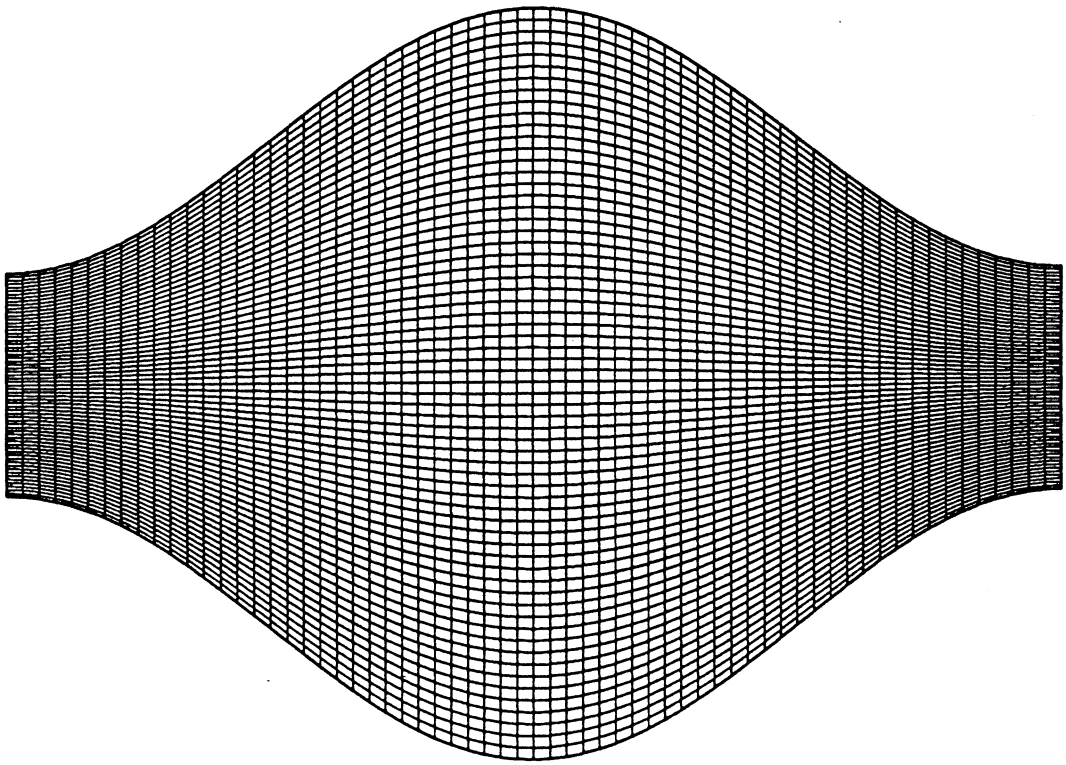

Figure 3.2.1 Initial non-orthogonal mesh for a single wave

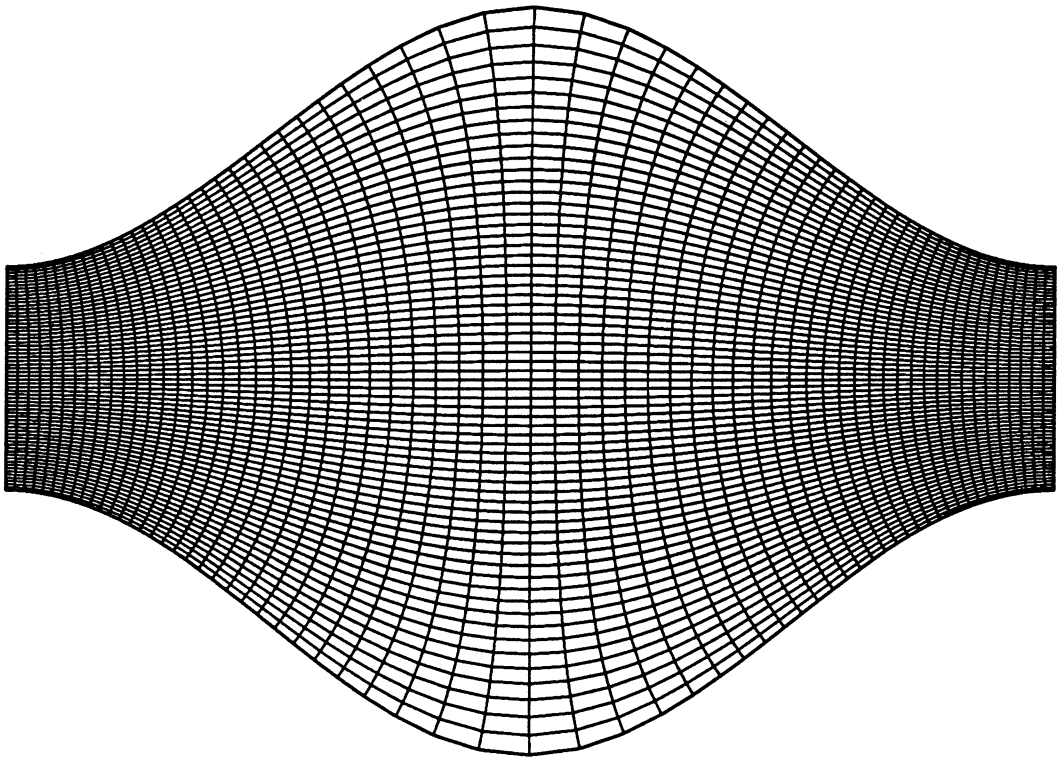

Figure 3.2.2 Orthogonal mesh for a single wave

Figure 3.2.3 Sixteen-wavelength passage for developing flow simulations

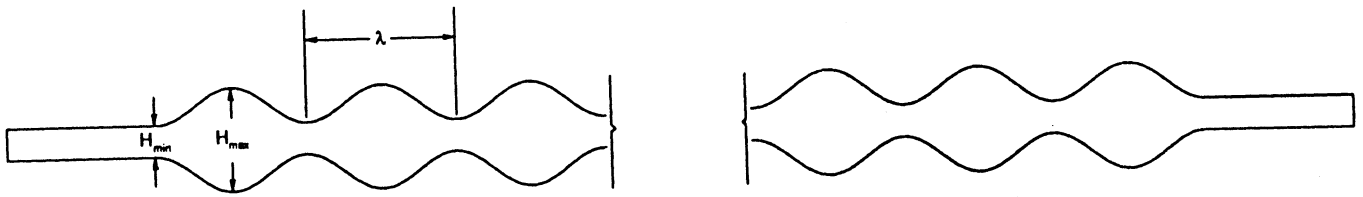

Figure 4.1.1 Schematic of computational domain for developing flow simulations

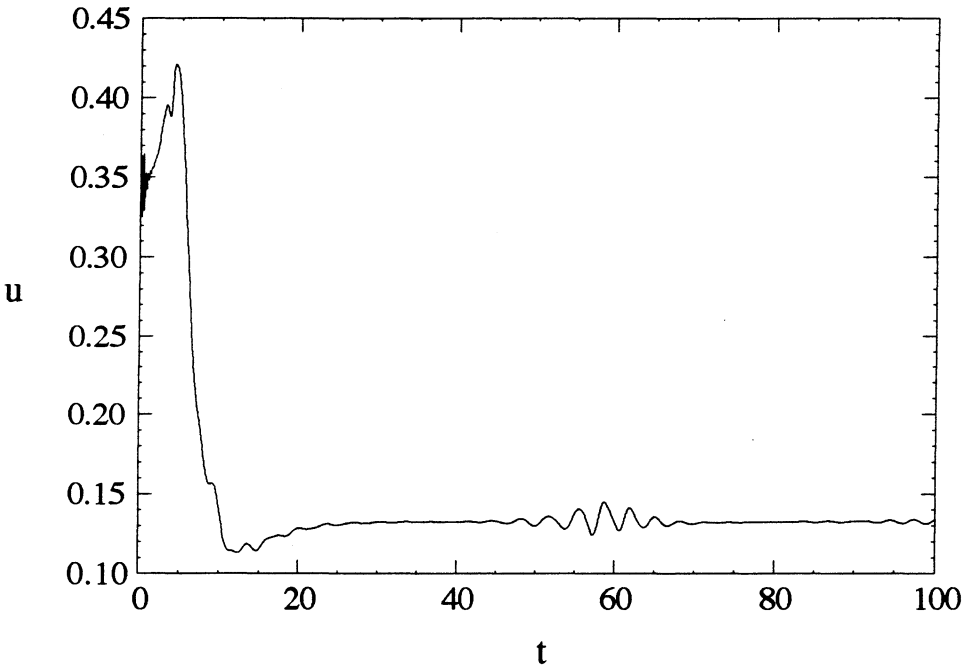

Figure 4.2.1 Time signal for u-velocity in 14th wave of Channel #1 at Re = 300

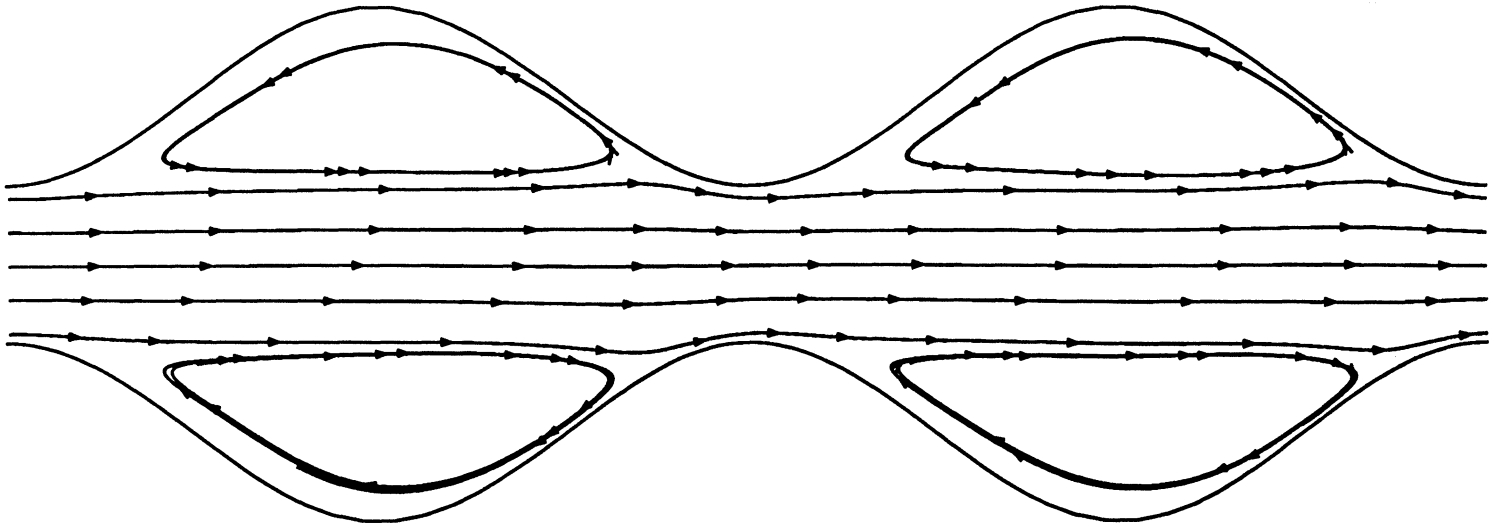

Figure 4.2.2 Instantaneous streamline plot in 13th and 14th waves of Channel #1 at Re = 300

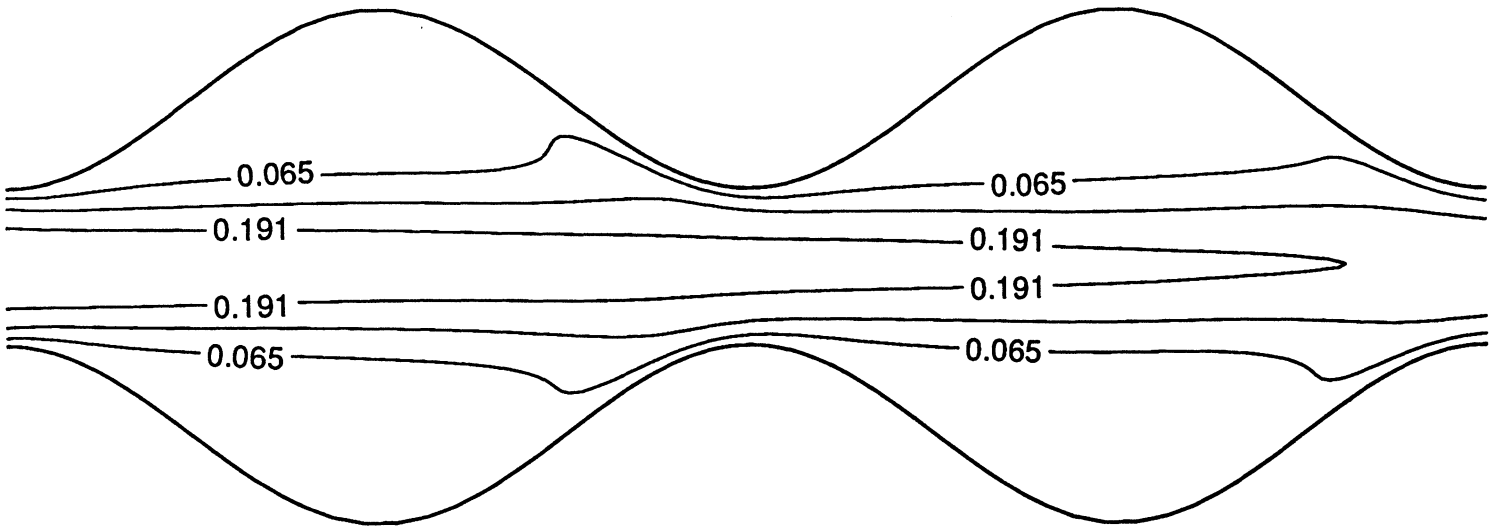

Figure 4.2.3 Instantaneous isotherm plot in 13th and 14th waves of Channel #1 at Re = 300

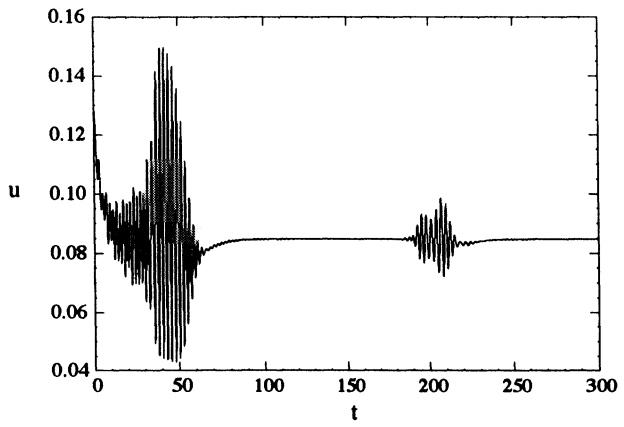

(a)

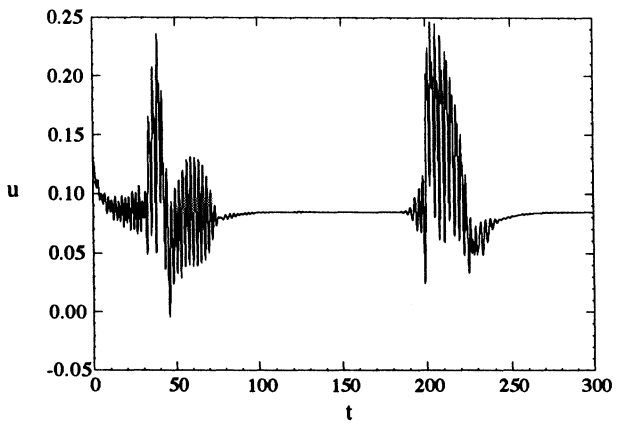

(b)

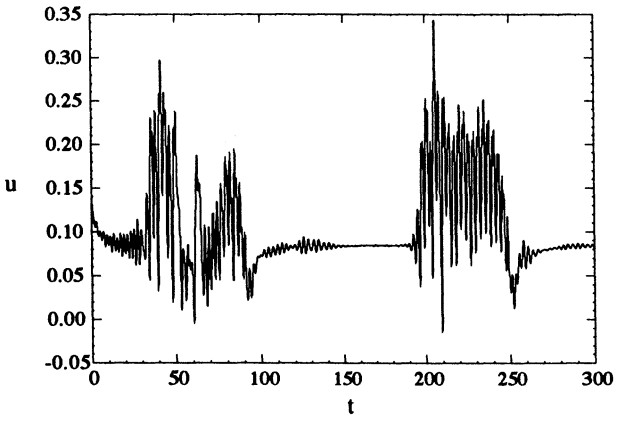

(c)

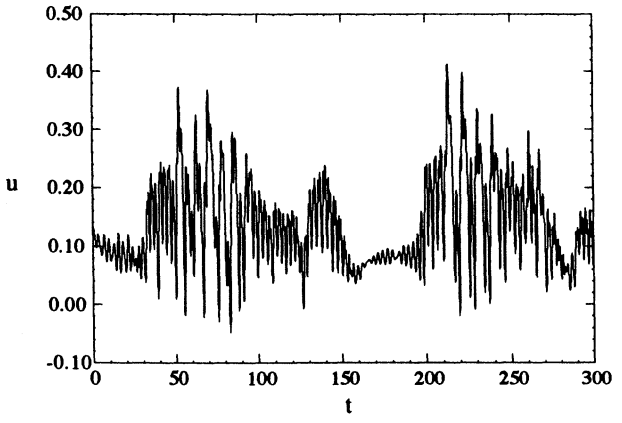

(d)

Figure 4.2.4 Time signals for u-velocity in Channel #1 at Re = 500
(a) Wave 8 (b) Wave 10 (c) Wave 12 (d) Wave 14

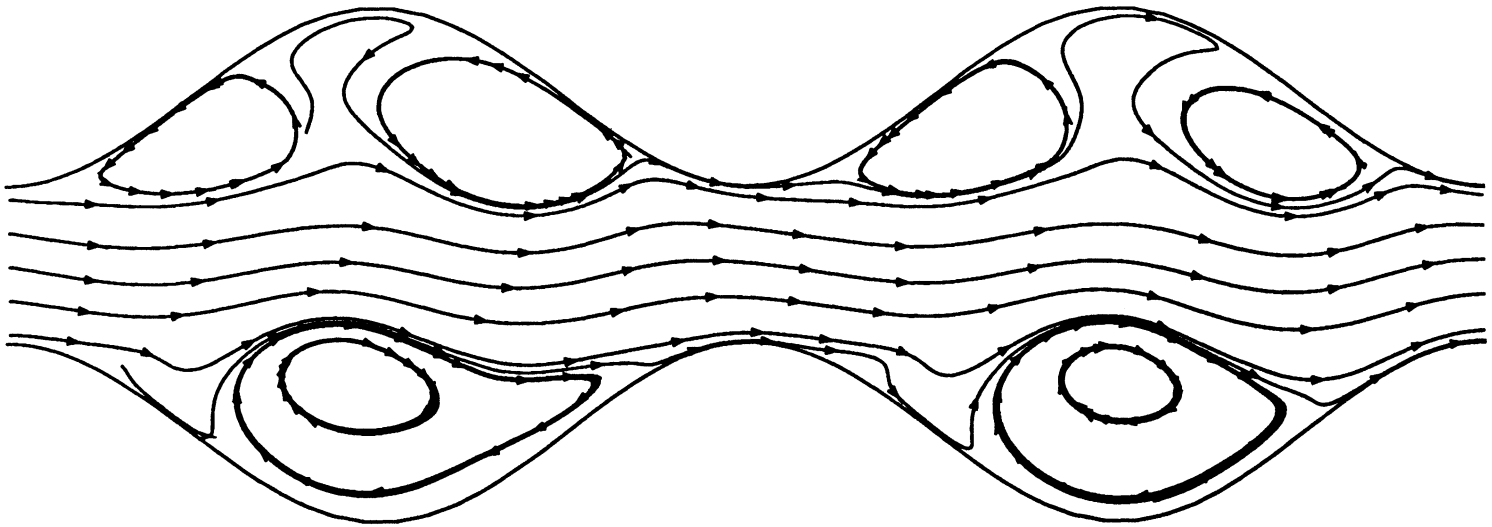

Figure 4.2.5 Instantaneous streamline plot in 13^{th} and 14^{th} waves of Channel #1 at Re = 500 (unsteady flow)

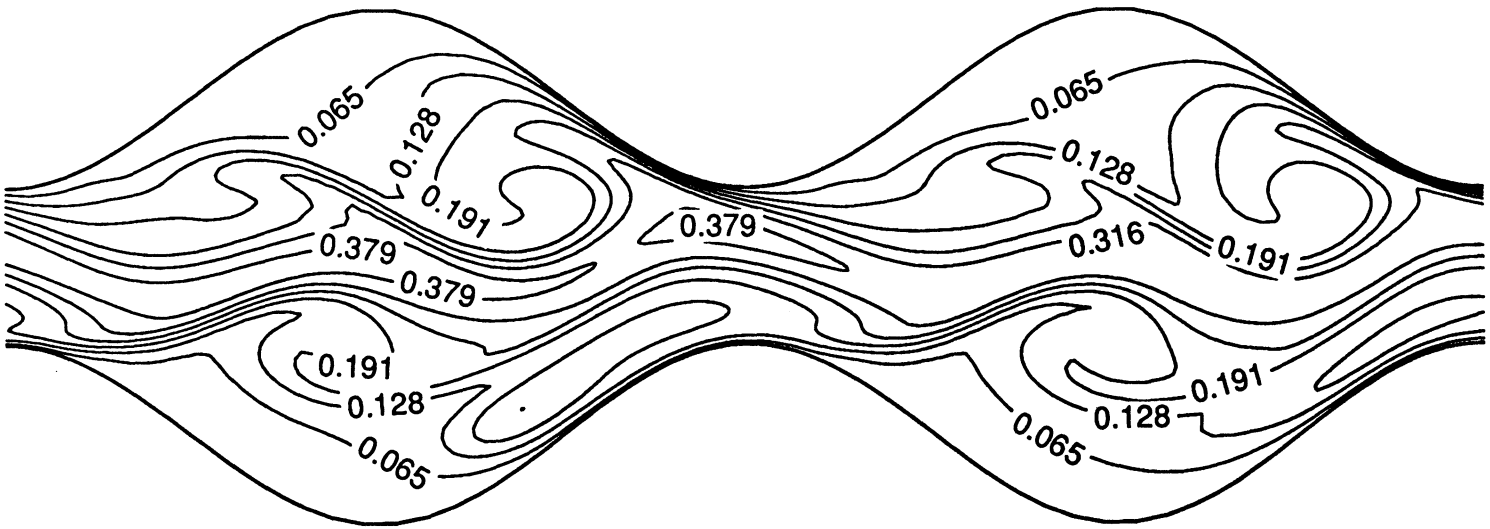

Figure 4.2.6 Instantaneous isotherm plot in 13th and 14th waves of Channel #1 at Re = 500 (unsteady flow)

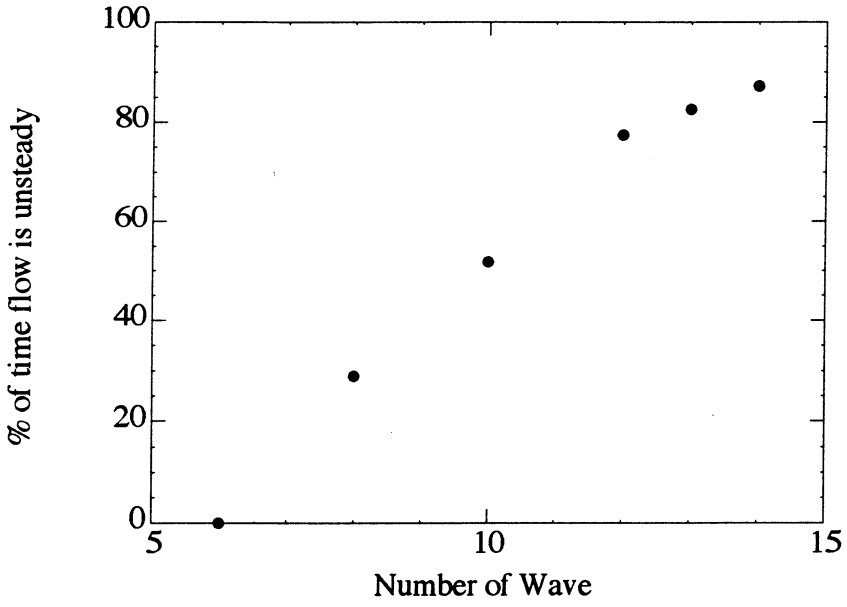

Figure 4.2.7 Percentage of time flow is unsteady as a function of location at Re = 500

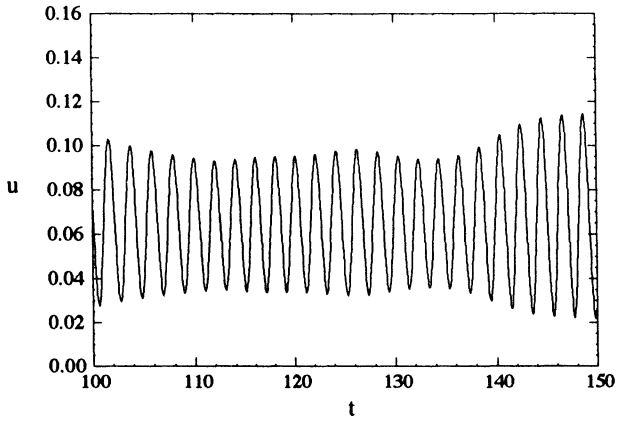

(a)

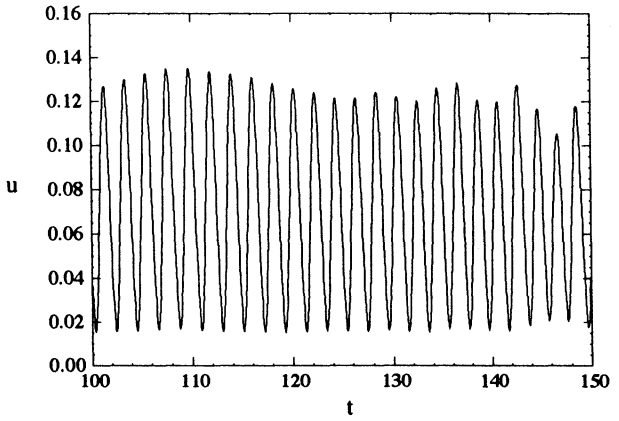

(b)

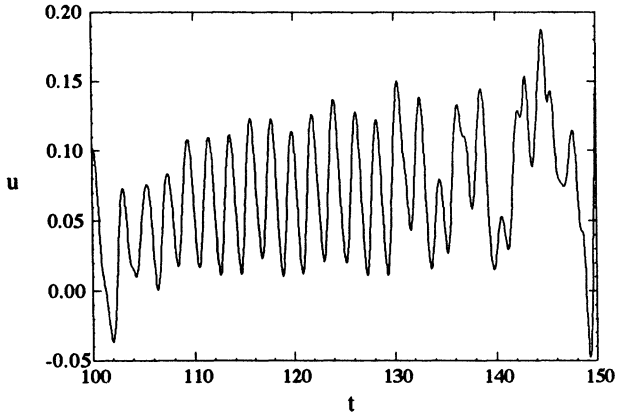

(c)

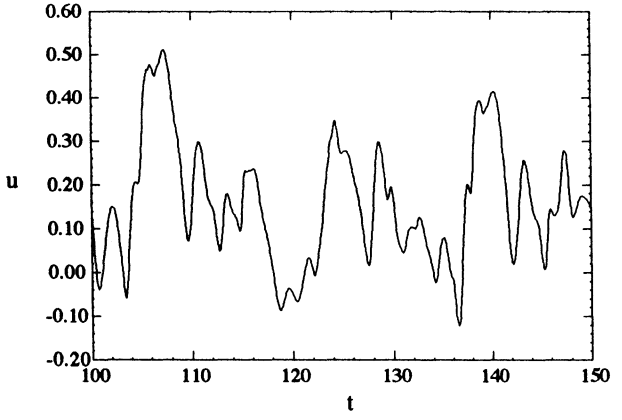

(d)

Figure 4.2.8 Time signals for u-velocity in Channel #1 at Re = 600
(a) Wave 8 (b) Wave 10 (c) Wave 12 (d) Wave 14

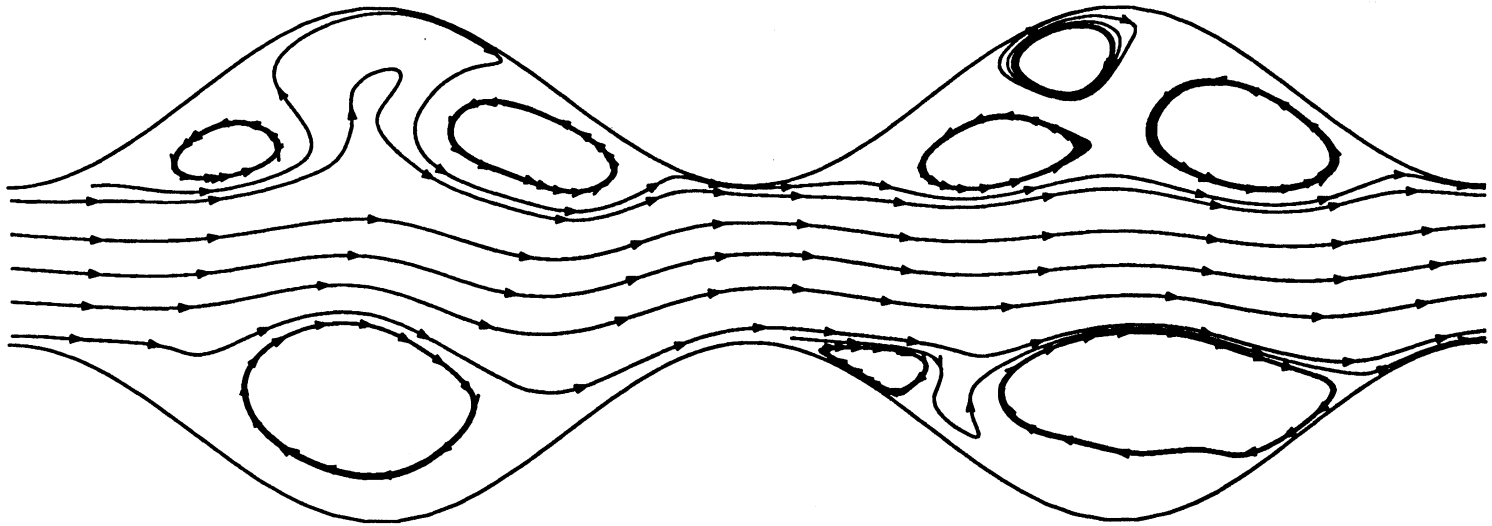

Figure 4.2.9 Instantaneous streamline plot in 13th and 14th waves of Channel #1 at Re = 600

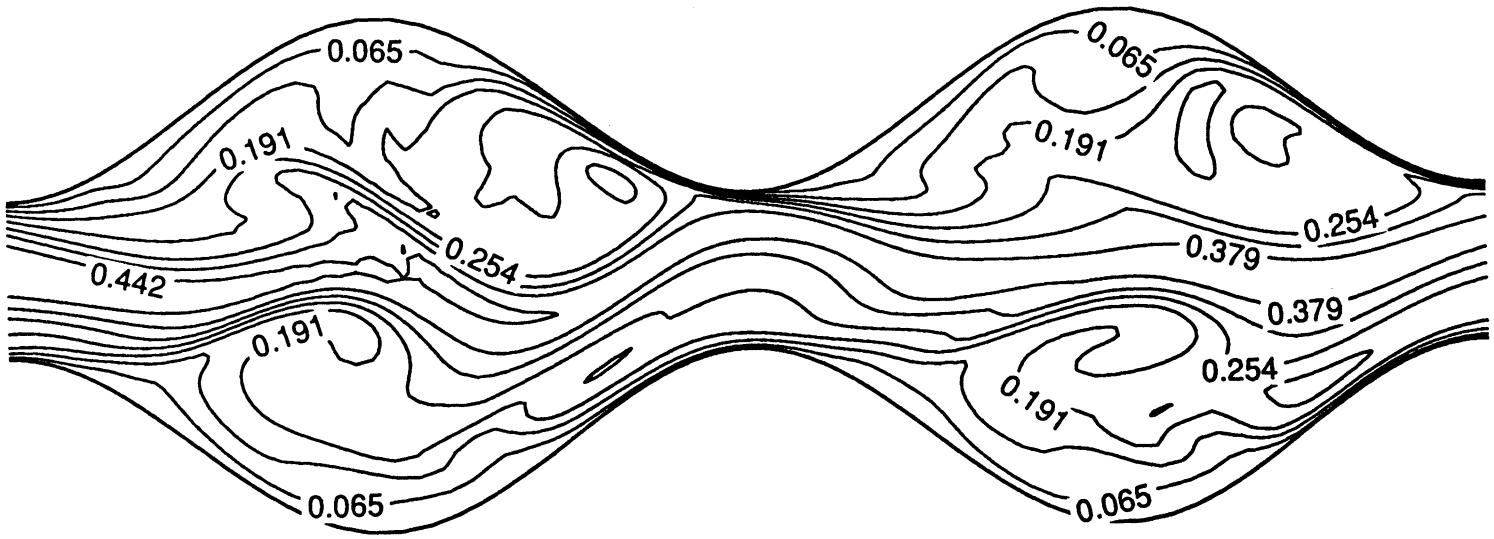

Figure 4.2.10 Instantaneous isotherm plot in 13th and 14th waves of Channel #1 at Re = 600

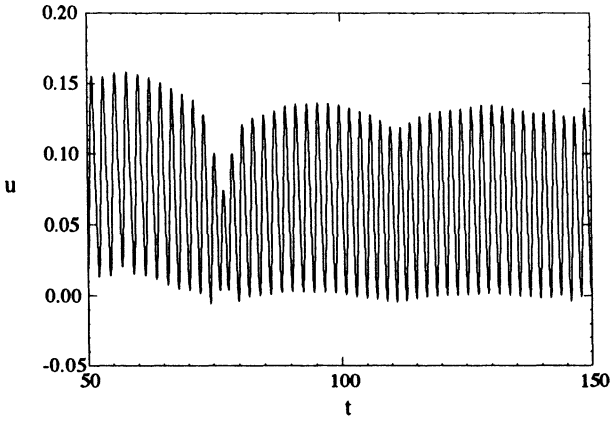

(a)

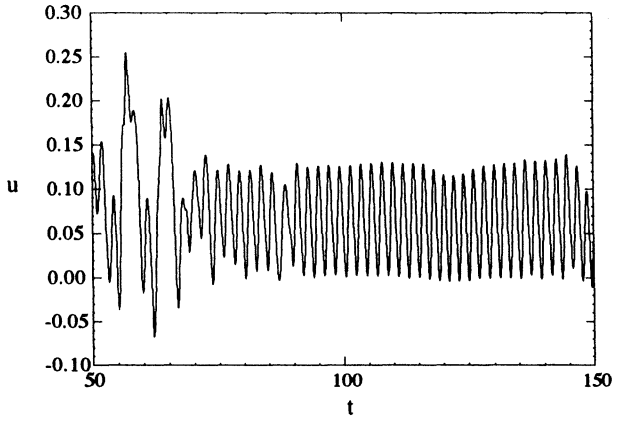

(b)

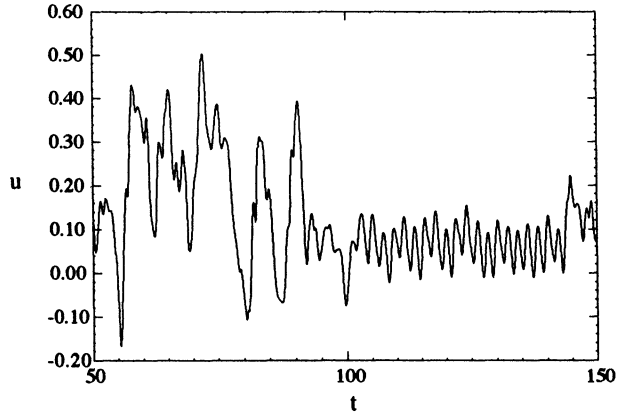

(c)

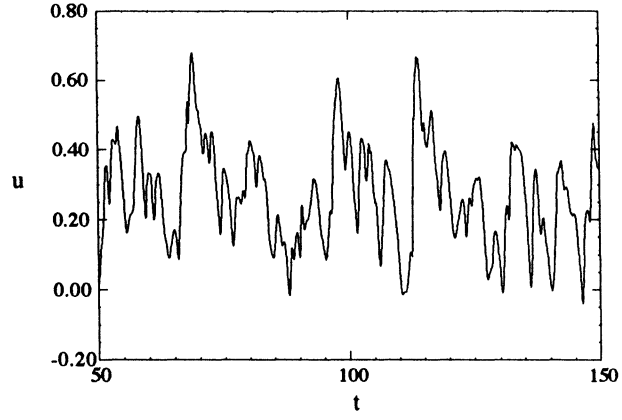

(d)

Figure 4.2.11 Time signals for u-velocity in Channel #1 at Re = 700
(a) Wave 8 (b) Wave 10 (c) Wave 12 (d) Wave 14

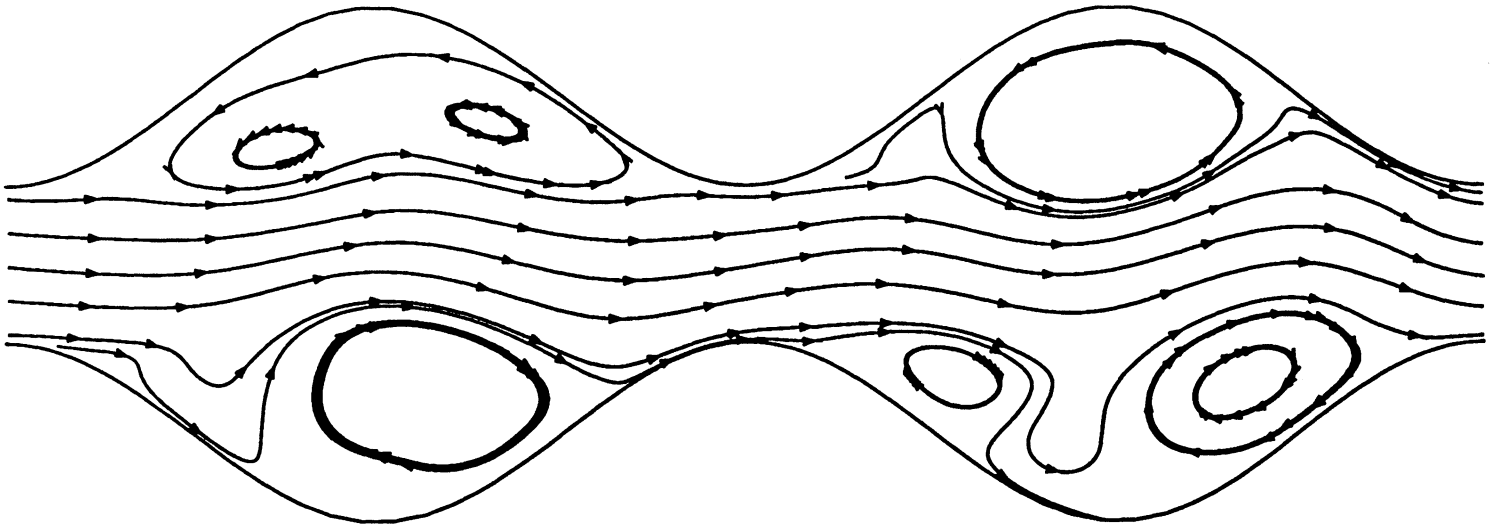

Figure 4.2.12 Instantaneous streamline plot in 13^{th} and 14^{th} waves of Channel #1 at Re = 700

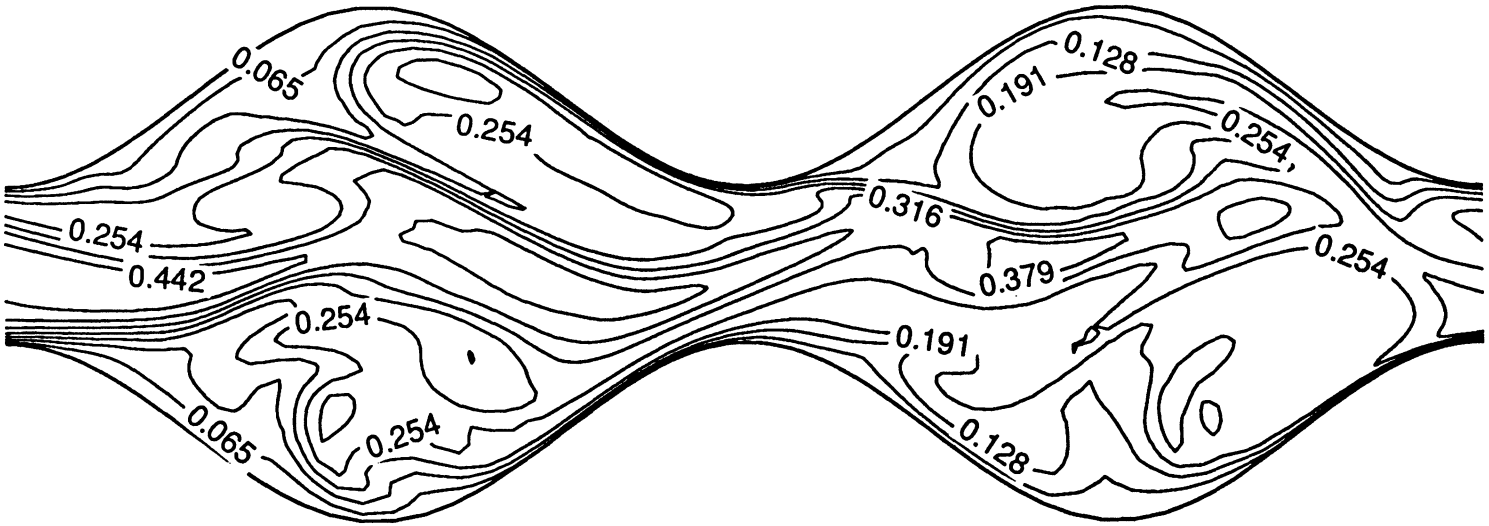

Figure 4.2.13 Instantaneous isotherm plot in 13th and 14th waves of Channel #1 at Re = 700

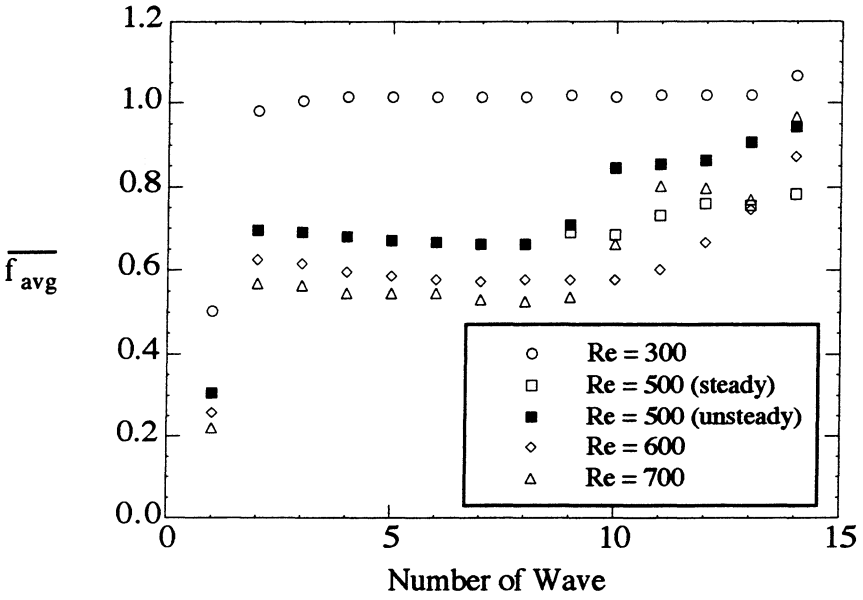

Figure 4.2.14 Time-averaged friction factor averaged across each wavelength as a function of location for Channel #1

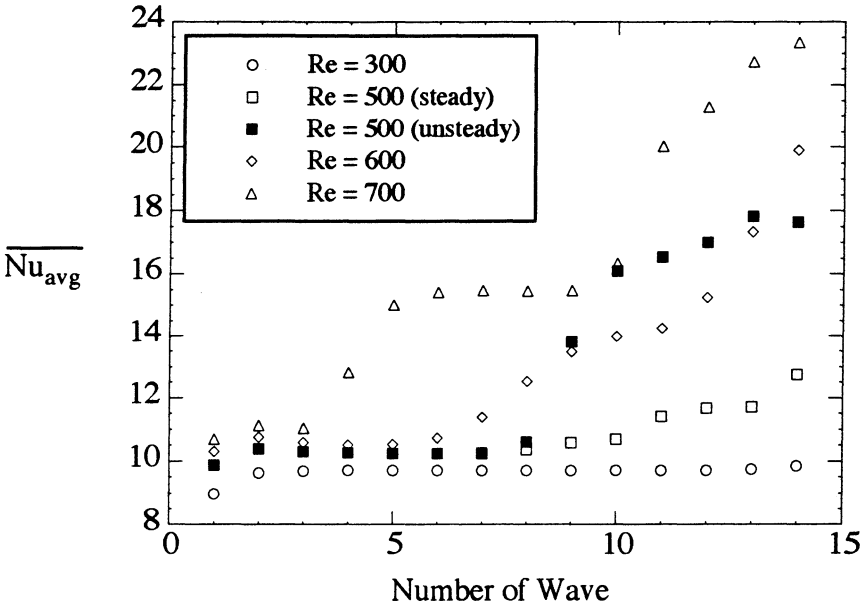

Figure 4.2.15 Time-averaged Nusselt number averaged across each wavelength as a function of location for Channel #1

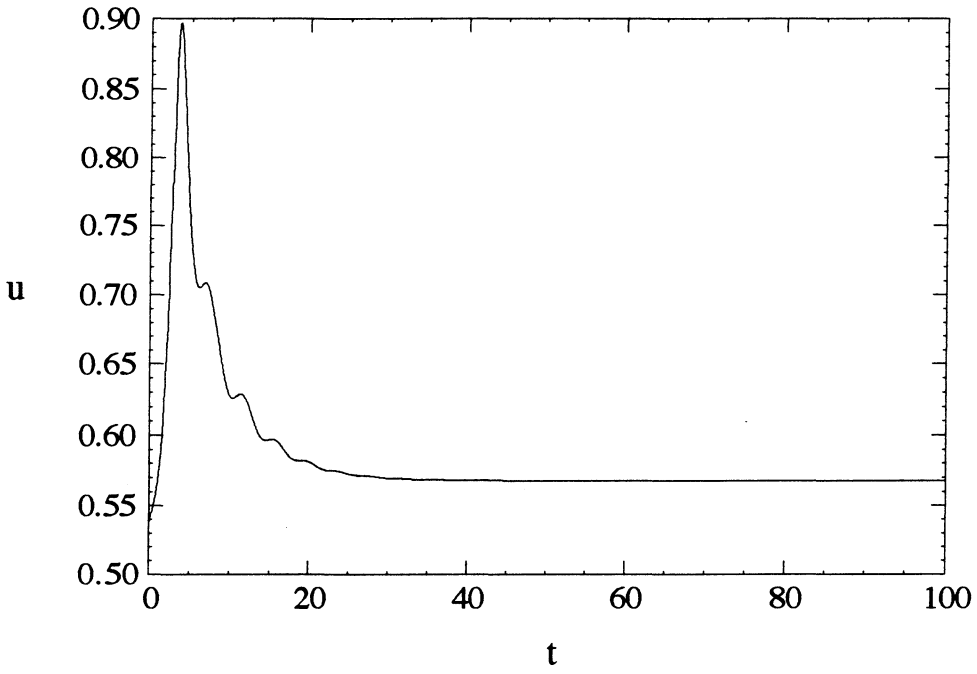

Figure 4.3.1 Time signal for u-velocity in 14th wave of Channel #2 at Re = 300

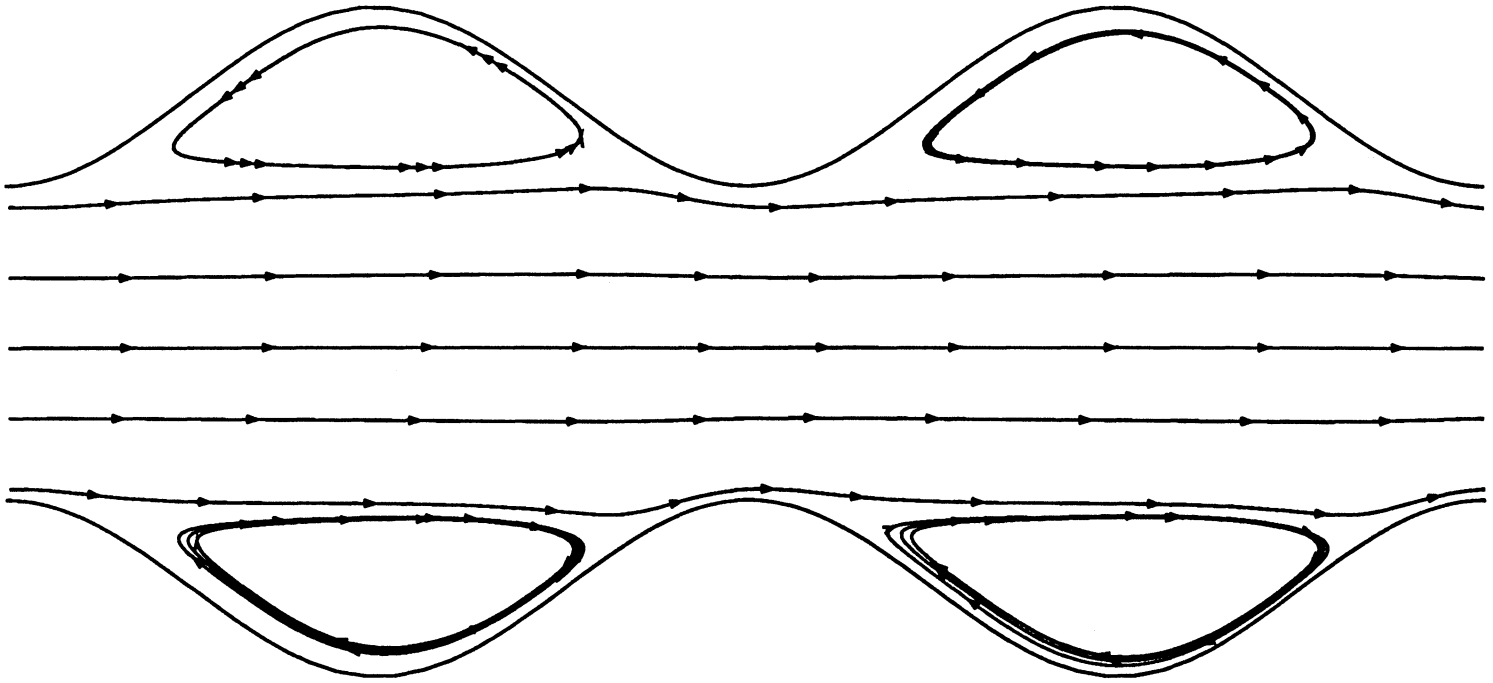

Figure 4.3.2 Instantaneous streamline plot in 13th and 14th waves of Channel #2 at Re = 300

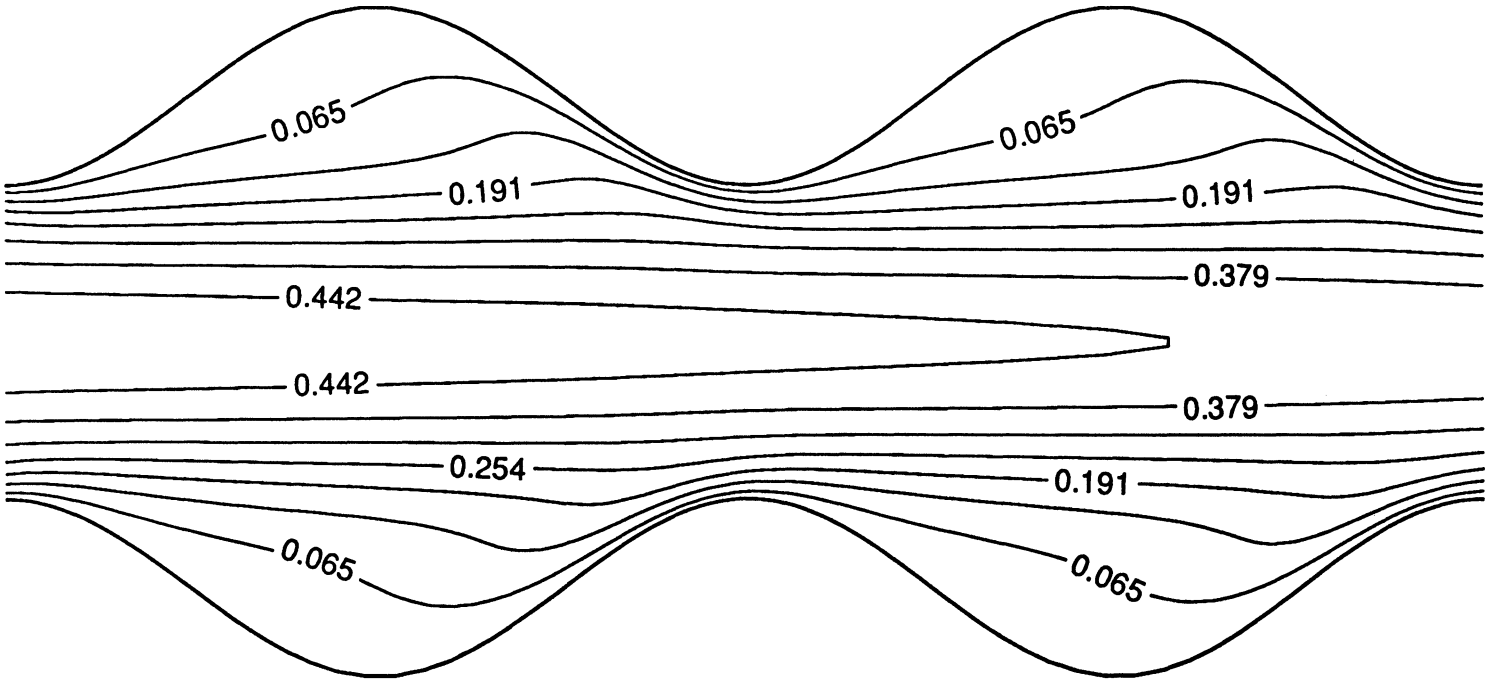

Figure 4.3.3 Instantaneous isotherm plot in 13th and 14th waves of Channel #2 at Re = 300

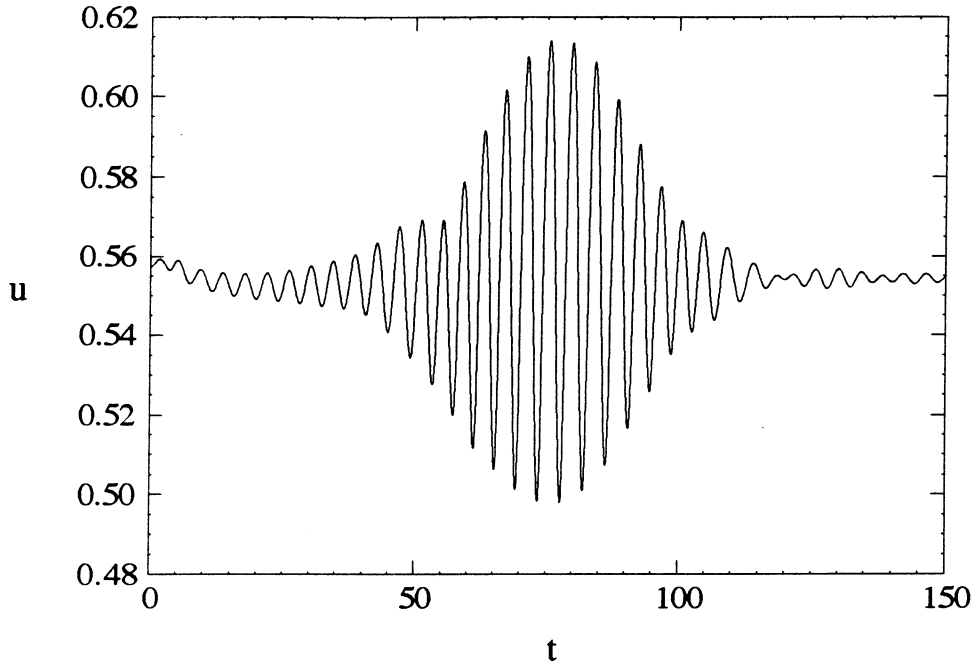

Figure 4.3.4 Time signal for u-velocity in 14th wave of Channel #2 at Re = 700

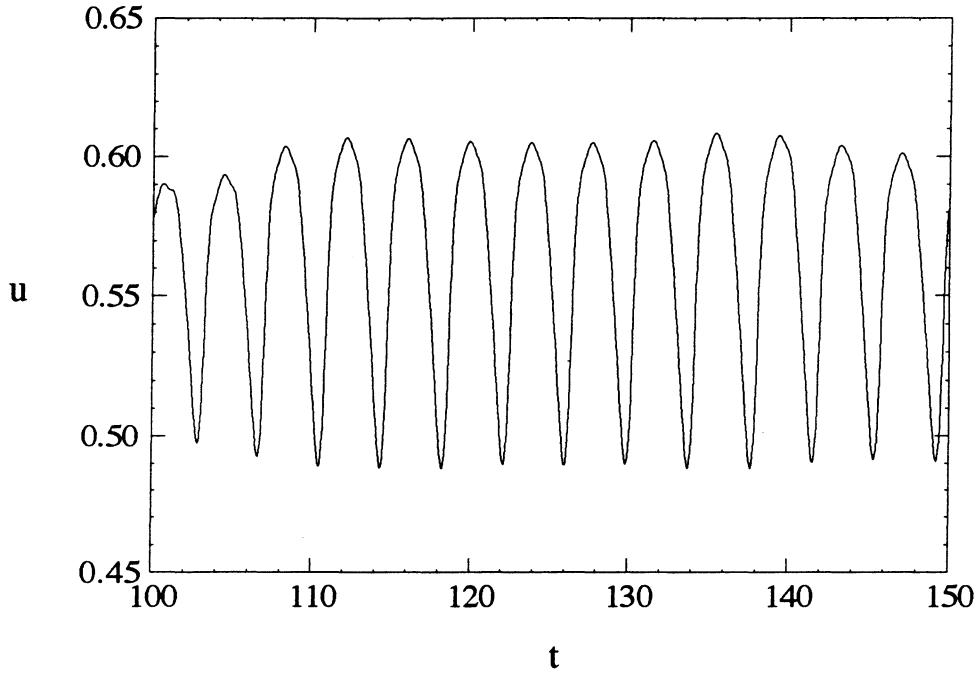

Figure 4.3.5 Time signal for u-velocity in 14th wave of Channel #2 at Re = 1000

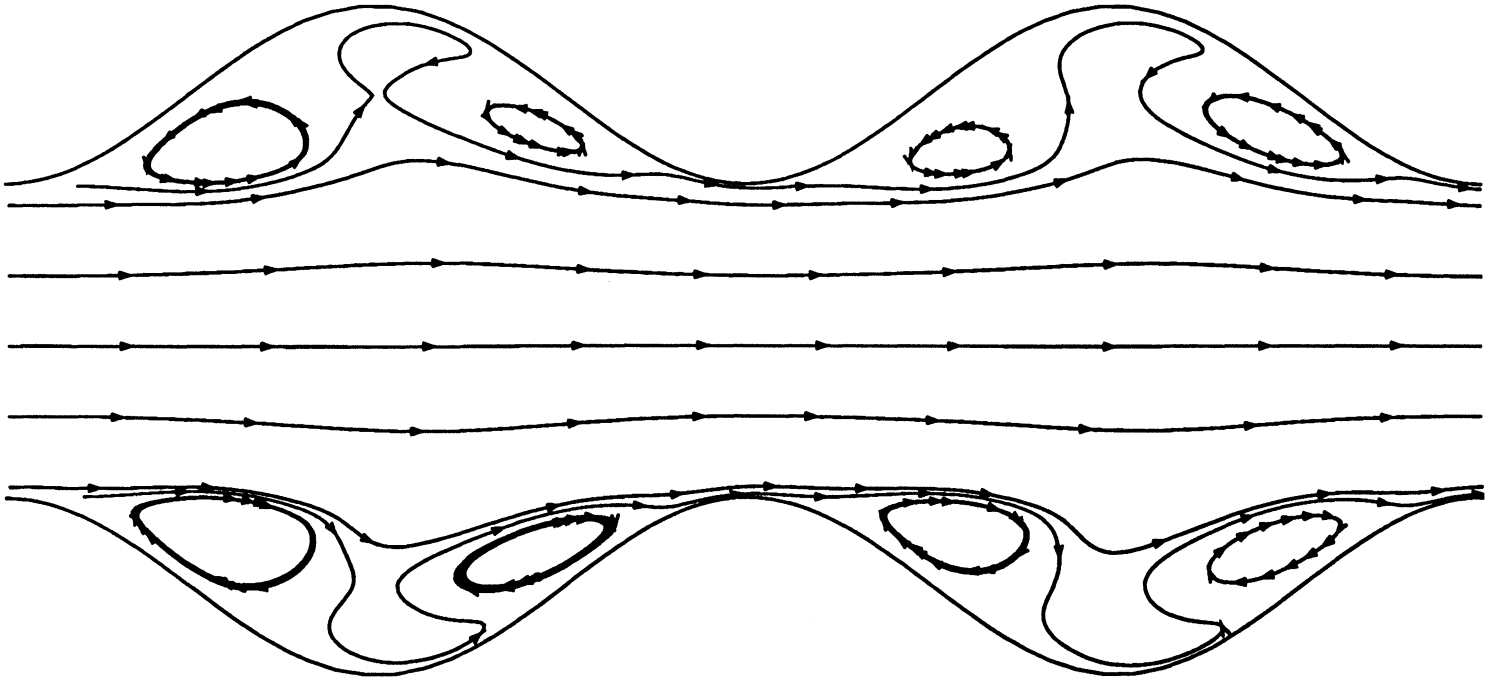

Figure 4.3.6 Instantaneous streamline plot in 13th and 14th waves of Channel #2 at Re = 1000

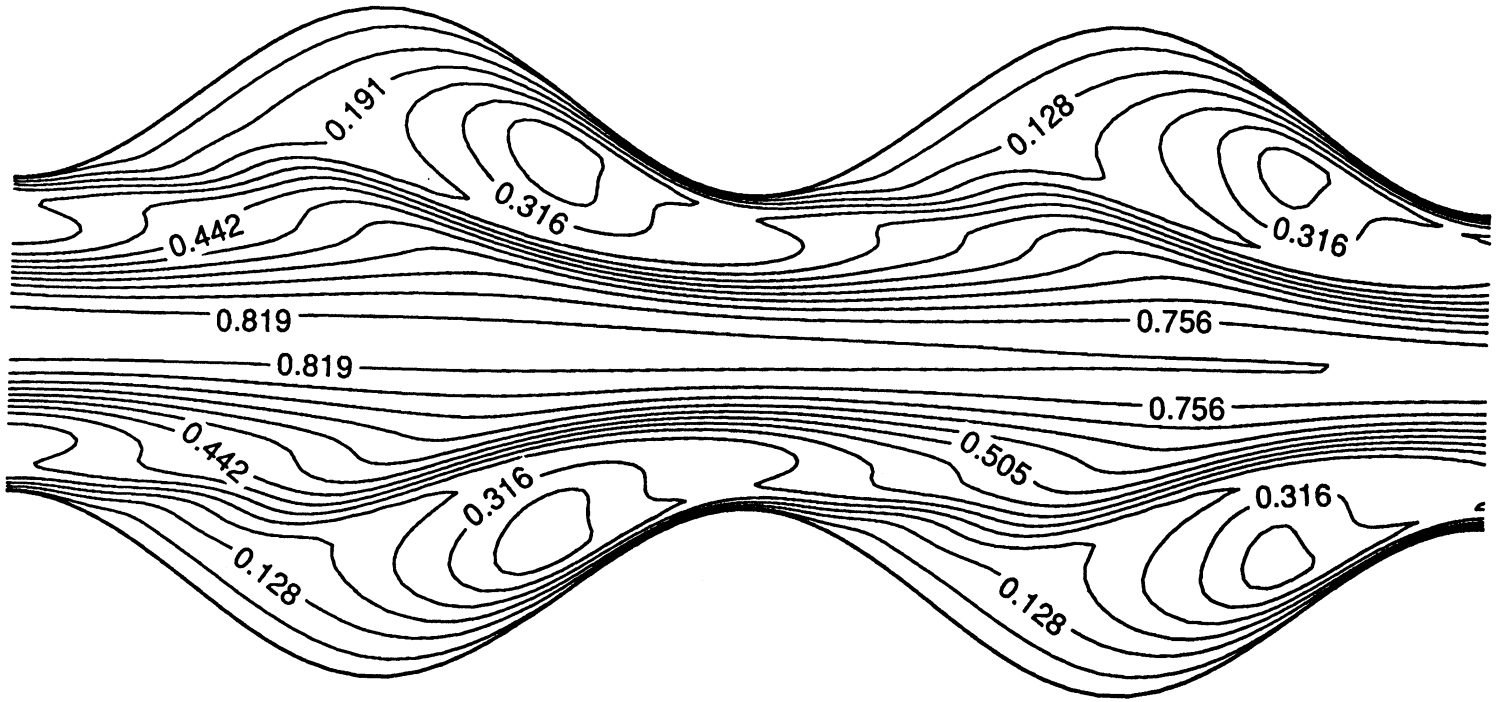

Figure 4.3.7 Instantaneous isotherm plot in 13th and 14th waves of Channel #2 at Re = 1000

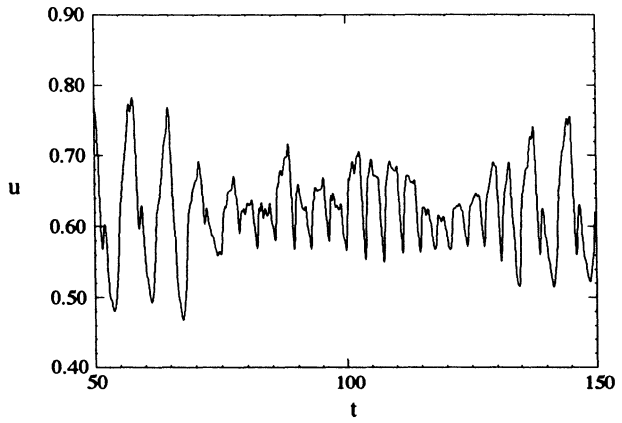

(a)

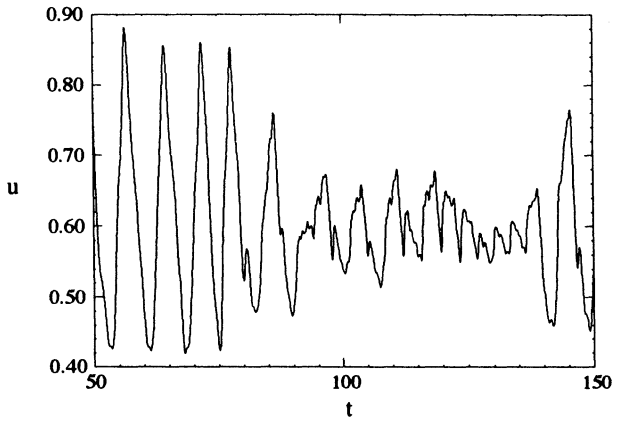

(b)

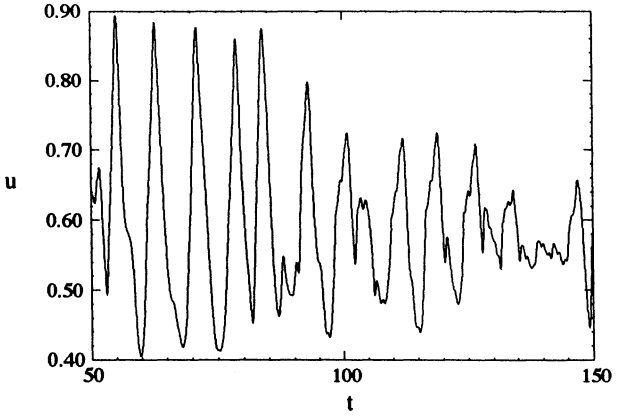

(c)

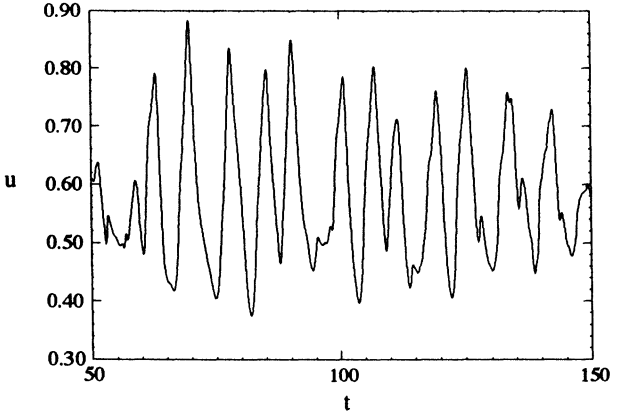

(d)

Figure 4.3.8 Time signals for u-velocity in Channel #2 at Re = 1400
(a) Wave 8 (b) Wave 10 (c) Wave 12 (d) Wave 14

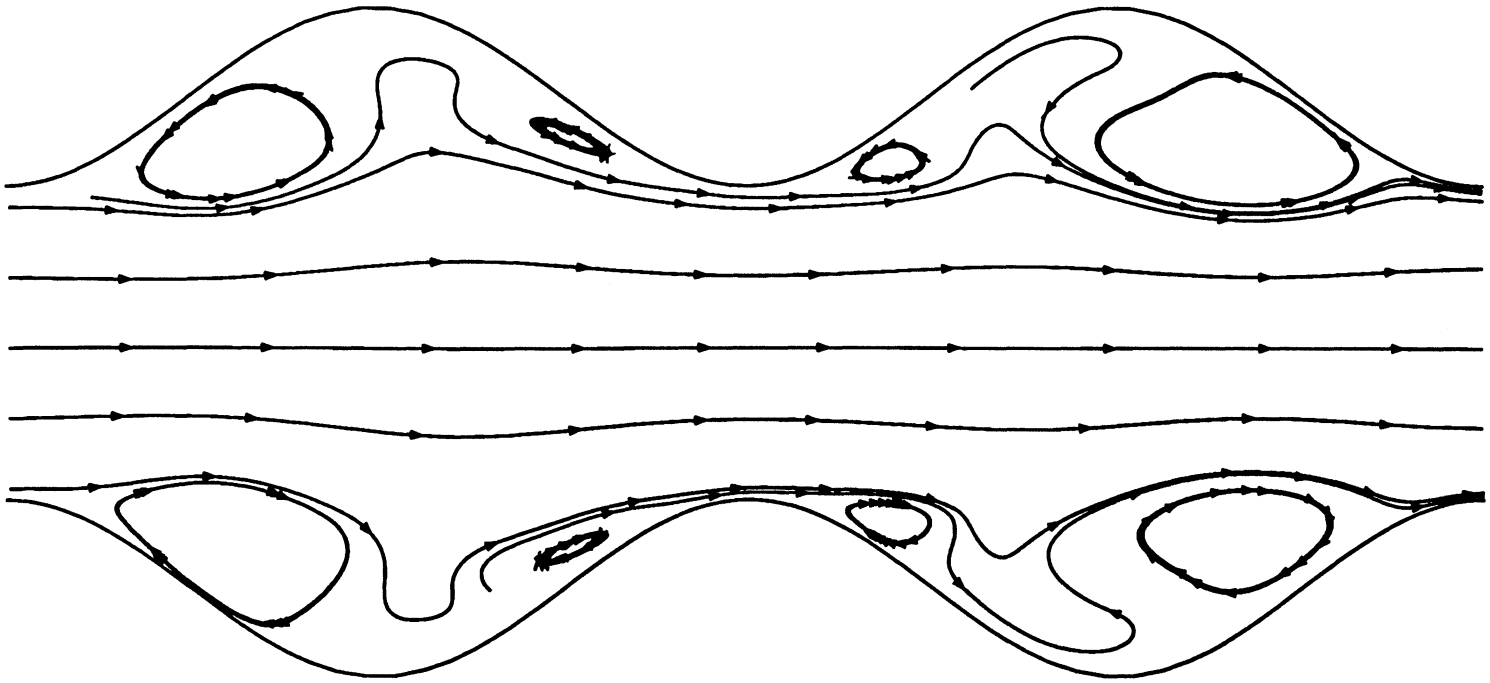

Figure 4.3.9 Instantaneous streamline plot in 13th and 14th waves of Channel #2 at Re = 1400

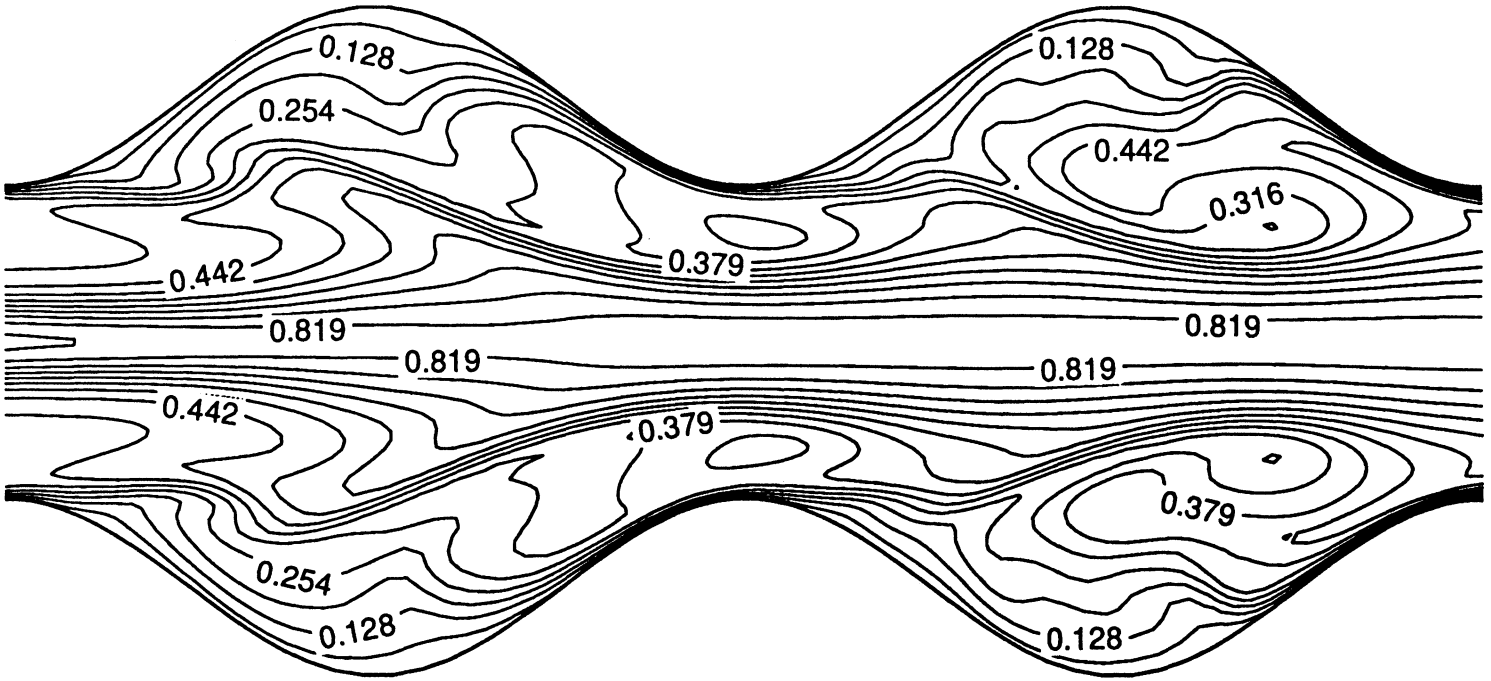

Figure 4.3.10 Instantaneous isotherm plot in 13th and 14th waves of Channel #2 at Re = 1400

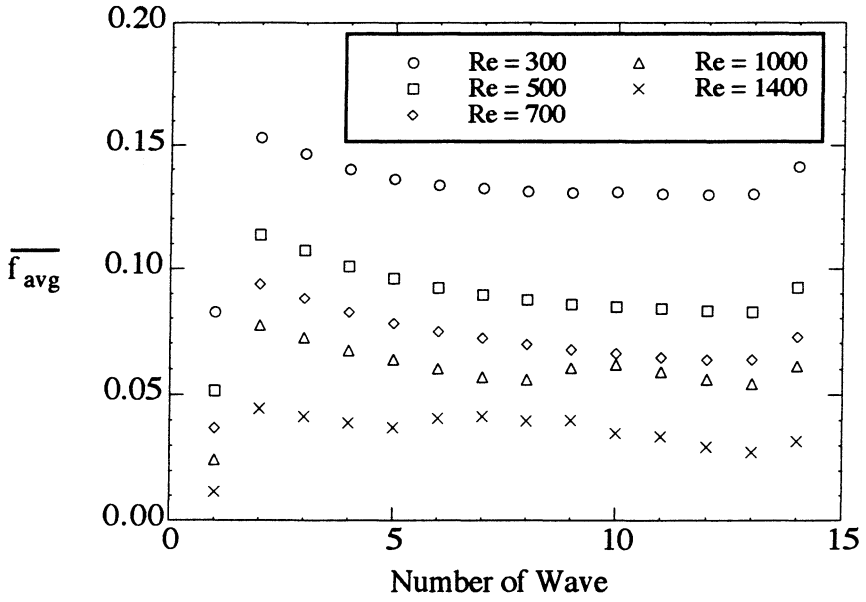

Figure 4.3.11 Time-averaged friction factor averaged across each wavelength as a function of location for Channel #2

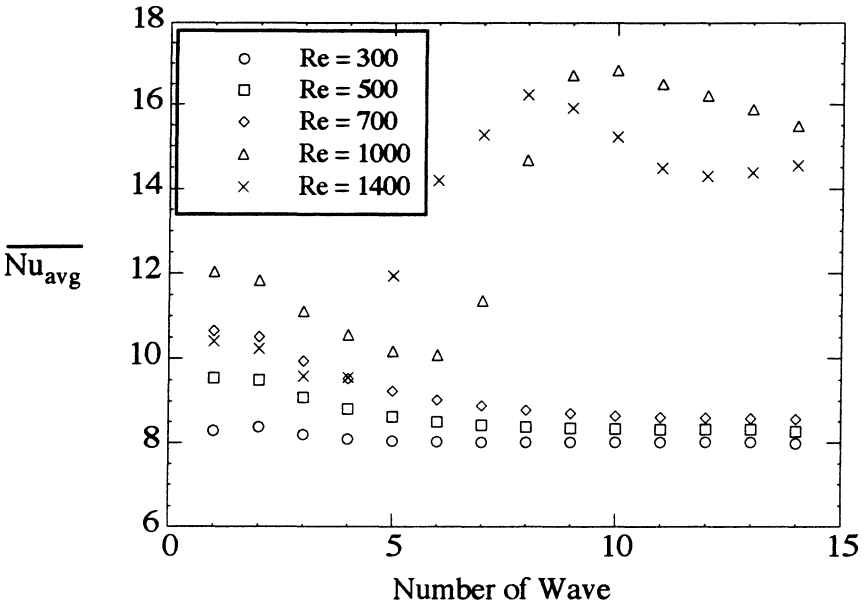

Figure 4.3.12 Time-averaged Nusselt number averaged across each wavelength as a function of location for Channel #2

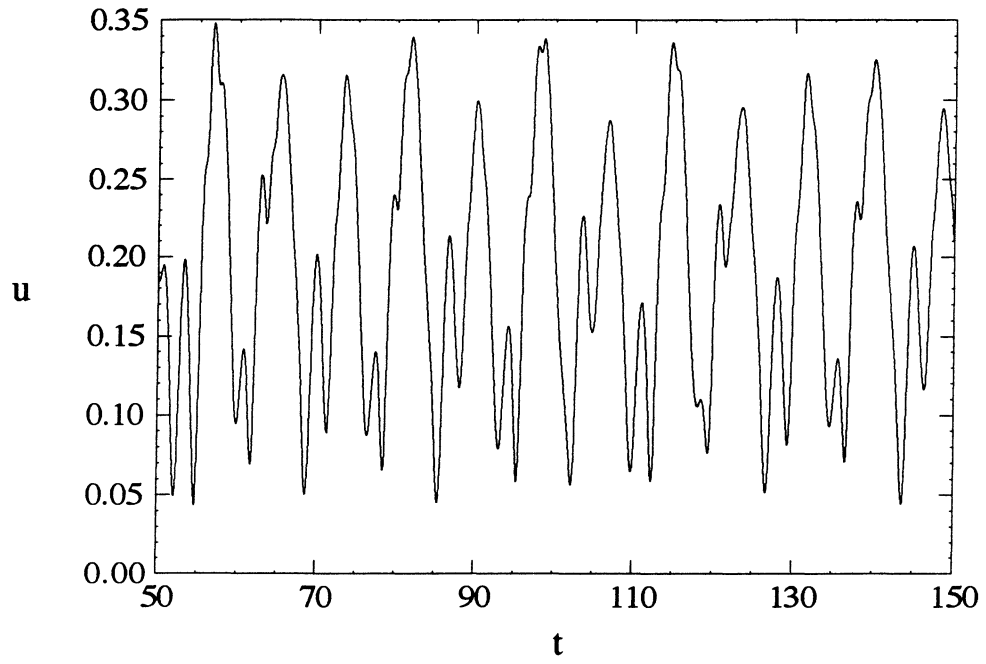

Figure 5.2.1 Time signal for u-velocity in channel with base geometry at Re = 268

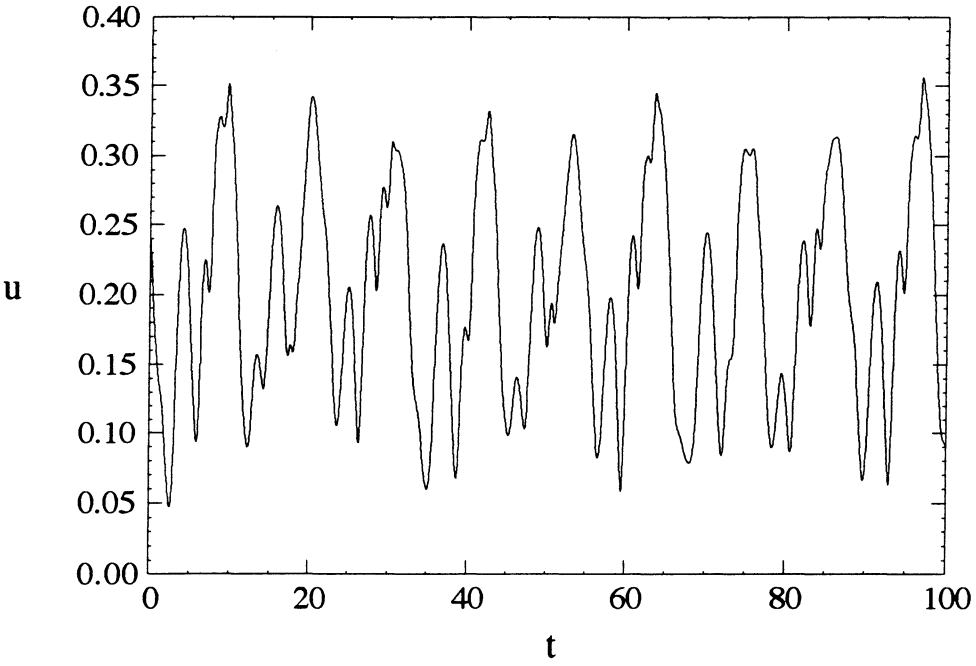

Figure 5.2.2 Time signal for u-velocity in channel with base geometry at Re = 425

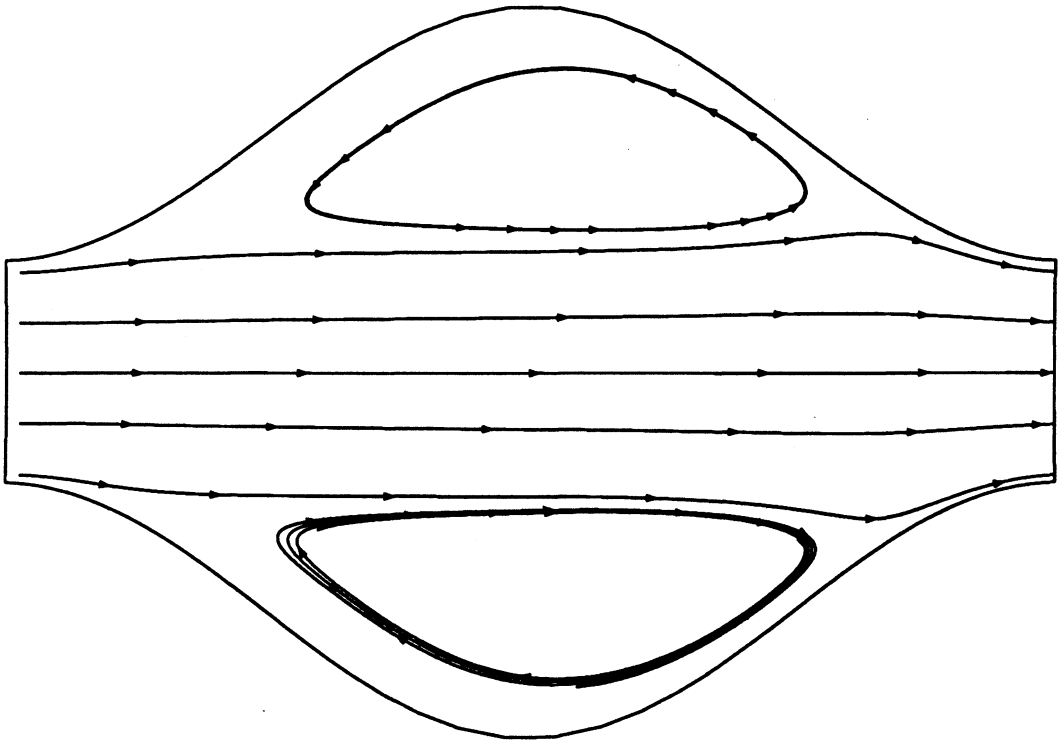

Figure 5.2.3 Instantaneous streamline plot for steady flow in channel with base geometry at Re = 169

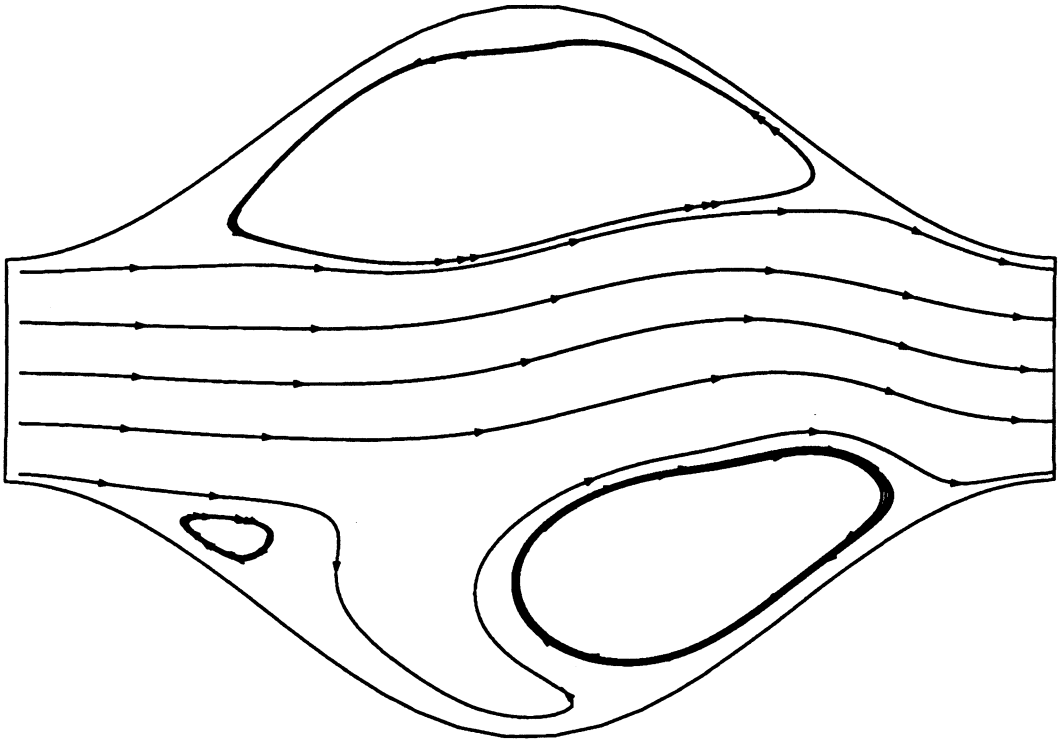

Figure 5.2.4 Instantaneous streamline plot for unsteady flow in channel with base geometry at Re = 364

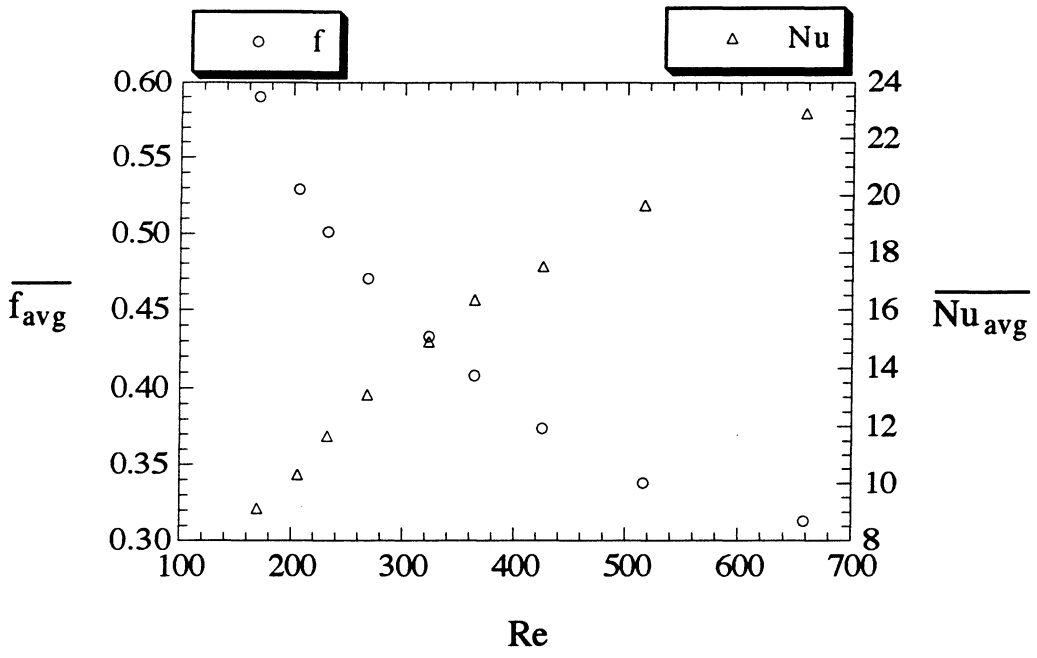

Figure 5.2.5 Time averaged friction factor and Nusselt number averaged across one wavelength as a function of Reynolds number for the base geometry

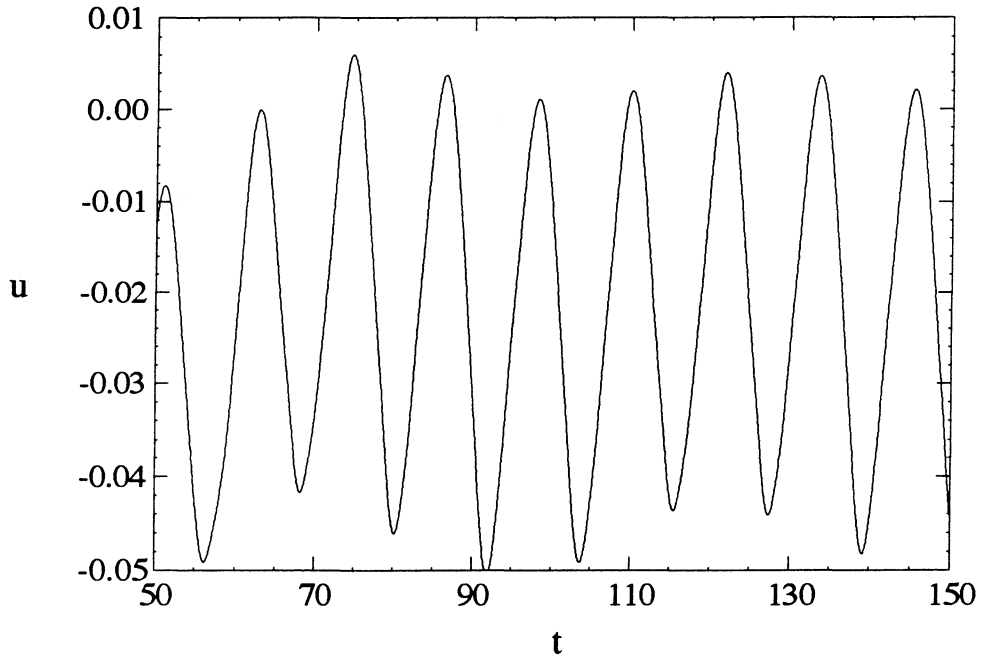

Figure 5.3.1 Time signal for u-velocity in channel with H_{avg} = 1.0 at Re = 182

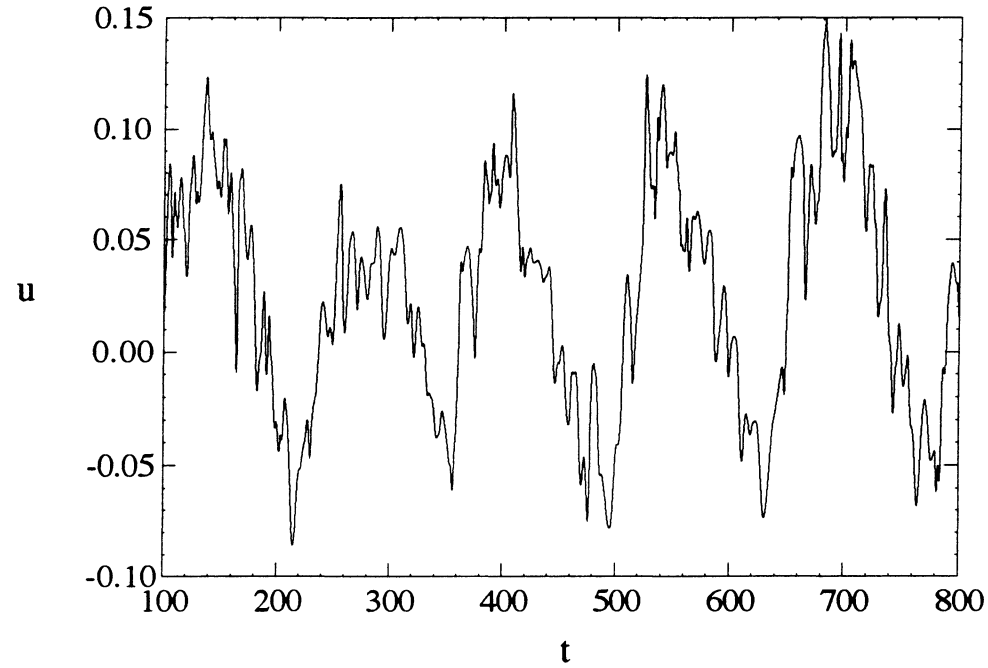

Figure 5.3.2 Time signal for u-velocity in channel with H_{avg} = 1.0 at Re = 400

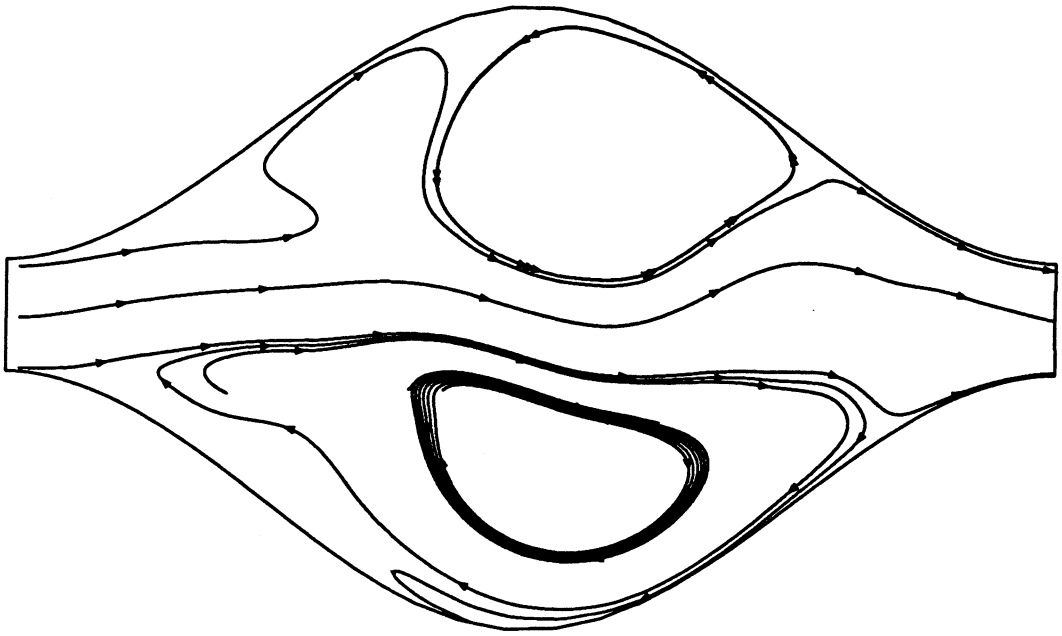

Figure 5.3.3 Instantaneous streamline plot for channel with $H_{avg} = 1.0$ at Re = 400

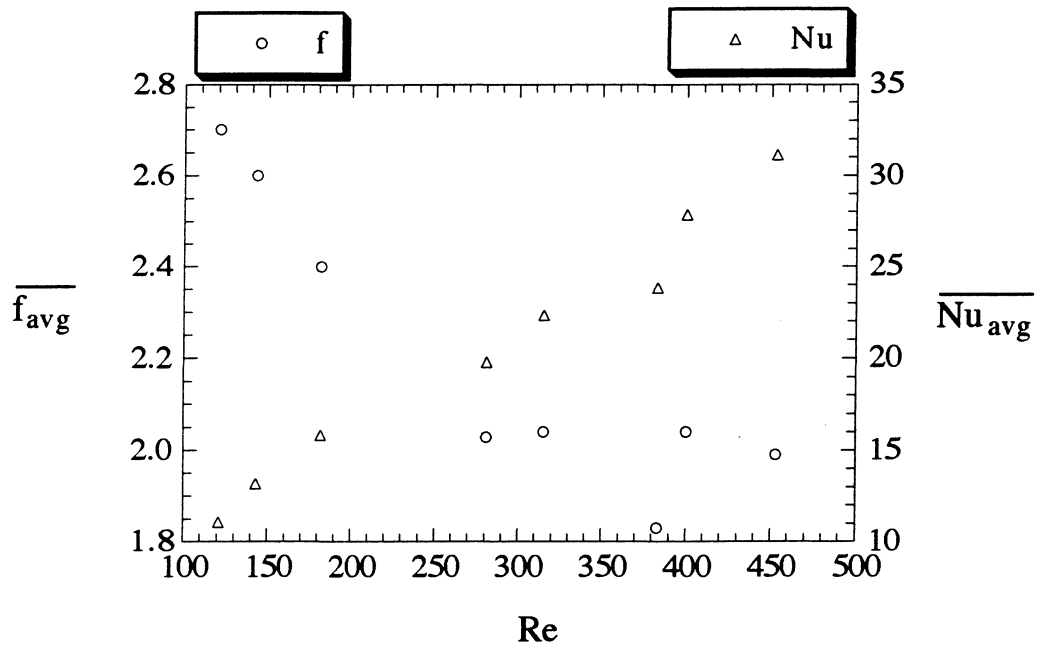

Figure 5.3.4 Time averaged friction factor and Nusselt number averaged across one wavelength as a function of Reynolds number for $H_{avg} = 1.0$

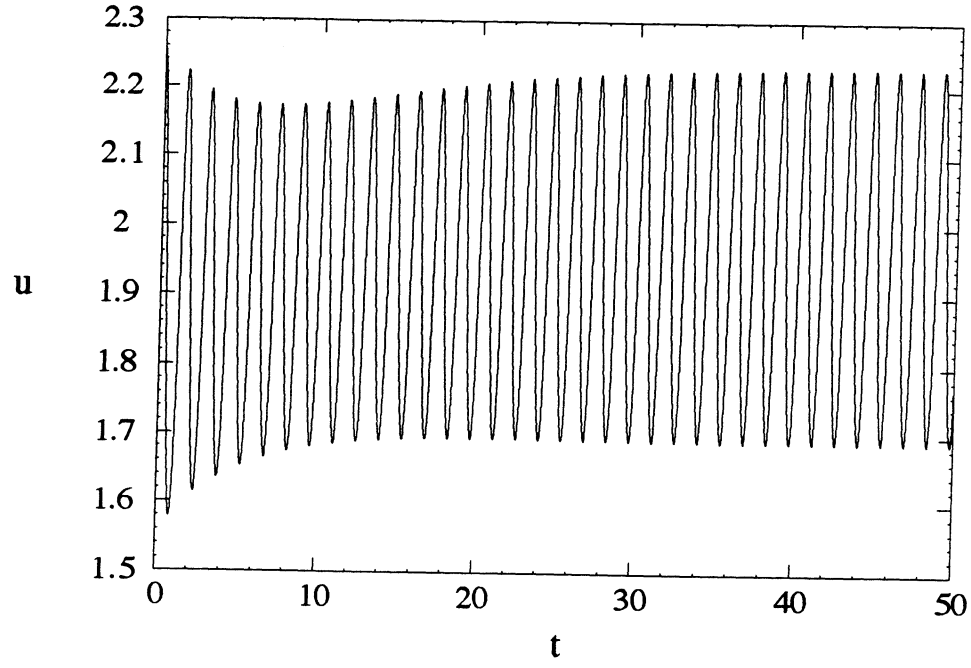

Figure 5.3.5 Time signal for u-velocity in channel with H_{avg} = 1.9 at Re = 269

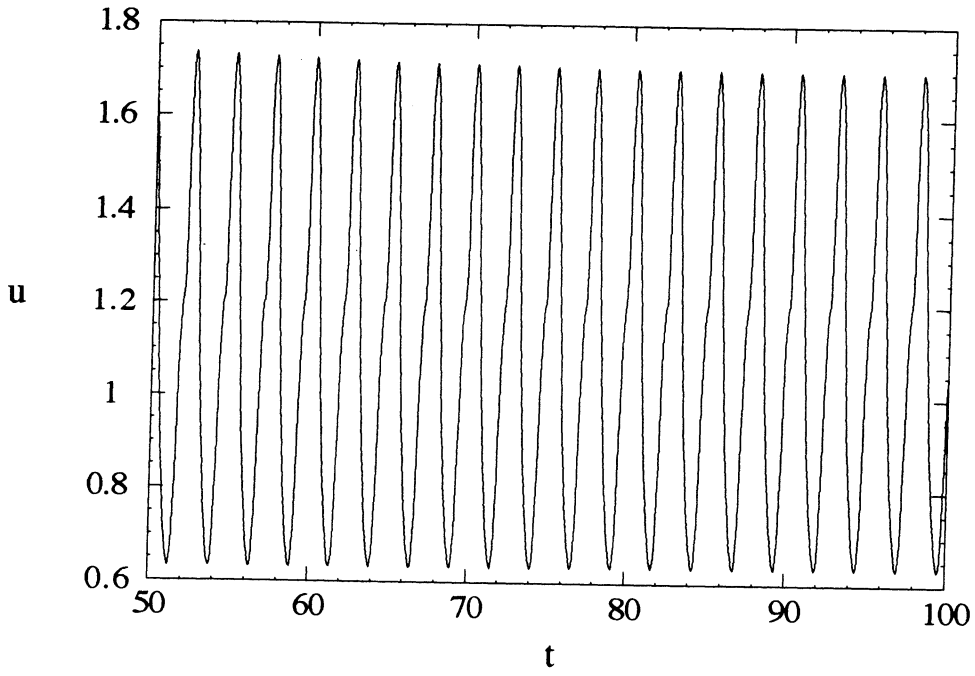

Figure 5.3.6 Time signal for u-velocity in channel with H_{avg} = 1.9 at Re = 1001

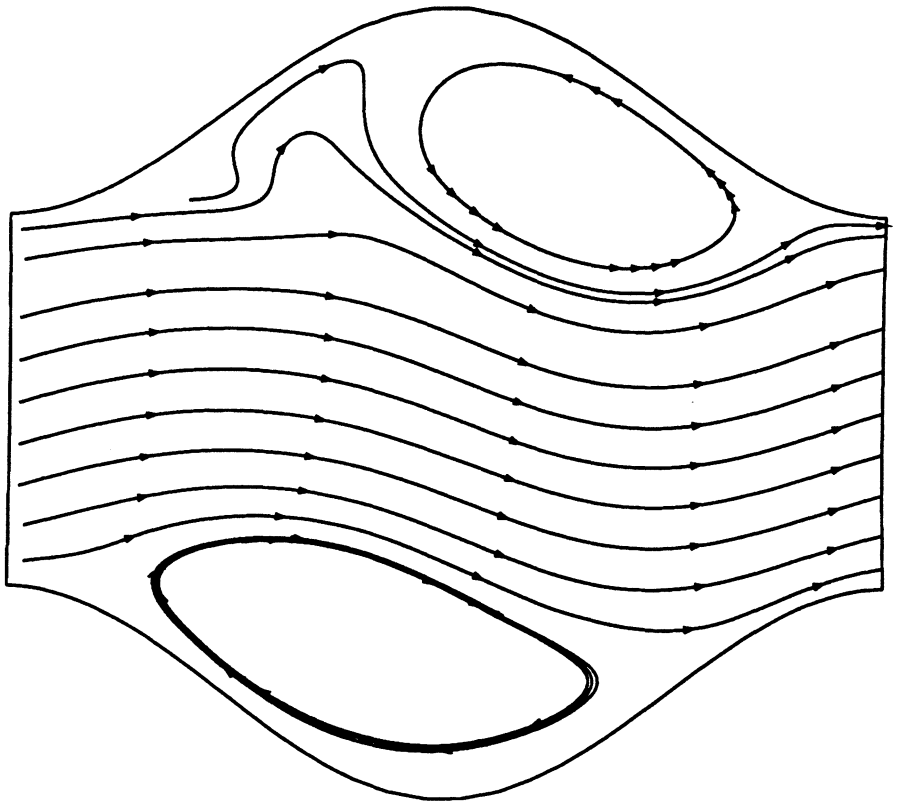

Figure 5.3.7 Instantaneous streamline plot for channel with $H_{avg} = 1.9$ at Re = 1001

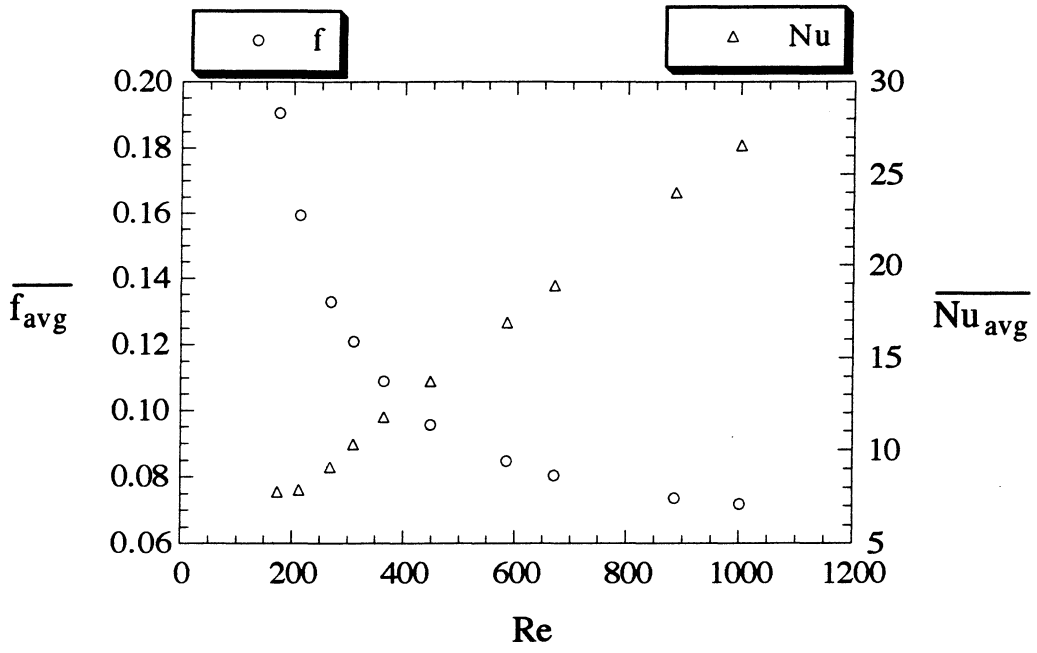

Figure 5.3.8 Time averaged friction factor and Nusselt number averaged across one wavelength as a function of Reynolds number for $H_{avg} = 1.9$

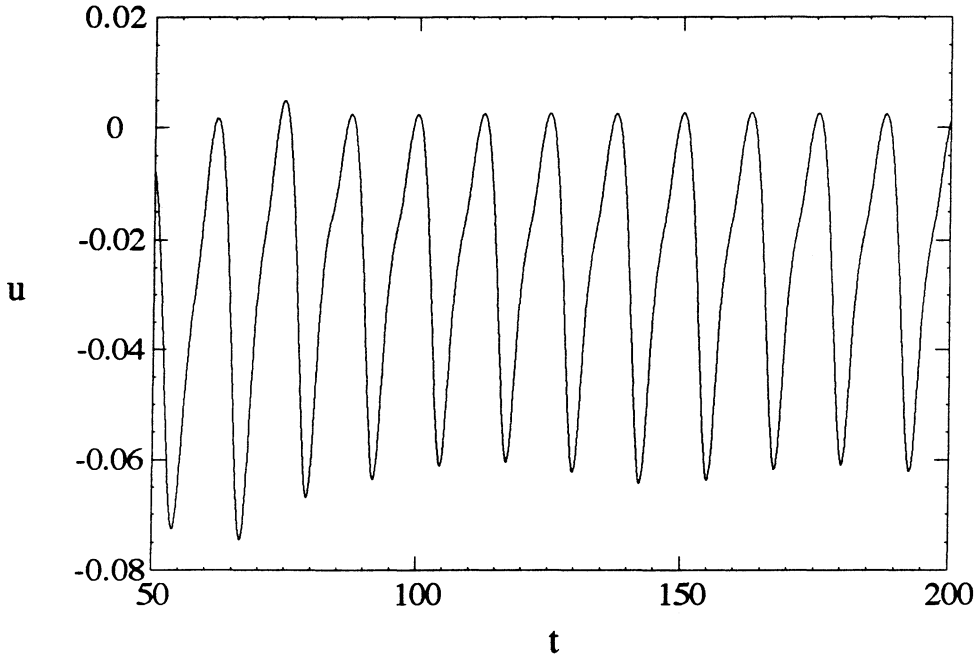

Figure 5.4.1 Time signal for u-velocity in channel with a = 0.50 at Re = 174

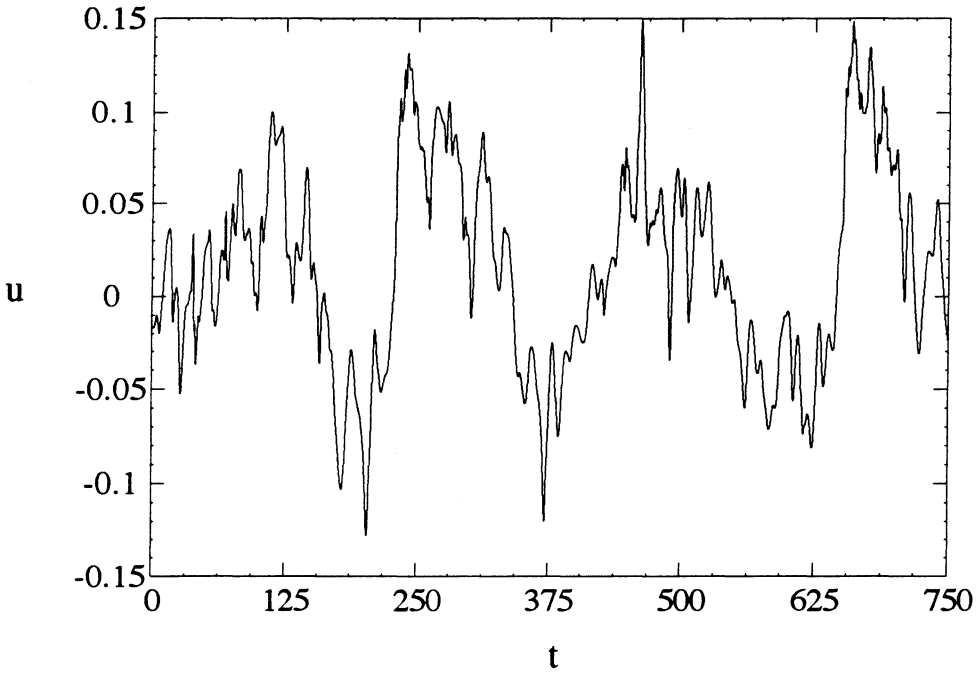

Figure 5.4.2 Time signal for u-velocity in channel with a = 0.50 at Re = 363

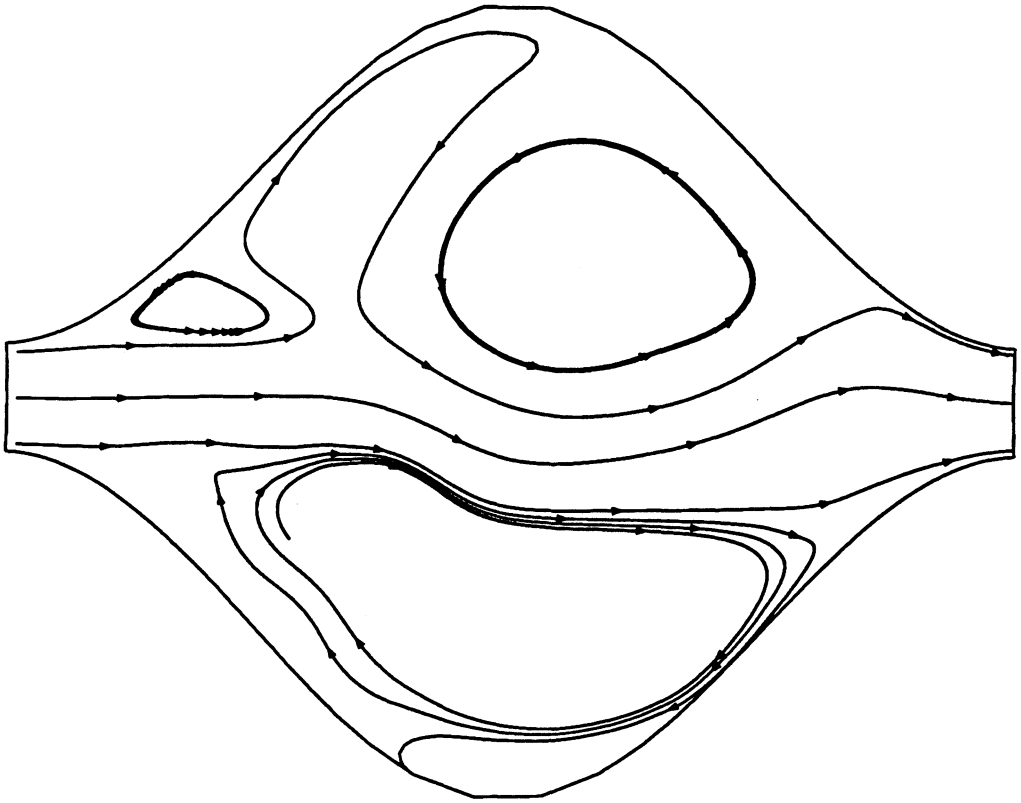

Figure 5.4.3 Instantaneous streamline plot for channel with a = 0.50 at Re = 363

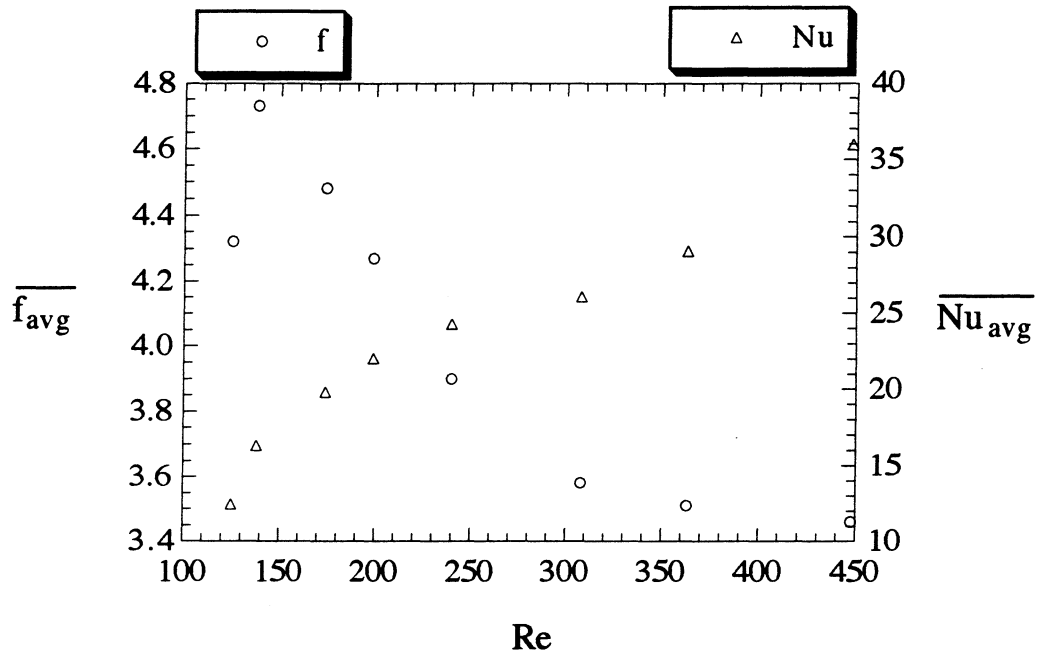

Figure 5.4.4 Time averaged friction factor and Nusselt number averaged across one wavelength as a function of Reynolds number for a = 0.50

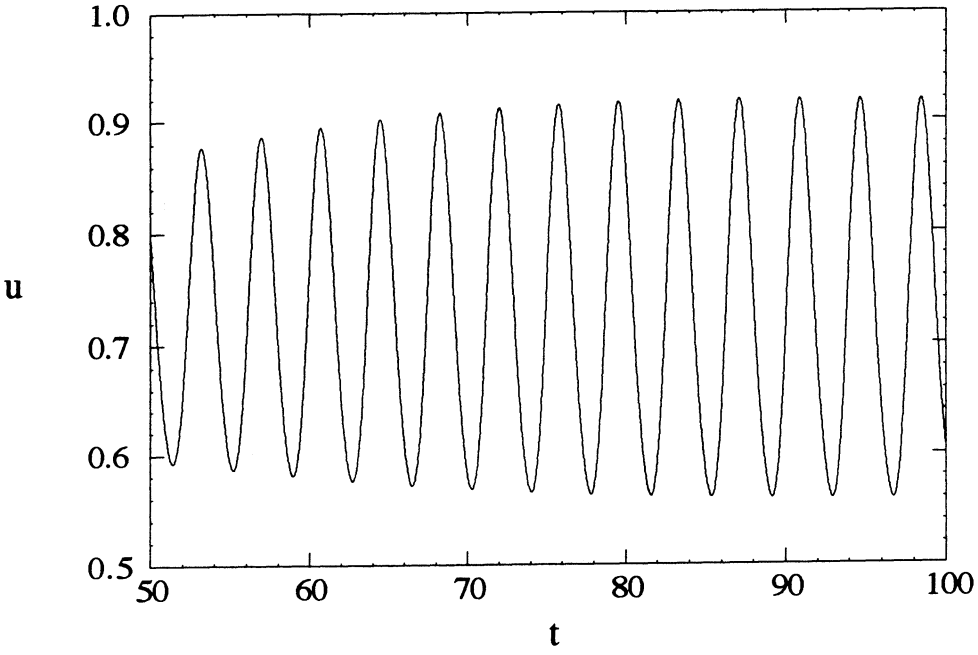

Figure 5.4.5 Time signal for u-velocity in channel with a = 0.25 at Re = 260

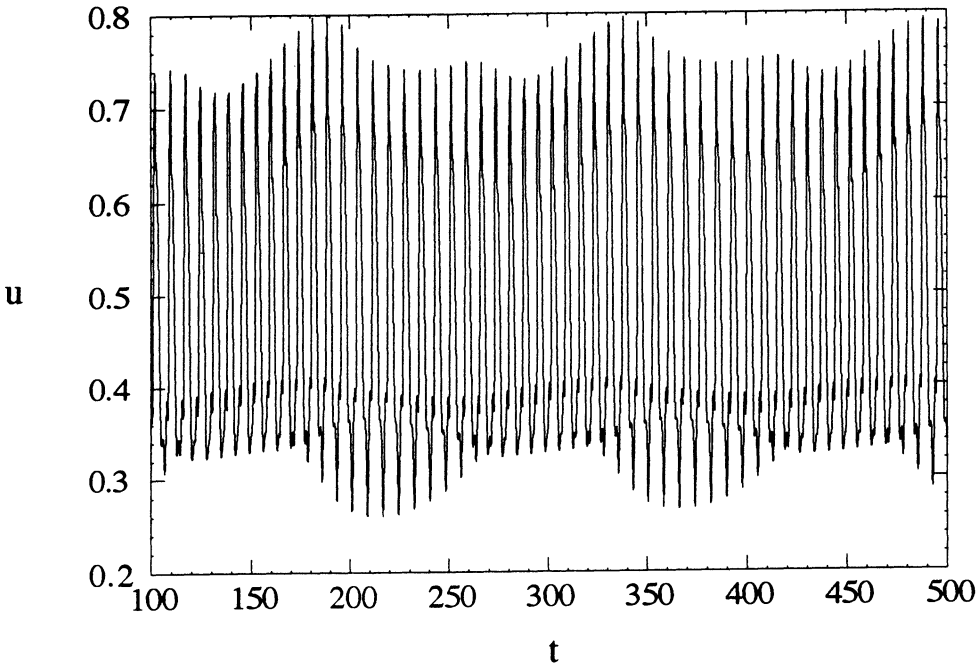

Figure 5.4.6 Time signal for u-velocity in channel with a = 0.25 at Re = 668

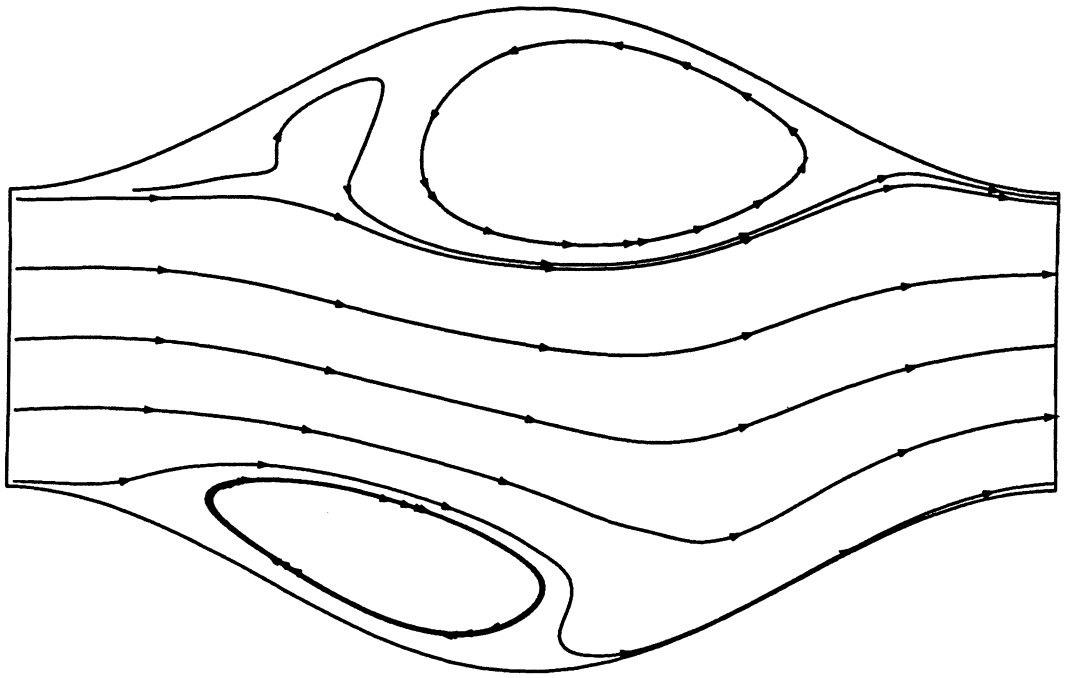

Figure 5.4.7 Instantaneous streamline plot for channel with a = 0.25 at Re = 668

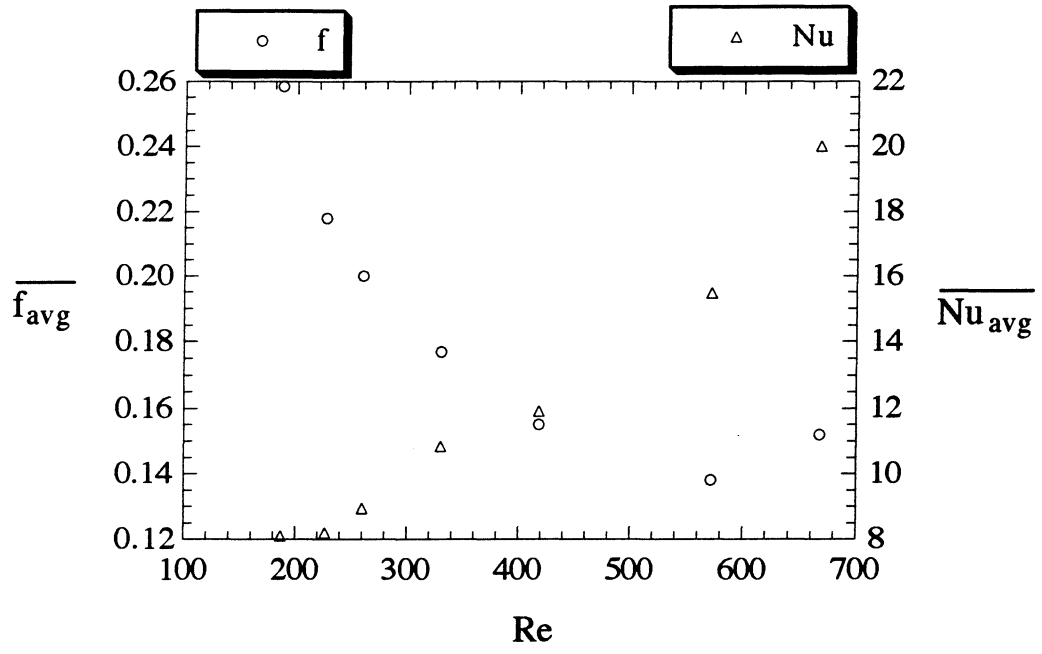

Figure 5.4.8 Time averaged friction factor and Nusselt number averaged across one wavelength as a function of Reynolds number for a = 0.25

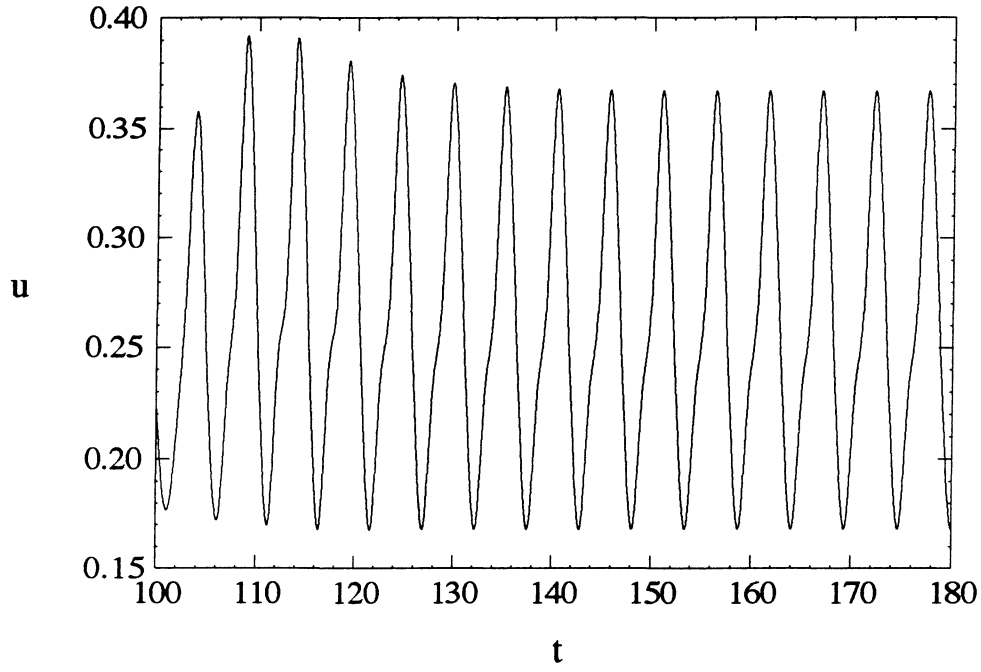

Figure 5.5.1 Time signal for u-velocity in channel with lambda = 2.24 at Re = 189

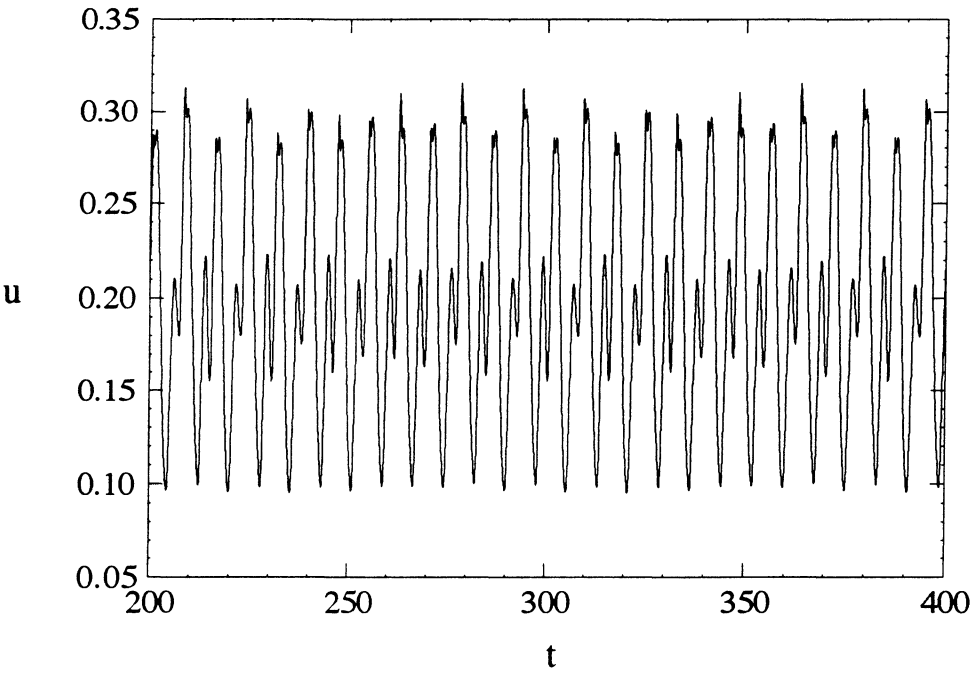

Figure 5.5.2 Time signal for u-velocity in channel with lambda = 2.24 at Re = 492

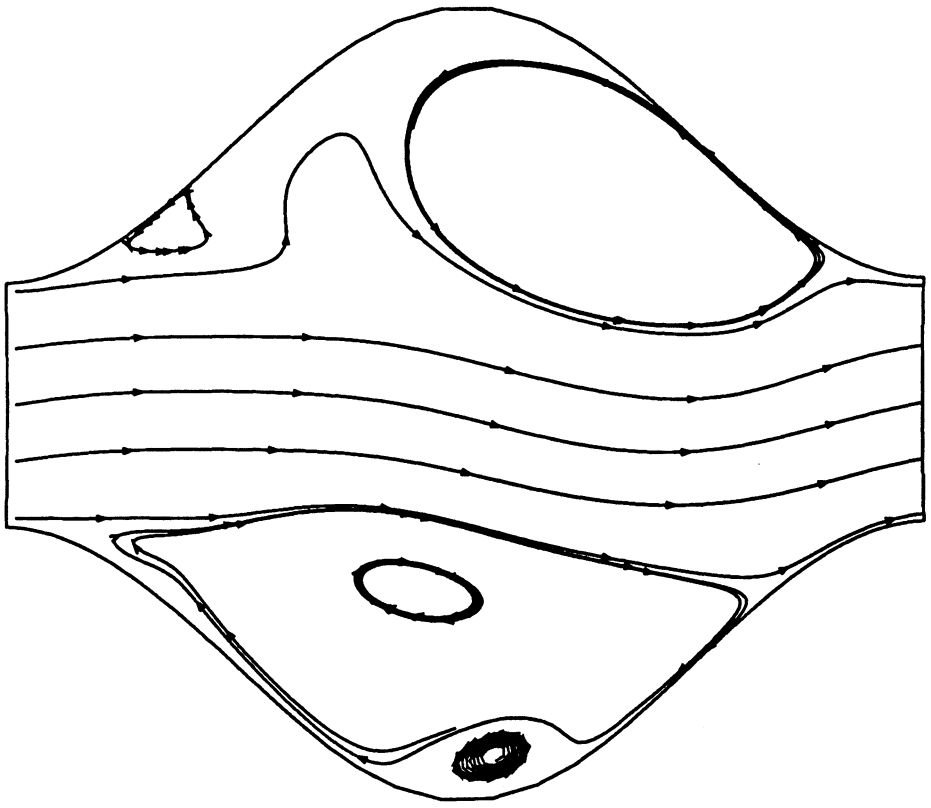

Figure 5.5.3 Instantaneous streamline plot for channel with $\lambda = 2.24$ at Re = 492

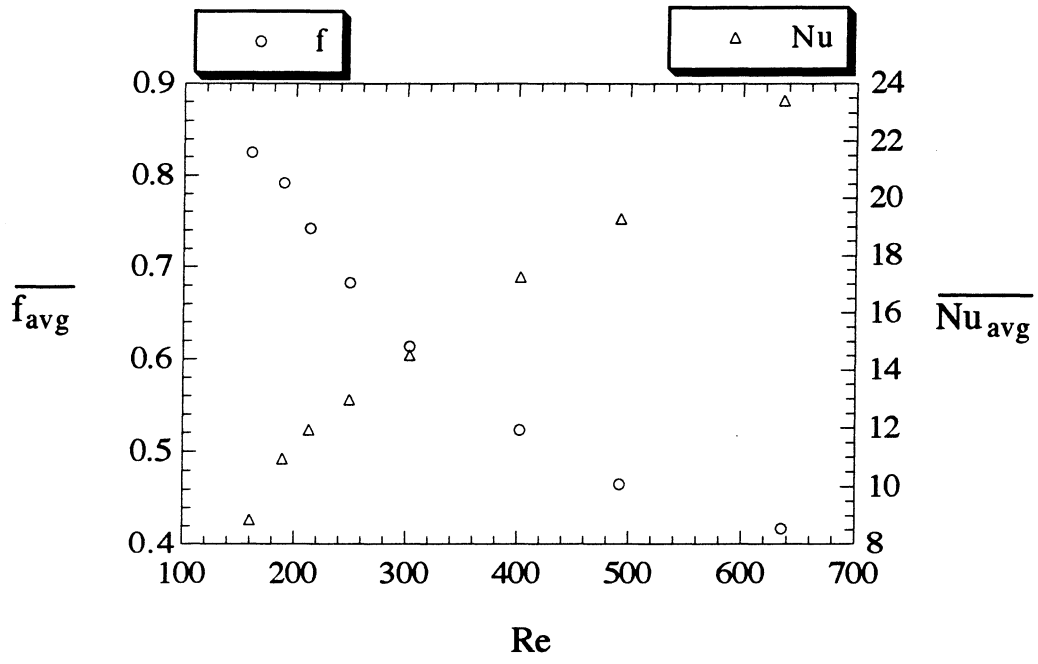

Figure 5.5.4 Time averaged friction factor and Nusselt number averaged across one wavelength as a function of Reynolds number for lambda = 2.24

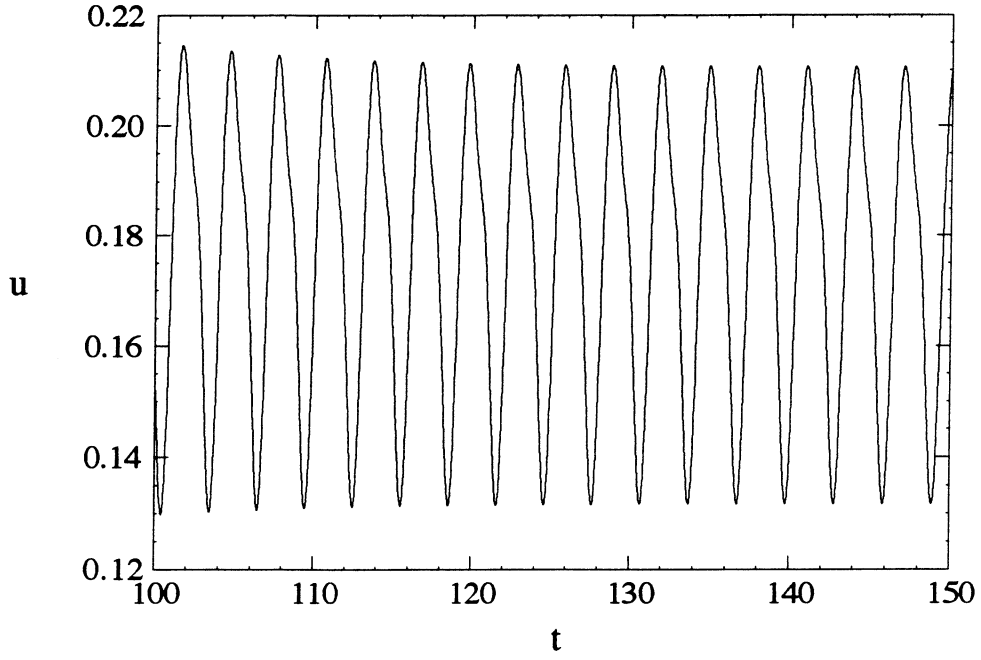

Figure 5.5.5 Time signal for u-velocity in channel with lambda = 3.36 at Re = 213

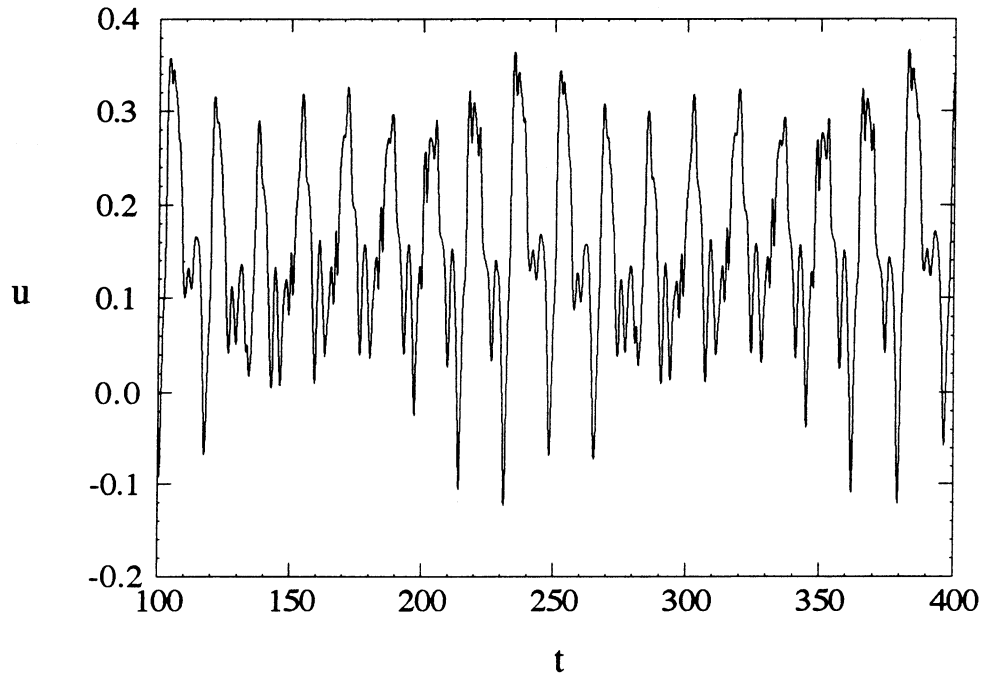

Figure 5.5.6 Time signal for u-velocity in channel with lambda = 3.36 at Re = 443

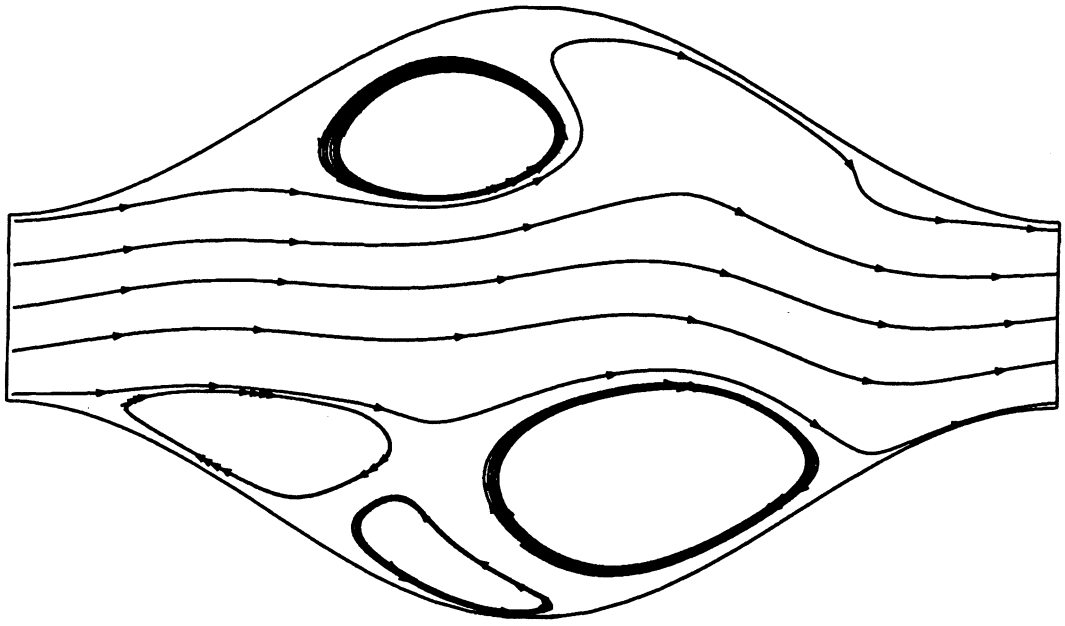

Figure 5.5.7 Instantaneous streamline plot for channel with $\lambda = 3.36$ at Re = 443

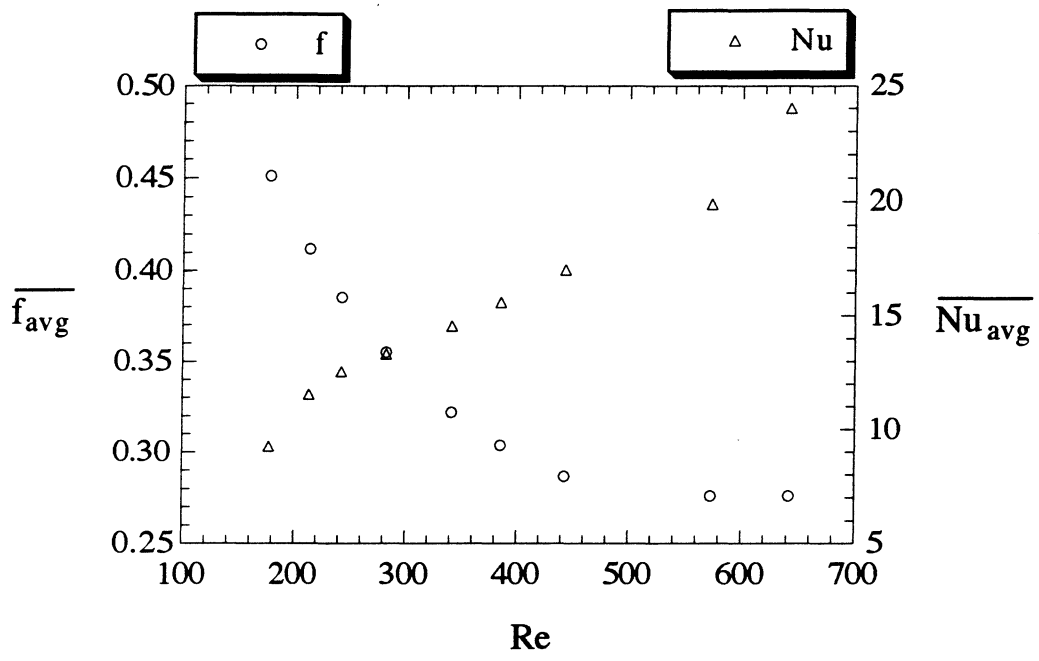

Figure 5.5.8 Time averaged friction factor and Nusselt number averaged across one wavelength as a function of Reynolds number for lambda = 3.36

REFERENCES

Ali, M. M. and Ramadhyani, S. (1992). "Experiments on Convective Heat Transfer in Corrugated Channels," Experimental Heat Transfer, Vol. 5, pp. 175-193.

Amano, R. S., Bagherlee, A., Smith, R. J., and Niess, T. G. (1987). "Turbulent Heat Transfer in Corrugated-Wall Channels With and Without Fins," ASME Journal of Heat Transfer, Vol. 109, pp. 62-67.

Asako, Y. and Faghri, M. (1987). "Finite-Volume Solutions for Laminar Flow and Heat Transfer in a Corrugated Duct," ASME Journal of Heat Transfer, Vol. 109, pp. 627-634.

Asako, Y., Nakamura, H., and Faghri, M. (1988). "Heat Transfer and Pressure Drop Characteristics in a Corrugated Duct with Rounded Corners," International Journal of Heat and Mass Transfer, Vol. 31, No. 6, pp. 1237-1245.

Bergles, A. E., Webb, R. L., and Junkan, G. H. (1979). "Energy Conservation Via Heat Transfer Enhancement," Energy, Vol. 4, pp. 193-200.

Brockmeier, U., Guentermann, T., and Fiebig, M. (1993). "Performance Evaluation of a Vortex Generator Heat Transfer Surface and Comparison with Different High Performance Surfaces," International Journal of Heat and Mass Transfer, Vol. 36, pp. 2575-2587.

Burns, J. C. and Parks, T. (1967). "Peristaltic Motion," Journal of Fluid Mechanics, Vol. 29, pp. 405-416.

Choi, J. M., Anand, N. K., Lau, S. C., and Kukreja, R. T. (1996). "Heat (Mass) Transfer in a Serpentine Channel With Right-Angled Turns," ASME Journal of Heat Transfer, Vol. 118, pp. 211-213.

Garg, V. K. and Maji, P. K. (1988a). "Flow and Heat Transfer in a Sinusoidally Curved Channel," International Journal of Engineering Fluid Mechanics, Vol. 1, No. 3, pp. 293-319.

Garg, V. K. and Maji, P. K. (1988b). "Laminar Flow and Heat Transfer in a Periodically Converging-Diverging Channel," International Journal for Numerical Methods in Fluids, Vol. 8, pp. 579-597.

Goldstein, J. L. and Sparrow, E. M. (1977). "Heat / Mass Transfer Characteristics for Flow in a Corrugated Wall Channel," ASME Journal of Heat Transfer, Vol. 99, pp. 187-195.

Greiner, M., Chen, R.-F., and Wirtz, R. A. (1990). "Heat Transfer Augmentation Through Wall-Shape-Induced Flow Destabilization," ASME Journal of Heat Transfer, Vol. 112, pp. 336-341.

Greiner, M., Chen, R.-F., and Wirtz, R. A. (1991). "Enhanced Heat Transfer / Pressure Drop Measured From a Flat Surface in a Grooved Channel," ASME Journal of Heat Transfer, Vol. 113, pp. 498-501.

Greiner, M., Chen, R.-F., and Wirtz, R. A. (1995). "Augmented Heat Transfer in a Recovery Passage Downstream From a Grooved Section: An Example of Uncoupled Heat / Momentum Transport," ASME Journal of Heat Transfer, Vol. 117, pp. 303-308.

Gschwind, P., Regele, A., and Kottke, V. (1995). "Sinusoidal Wavy Channels with Taylor-Goertler Vortices," Experimental Thermal and Fluid Science, Vol. 11, pp. 270-275.

Guzman, A. M. and Amon, C. H. (1994). "Transition to Chaos in Converging-Diverging Channel Flows: Ruelle-Takens-Newhouse Scenario," Physics of Fluids, Vol. 6, No. 6, pp. 1994-2002.

Guzman, A. M. and Amon, C. H. (1996). "Dynamical Flow Characterization of Transitional and Chaotic Regimes in Converging-Diverging Channels," Journal of Fluid Mechanics, Vol. 321, pp. 25-57.

Kays, W. M. and London, A. L. (1964). Compact Heat Exchangers, The National Press, Palo Alto, CA.

Mendes, P. S. and Sparrow, E. M. (1984). "Periodically Converging-Diverging Tubes and Their Turbulent Heat Transfer, Pressure Drop, Fluid Flow, and Enhancement Characteristics," ASME Journal of Heat Transfer, Vol. 106, pp. 55-63.

Nishimura, T., Ohori, Y., and Kawamura, Y. (1984). "Flow Characteristics in a Channel With Symmetric Wavy Wall for Steady Flow," Journal of Chemical Engineering of Japan, Vol. 17, No. 5, pp. 466-471.

Nishimura, T., Ohori, Y., and Kawamura, Y. (1985). "Mass Transfer Characteristics in a Channel With Symmetric Wavy Wall for Steady Flow," Journal of Chemical Engineering of Japan, Vol. 18, No. 6, pp. 550-555.

Nishimura, T., Kajimoto, Y., and Kawamura, Y. (1986). "Mass Transfer Enhancement in Channels with a Wavy Wall," Journal of Chemical Engineering of Japan, Vol. 19, pp. 142-144.

Nishimura, T., Kajimoto, Y., and Kawamura, Y. (1987). "Flow and Mass Transfer Characteristics in Wavy Channels for Oscillatory Flow," International Journal of Heat and Mass Transfer, Vol. 30, No. 5, pp. 1007-1015.

Nishimura, T., Yano, K., Yoshino, T., and Kawamura, Y. (1990a). "Occurrence and Structure of Taylor-Goertler Vortices Induced in Two-Dimensional Wavy Channels For Steady Flow," Journal of Chemical Engineering of Japan, Vol. 23, No. 6, pp. 697-703.

Nishimura, T., Murakami, S., Arakawa, S., and Kawamura, Y. (1990b). "Flow Observations and Mass Transfer Characteristics in Symmetrical Wavy-Walled Channels at Moderate Reynolds Numbers for Steady Flow," International Journal of Heat and Mass Transfer, Vol. 33, pp. 835-845.

O'Brien, J. E. and Sparrow, E. M. (1982). "Corrugated-Duct Heat Transfer, Pressure Drop, and Flow Visualization," ASME Journal of Heat Transfer, Vol. 104, pp. 410-416.

Oyakawa, K. Shinzato, T., and Mabuchi, I. (1989). "The Effects of the Channel Width on Heat-Transfer Augmentation in a Sinusoidal Wave Channel," JSME International Journal, Series II, Vol. 32, No. 3, pp. 403-410.

Patel, V. C., Chon, J. T., and Yoon, J. Y. (1991a). "Laminar Flow Over Wavy Walls," ASME Journal of Heat Transfer, Vol. 113, pp. 574-578.

Patel, V. C., Chon, J. T., and Yoon, J. Y. (1991b). "Turbulent Flow in a Channel With a Wavy Wall," ASME Journal of Heat Transfer, Vol. 113, pp. 579-586.

Rush, T. (1997). "Investigation of Wavy Fins for Heat Transfer Augmentation in Refrigeration and Air Conditioning Systems" (tentative title), MS Thesis, University of Illinois, Urbana, IL.

Saniei, N. and Dini, S. (1993). "Heat Transfer Characteristics in a Wavy-Walled Channel," ASME Journal of Heat Transfer, Vol. 115, pp. 788-792.

Shah, R. K. and Webb, R. L. (1983)., "Compact and Enhanced Heat Exchangers," Heat Exchangers: Theory and Practice, ed. Taborek, J., Hewitt, G. F., and Afgan, N., Hemisphere Publishing Corporation, Washington, pp. 425-468.

Snyder, B., Li, K. T., and Wirtz, R. A. (1993). "Heat Transfer Enhancement in a Serpentine Channel," International Journal of Heat and Mass Transfer, Vol. 36, No. 12, pp. 2965-2976.

Sobey, I. J. (1980). "On Flow Through Furrowed Channels. Part 1. Calculated Flow Patterns," Journal of Fluid Mechanics, Vol. 96, Part 1, pp. 1-26.

Sobey, I. J. (1982). "Flows at Intermediate Strouhal Number in Asymmetric Channels," Journal of Fluid Mechanics, Vol. 125, pp. 359-373.

Sobey, I. J. (1983). "The Occurrence of Separation in Oscillatory Flow," Journal of Fluid Mechanics, Vol. 134, pp. 247-257.

Sparrow, E. M. and Comb, J. W. (1983). "Effect of Interwall Spacing and Fluid Flow Inlet Conditions on Corrugated-Wall Heat Exchanger," International Journal of Heat and Mass Transfer, Vol. 26, No. 7, pp. 993-1005.

Sparrow, E. M. and Prata, A. T. (1983). "Numerical Solutions for Laminar Flow and Heat Transfer in a Periodically Converging-Diverging Tube, with Experimental Confirmation," Numerical Heat Transfer, Vol. 6, pp. 441-461.

Stephanoff, K. D., Sobey, I. J., and Bellhouse, B. J. (1980). "On Flow Through Furrowed Channels. Part 2. Observed Flow Patterns," Journal of Fluid Mechanics, Vol. 96, part 1, pp. 27-32.

Stephanoff, K. D. (1986). "Self-Excited Shear-Layer Oscillations in a Multi-Cavity Channel with a Steady Mean Velocity," ASME Journal of Fluids Engineering, Vol. 108, pp. 338-342.

Temperton, C. (1979). "Direct Methods for the Solution of the Discrete Poisson Equation: Some Comparisons," Journal of Computational Physics, Vol. 31, pp. 1-20.

Thompson, J. F., Warsi, Z. U. A., and Mastin, C. W. (1985). Numerical Grid Generation: Foundations and Applications, Elsevier Science Publishers B. V.

Vajravelu, K. (1980). "Fluid Flow and Heat Transfer in Horizontal Wavy Channels," Acta Mechanica, Vol. 35, pp. 245-258.

Voelker, S. and Vanka, S. P. (1997). "Fluid Flow and Heat Transfer in Serpentine Channels at Low Reynolds Numbers," University of Illinois at Urbana-Champaign, Air Conditioning and Refrigeration Center, Technical Report ACRC TR-115

Wang, G. and Vanka, S. P. (1995). "Convective Heat Transfer in Periodic Wavy Passages," International Journal of Heat and Mass Transfer, Vol. 38, pp. 3219-3230.

Webb, R. L. (1987). "Enhancement of Single-phase Heat Transfer," Handbook of Single-Phase Convective Heat Transfer, ed. Kakac, S., Shah, R. K., and Bergles, A. E., Wiley, New York, pp. 17-1-62.

Webb, R. L. (1994). Principles of Enhanced Heat Transfer, John Wiley & Sons, Inc., New York.